Numerical study of rapidly rotating turbulent convection

Citation for published version (APA):
Aguirre Guzmán, A. J. (2021). *Numerical study of rapidly rotating turbulent convection*. [Phd Thesis 1 (Research TU/e / Graduation TU/e), Applied Physics and Science Education]. Technische Universiteit Eindhoven.

Document status and date:
Published: 05/03/2021

Document Version:
Publisher’s PDF, also known as Version of Record (includes final page, issue and volume numbers)

Please check the document version of this publication:

• A submitted manuscript is the version of the article upon submission and before peer-review. There can be important differences between the submitted version and the official published version of record. People interested in the research are advised to contact the author for the final version of the publication, or visit the DOI to the publisher's website.
• The final author version and the galley proof are versions of the publication after peer review.
• The final published version features the final layout of the paper including the volume, issue and page numbers.

Link to publication

General rights
Copyright and moral rights for the publications made accessible in the public portal are retained by the authors and/or other copyright owners and it is a condition of accessing publications that users recognise and abide by the legal requirements associated with these rights.

- Users may download and print one copy of any publication from the public portal for the purpose of private study or research.
- You may not further distribute the material or use it for any profit-making activity or commercial gain
- You may freely distribute the URL identifying the publication in the public portal.

If the publication is distributed under the terms of Article 25fa of the Dutch Copyright Act, indicated by the “Taverne” license above, please follow below link for the End User Agreement:

www.tue.nl/taverne

Take down policy
If you believe that this document breaches copyright please contact us at:

openaccess@tue.nl

providing details and we will investigate your claim.

Download date: 04. Oct. 2023

Numerical study of rapidly rotating turbulent convection

Andrés José Aguirre Guzmán

This research was supported by the European Research Council (ERC) under the European Union's Horizon 2020 research and innovation programme, Grant agreement No. 678634. The use of supercomputer facilities (Cartesius) was supported by the Netherlands Organisation for Scientific Research (NWO in Dutch), Grants No. 15462, 16467 and 2019.005.

Copyright © 2021, Andrés José Aguirre Guzmán
All rights reserved.

Cover design by Andrés José Aguirre Guzmán
Printed by Gildeprint - Enschede

A catalogue record is available from the Eindhoven University of Technology Library

ISBN: 978-90-386-5217-7
NUR: 925

Numerical study of rapidly rotating turbulent convection

PROEFSCHRIFT

ter verkrijging van de graad van doctor aan de Technische Universiteit
Eindhoven, op gezag van de rector magnificus prof.dr.ir. F.P.T. Baaijens,
voor een commissie aangewezen door het College voor Promoties, in het
openbaar te verdedigen op vrijdag 5 maart 2021 om 16:00 uur

door

Andrés José Aguirre Guzmán

geboren te Valencia, Venezuela

Dit proefschrift is goedgekeurd door de promotoren en de samenstelling van de promotiecommissie is als volgt:

voorzitter:	prof.dr.ir. G.M.W. Kroesen
1e promotor:	prof.dr. H.J.H. Clercx
co-promotor:	dr.ir. R.P.J. Kunnen
leden:	prof.dr. K. Julien (University of Colorado Boulder)
	prof.dr. J.G.M. Kuerten
	prof.dr.Dipl.-Ing. S. Kenjereš (Technische Universiteit Delft)
	prof.dr. R. Verzicco (Università di Roma “Tor Vergata”)
	prof.dr. F. Toschi

Het onderzoek of ontwerp dat in dit proefschrift wordt beschreven is uitgevoerd in overeenstemming met de TU/e Gedragscode Wetenschapsbeoefening.

Contents

1. Introduction **1**

2. Theoretical Background **7**
2.1. Preliminary remarks 7
2.2. Equations of motion 8
2.3. Dimensionless parameters 10
2.4. Parameter values for onset of convection 11
2.5. Convective heat transfer 12
2.6. Geostrophic flow 13
2.7. Boundary layers 14
2.8. Convective turbulence 18

3. Numerical methods **21**
3.1. Direct numerical simulations 21
3.2. DNS codes 22
3.3. Performance 23
3.4. Numerical setup, transient state and statistical equilibrium . . 24
3.5. Validation 26
3.6. Summary of simulation cases 29

4. Force balances **33**
4.1. Introduction 33
4.2. Magnitudes of the governing forces 37
4.3. Force balance in the bulk 38
4.4. Force balance near no-slip walls 44
4.5. Conclusions 47

5. Flow statistics **49**
5.1. Introduction 49
5.2. Mean temperature and heat transport 53
5.3. Boundary layers 56
5.4. Temperature, velocity and vorticity skewnesses 59
5.5. Temperature, velocity and vorticity kurtoses 64
5.6. Conclusions 68

6. Large-scale vortices **69**
6.1. Introduction 69
6.2. The quasi-dimensional turbulent state 71
6.3. Morphology of the LSVs 73
6.4. Kinetic energy transfer among scales 73
6.5. Near-walls dynamics 75
6.6. Conclusions 77

7. RRBC in a cylinder: the sidewall circulation **81**
7.1. Introduction 81
7.2. Numerical and experimental methods 83
7.3. Instantaneous snapshots 84
7.4. Size of the sidewall circulation 86
7.5. Dynamics of the sidewall circulation 87
7.6. Orientation-compensated mean flow structure of the sidewall circulation 88
7.7. Contributions of bulk and sidewall circulation regions to the heat transfer 90
7.8. Experimental evidence for existence of the sidewall circulation . 92
7.9. Conclusions 93

8. Concluding remarks **97**
8.1. Conclusions 97
8.2. Outlook 99

A. Additional analyses of the sidewall circulation **101**

Bibliography **105**

Summary **125**

Cover Illustration **127**

Curriculum Vitae **129**

List of publications and conferences **131**

Acknowledgements **135**

Chapter 1

Introduction

The exploration of thermally driven turbulent convection dates back to 1900, when Bénard [1–3] experimented with very thin layers of fluid sitting on top of a hot metallic plate. He observed the development of flow motion that organized itself into a regular pattern of convective cells. Some years later, inspired by Bénard's experiment, Rayleigh [4] presented the theoretical analysis of the convective instability of such fluid layers bounded by two infinite horizontal planes. The thermally driven flow confined between a hot bottom plate and a cooler top plate is therefore known as Rayleigh–Bénard convection (RBC). A variant to this classical setup was considered by Chandrasekhar [5], who theoretically investigated, quite thoroughly, the stability of the fluid layer in presence of Coriolis forces [5]. Through linear stability analysis, he provided explicit expressions for the critical Rayleigh numbers (defined below) necessary for the onset of convection. The experimental verification of Chandrasekhar's predictions was given by Nakagawa & Frenzen [6]. Later studies by Rossby [7] showed that sufficiently large Rayleigh numbers lead to transitions from near-onset stable rotating cells to a time-dependent three-dimensional flow and to turbulence. These studies have shown that the stability of the fluid is mainly dependent on three parameters: the Rayleigh number Ra that characterises the strength of the thermal forcing, the Ekman number Ek that measures the strength of rotation (although Rossby used the Taylor number $Ta = Ek^{-2}$; note that small Ek indicates rapid rotation), and the Prandtl number Pr that parametrises the diffusive properties of the fluid.

Rotating Rayleigh–Bénard convection (RRBC) turns out to be incredibly relevant for the fundamental study of numerous geo- and astrophysical flows and for many technological applications. Large-scale motions in Earth's interior, oceans and atmosphere are primarily driven by temperature-induced buoyancy, and develop over length scales that are large enough to make them susceptible to the Earth's rotation. For example, in the liquid-metal outer core, rotating convection is believed to be the energy source of its self-sustained dynamo action [8–11]. Open-ocean deep convection, an integral part of the global thermohaline circulation, is driven by cold sinking fluid from the air-water surface of the seas [12–15]. In the atmosphere, the combined effects of buoyancy and rotation lead to the formation of so-called Hadley cells [16], which are responsible for trade winds near the Earth's surface. Hadley cells at low latitudes, Ferrel cells at mid-latitudes and polar cells at high latitudes are the backbone of the large-scale dynamics of the atmosphere. The effects of rotation and convection can also be evidenced in the interior and atmosphere of the gaseous planets in the solar system: Jupiter, Saturn, Uranus and Neptune exhibit deep convection in their interior [17,18] and zonal flows in their atmosphere [19–22]). In stars, like our Sun, convective currents of plasma in the convection zone are also affected by rotation [23–25]. Finally, rotating convection can also be present in technological applications, such as the convective cooling in rotating turbomachinery blades [26,27], chemical vapour deposition on rotating heated substrates [28], and centrifugal gas separation [29,30].

Hence, rotating Rayleigh–Bénard convection offers a relatively simple, but highly relevant framework to investigate many complex flows in nature and industry. Because of this, RRBC has been extensively studied by means of numerical simulations (e.g. Refs. [31–59]), laboratory experiments (see e.g. Refs. [7,34,35,38,40,43,54,55,60–77]) and theoretical analysis (e.g. Refs. [78–83]). One of the main goals of many RRBC studies is to approximate the typical conditions of thermal forcing, rotation and fluid properties of geophysical and astrophysical settings. These large-scale flows are characterized by extreme values of the governing parameters, combining very large Rayleigh numbers $Ra > 10^{15}$ and very small Ekman numbers $Ek < 10^{-10}$; in Table 1.1 we provide two examples: the Earth's outer core and Jupiter's atmosphere. The Prandtl number can attain quite different values depending on the application: for liquid metals $Pr \sim \mathcal{O}(10^{-2})$, for most gases under normal atmospheric conditions $0.7 \lesssim Pr \lesssim 0.8$, for water at various operating temperatures $3 \lesssim Pr \lesssim 8$, and for highly viscous liquids Pr may take on even larger values. Table 1.1 also provides the range of parameters covered by most direct numerical simulations and by experiments. As we can see, there is a massive separation of several orders of magnitude between simulation/experimental conditions and large-scale natural flows.

While geophysical and astrophysical flow conditions are certainly unfeasible for present-day simulations, in this thesis we investigate RRBC at quite extreme parameter values compared to those explored in previous studies. We perform optimised direct numerical simulations at Rayleigh numbers up to $Ra \sim 10^{12}$ and Ekman numbers $Ek \sim 10^{-7}$. We consider Prandtl number $Pr = 0.1$, relevant to liquid metals as in the Earth's outer core, $Pr \approx 5$, that corresponds

Parameter	Earth's outer core [84–86]	Jupiter's atmosphere [87]	Simulations	Experiments
Thermal forcing Ra	$\sim 10^{20} - 10^{30}$	$\sim 10^{24}$	$\sim 10^{3} - 10^{11}$	$\sim 10^{5} - 10^{15}$
Rotation Ek	$\sim 10^{-15}$	$\sim 10^{-12}$	$\sim 10^{-7} - \infty$	$\sim 10^{-8} - \infty$
Fluid properties Pr	$\sim 10^{-2} - 10^{-1}$	~ 1	$\sim 10^{-2} - 10^{2}$	$\sim 10^{-2} - 10^{2}$

Table 1.1.: *Comparison of estimated parameters for the Earth's outer core and Jupiter's atmosphere with the most extreme parameter values achieved in numerical simulations and laboratory experiments of RRBC.*

to water that is commonly used in experiments and is applicable to oceanic processes, and $Pr = 100$, representative of highly viscous fluids. The parameter space of RRBC is partitioned into several regimes where the flow manifests as: steady cells [81], convective Taylor columns (only at $Pr \gtrsim 2$) [33, 40, 41, 63, 72, 77, 88–91], plumes [33, 41, 72, 88], large-scale vortices [33, 41, 44–46, 50, 58, 92], rotation-affected convection [50, 70] or non-rotating convection [93–96]. We explore a wide range of parameter values that allows the observation of most of these structures. We provide their detailed description in Chapter 4. In this thesis, we characterise the flow regimes according to their specific force balance and flow statistics.

Besides large parameter values, another challenge for RRBC simulations is that under rapid rotation Ekman-type kinetic boundary layers develop at the no-slip top and bottom wall [97]. These Ekman layers are very thin (characteristic thickness $\mathcal{O}(E^{1/2})$), which means that the numerical resolution near the boundaries must be significantly increased in order to resolve these thin layers. This challenge has inhibited direct numerical simulations of the incompressible Navier–Stokes equations from an exhaustive analysis of the flow at large rotation rates. Many studies have then adopted an alternative approach where the flow is simulated in presence of stress-free boundaries, thereby preventing the flow from "sticking" to the walls, and so hindering the development of Ekman layers. Another approach consists of studying the flow in the limit of rapid rotation ($Ek \to \infty$), such that the specific boundary conditions become irrelevant. Under these assumptions a set of asymptotically reduced equations can be derived to describe the rotation-dominated flow. Most of our understanding of RRBC relies on simulations of these asymptotic equations [33, 41, 51, 59]. Laboratory experiments inherently deal with no-slip boundaries, nevertheless, direct flow measurements in the boundary layers remain beyond reach for present-day experiments. This problem is caused by the fact that the Ekman boundary layer is very thin; of the order of one millimetre in typical water-based experiments (at $\nu \sim 10^{-6}$ m^2 s^{-1} and rotation rate $\Omega \sim 1$ rad s^{-1}) regardless of the container's height. Therefore, research on the dynamics of the flow close to no-slip boundaries has been limited to direct numerical simulations. From these, we know that kinetic boundary layers in rapidly rotating Rayleigh–Bénard convection are indeed of Ekman-type, and that they can markedly influence the bulk dynamics and heat transfer across the fluid layer, unlike those formed in the non-rotating case [45, 52, 63, 64, 88, 97, 98]. However, some questions remain: how does their specific dynamics connect to the above-mentioned bulk regimes? And, does this dynamics change from one regime to another? In the interest of shedding light on these matters, most of the numerical simulations presented in this thesis do employ no-slip walls.

An interesting regime of RRBC manifests when the flow is rotationally constrained and yet it remains turbulent due to strong thermal forcing. The resulting dynamics may lead to the development of long-lived, large-scale vortices (LSVs) in the flow [41, 44, 46, 51, 92]. A customary decomposition of this flow consists of a so-called barotropic component that represents the dominant 2D (depth-averaged) dynamics of the flow, and a baroclinic component to denote the 3D (depth-dependent) convective motion. These coherent structures are most clearly observed in the stress-free case, whereas their formation is inhibited in simulations with no-slip boundaries [45, 50, 51]. In the latter case, the premise is that vertical disturbances due to Ekman pumping from the boundary layers disrupt the development of large scales in the flow. It is believed that this adverse role of the Ekman layers weakens at very large rotation rates [41, 99, 100]. The question is whether the increased rotation can suppress vertical disturbances to a degree where the condition for LSV formation are effectively met. Addressing this issue is challenging, because the thermal forcing must then be increased too in order to ensure turbulence. In this thesis we evaluate the formation of large-scale vortices for our rather extreme suite of explored parameter values.

Up until now, the effect of lateral boundaries has been mostly ignored. This configuration is of course appropriate for certain natural phenomena where, for example, the lateral dimensions of the system are much larger than the vertical, as in oceans, planetary atmospheres and the solar convection zone. Because this thesis is inspired by these large-scale geophysical and astrophysical flows, most of our simulations consider a Cartesian domain with periodic lateral boundaries. However, this setup is impossible to achieve experimentally. Most experiments are carried out in cylindrical vessels sitting on a rotating table. It is therefore paramount to establish connections between experiments on a confined cylindrical domain and simulations on a laterally unconfined periodic domain [53, 55, 56, 101]. To bridge this gap, we also perform direct numerical simulations on a cylindrical domain.

Thesis outline

This work is structured as follows. Chapter 2 introduces the theoretical foundations of rotating Rayleigh–Bénard convection needed for the present investigation. Chapter 3 presents a brief review of the methodology of the direct numerical simulations, as well as details on the validation of the numerical results. A list of the simulation cases explored is included. In Chapter 4 we analyse the interplay between the forces acting on the fluid in RRBC. We do so for the various observed flow states, and compare the force balance in the bulk with that near the no-slip plates. We also present a discussion on the nature of the transitions among flow regimes. In Chapter 5 we examine the statistical properties of the bulk and near-wall flow and their transitional behaviours between flow regimes in laterally unconfined RRBC. In Chapter 6 we focus on the regime of large-scale vortices, as their formation in presence of no-slip boundaries is a novel result. We investigate their structure, conditions for development, energy transfer properties and near-wall dynamics. In Chapter 7 we study turbulent convection in a confined domain, i.e. in a cylindrical vessel as in laboratory experiments, where the development of a so-called sidewall circulation is observed. We characterise its size, dynamics and, especially, its contribution to the convective heat transfer. We also discuss how this sidewall circulation interacts with the bulk, and its implications on the development of bulk structures such as those found in laterally unconfined domains, discussed in the previous chapters. Finally, in Chapter 8 we provide an overall conclusion to the thesis and an outlook to further research on turbulent rotating convection.

Chapter 2

Theoretical Background

This chapter provides a brief summary of the theoretical background necessary for the following chapters. We present the equations of motion of rotating Rayleigh–Bénard convection, the related dimensionless parameters, and discuss the effects of rotation on the flow in the fluid bulk and near solid boundaries.

2.1. Preliminary remarks

In this section we set the stage for this chapter, where we motivate the concepts to be discussed. We start off by deriving the governing equations of RRBC in Section 2.2. For the task, we first introduce the equations of motion of thermal convection, then we employ the Oberbeck–Boussinesq approximation, and finally we derive these equations in a rotating frame of reference. In Section 2.3, we nondimensionalise the governing equations and present the relevant dimensionless parameters. These parameters dictate the convective state of the flow. In Section 2.4, we present the critical values of these parameters that lead to the onset of convection. The response of the system to these convective motions is measured by the Nusselt number Nu. We introduce this output parameter in Section 2.5. As mentioned in Chapter 1, planetary-scale flows are greatly influence by the rotation of the celestial body. As a result, their dynamics is directed by the so-called geostrophic balance. In Section 2.6, we derive and discuss this balance as well as the Taylor–Proudman theorem. These concepts are needed later on in Chapters 4 and 5, where we discuss the rotation-dominated regimes of RRBC. In these two chapters we also investigate the flow dynamics close to no-slip top and bottom boundaries, where Ekman-type viscous boundary layers develop. We thus dedicate Section 2.7 to introduce the fundamental properties of these layers. In this section we also discuss the boundary layers that develop along the sidewalls in confined domains: the Stewartson boundary layers. The role of lateral confinement is investigated in Chapter 7. Finally, in Section 2.8, we address the presence of turbulence in RRBC by introducing useful definitions of convective turbulence.

2.2. Equations of motion

In the Rayleigh–Bénard convection setup, a fluid layer between two parallel horizontal plates is heated from below and cooled from above in order to induce a buoyancy-driven flow. The incompressible flow of a Newtonian fluid is described by the Navier–Stokes equations

$$\rho \left(\frac{\partial \boldsymbol{u}}{\partial t} + (\boldsymbol{u} \cdot \boldsymbol{\nabla}) \, \boldsymbol{u} \right) = -\boldsymbol{\nabla} p + \boldsymbol{\nabla} \cdot \boldsymbol{\tau} - \rho g \hat{\boldsymbol{z}} \tag{2.1}$$

and temperature by the advection-diffusion equation

$$\rho c_p \left(\frac{\partial T}{\partial t} + \boldsymbol{u} \cdot \boldsymbol{\nabla} T \right) = k \nabla^2 T, \tag{2.2}$$

subject to the incompressibility constraint

$$\boldsymbol{\nabla} \cdot \boldsymbol{u} = 0. \tag{2.3}$$

In these equations, ρ is the density of the fluid, $\boldsymbol{u} = (u, v, w)$ is the fluid velocity, t is time, p is pressure, $\boldsymbol{\tau}$ is the viscous stress tensor, g is gravitational acceleration, $\hat{\boldsymbol{z}}$ is the unit vector in the vertical direction, T is temperature, c_p is the specific heat at constant pressure, and k is the thermal conductivity of the fluid. Moreover, the viscous stress tensor for a Newtonian fluid is given by

$$\boldsymbol{\tau} = 2\mu \boldsymbol{\varepsilon} \tag{2.4}$$

where

$$\boldsymbol{\varepsilon} = \frac{1}{2} \left(\boldsymbol{\nabla} \boldsymbol{u} + \boldsymbol{\nabla} \boldsymbol{u}^T \right) \tag{2.5}$$

is the rate-of-strain tensor and μ is the dynamic viscosity of the fluid. Equations (2.1) to (2.3) express respectively the conservation of momentum, energy and mass [102].

Oberbeck–Boussinesq approximation

Rayleigh–Bénard convection is often studied in the Oberbeck–Boussinesq (OB) approximation [103, 104], where fluid properties are assumed constant (i.e. independent of temperature) and density variations are only important in the buoyancy term. The assumption is that density differences do not lead to significant changes in inertia, yet the gravitational acceleration g is sufficiently strong to drive the convective flow. Furthermore, density variations ρ' are assumed to be linearly dependent on the temperature variations T' as

$$\frac{\rho'}{\rho_0} = -\alpha T' \tag{2.6}$$

where α is the thermal expansion coefficient of the fluid. Here, density and temperature fluctuations are relative to, and much smaller, than their corresponding static constant equilibrium values ρ_0 and T_0. That is, the total density is $\rho = \rho_0 + \rho'$ with $\rho' \ll \rho_0$, and the total temperature is $T = T_0 + T'$ with $T' \ll T_0$. Similarly, the total pressure can be written as $p = p_0 + p'$ with $p' \ll p_0$.

Based on these approximations, the term $-\boldsymbol{\nabla} p - \rho g \hat{\boldsymbol{z}}$ in Eq. (2.1) can be simply written as $-\boldsymbol{\nabla} p' - \rho' g \hat{\boldsymbol{z}}$ (because $\boldsymbol{\nabla} p_0 = -\rho_0 g \hat{\boldsymbol{z}}$ is the hydrostatic balance) and the divergence of the viscous stress tensor in Eq. (2.4) is $\boldsymbol{\nabla} \cdot \boldsymbol{\tau} = \mu \nabla^2 \boldsymbol{u}$ (because μ is constant due to the OB approximation). Therefore, dropping the primes, the set of governing equations are [81]

$$\frac{\partial \boldsymbol{u}}{\partial t} + (\boldsymbol{u} \cdot \boldsymbol{\nabla})\, \boldsymbol{u} = -\frac{1}{\rho_0} \boldsymbol{\nabla} p + \nu \nabla^2 \boldsymbol{u} + g \alpha T \hat{\boldsymbol{z}} \tag{2.7}$$

$$\frac{\partial T}{\partial t} + \boldsymbol{u} \cdot \boldsymbol{\nabla} T = \kappa \nabla^2 T \tag{2.8}$$

$$\boldsymbol{\nabla} \cdot \boldsymbol{u} = 0 \tag{2.9}$$

where $\nu = \mu/\rho_0$ and $\kappa = k/(c_p \rho_0)$ are the kinematic viscosity and thermal diffusivity of the fluid, respectively.

The OB approximation is reasonably valid for small temperature differences, such that $\alpha T' \ll 1$. In practice, a rule of thumb for their validity, often applied in convection, is that $\alpha \Delta T \lesssim 0.2$ [105, 106], where $\Delta T = T_{\text{bottom}} - T_{\text{top}} > 0$ is the temperature difference between bottom and top plates.

Background rotation

Equations (2.7) to (2.9) describe Rayleigh–Bénard convection in an inertial frame of reference. In a rotating reference frame, like on our Earth, for example, the equations need to be adjusted. For details of this derivation we refer the reader to references [107] and [108]. Concretely, the acceleration $\boldsymbol{a} = d\boldsymbol{u}/dt$ in the inertial frame is related to the acceleration in the rotating frame $\boldsymbol{a}_{\text{R}}$ by the expression

$$\boldsymbol{a} = \boldsymbol{a}_{\text{R}} + 2\boldsymbol{\Omega} \times \boldsymbol{u}_{\text{R}} - \Omega^2 \boldsymbol{r}_{\perp} \tag{2.10}$$

where $\boldsymbol{\Omega}$ is the constant angular velocity of the rotating coordinate system and $\boldsymbol{u}_{\text{R}}$ the velocity vector in this frame. The position in the rotating frame is given by $\boldsymbol{r}$, and $\boldsymbol{r}_\perp$ denotes its projection on the plane perpendicular to $\boldsymbol{\Omega} = \Omega\hat{\boldsymbol{z}}$. The last term, $\Omega^2\boldsymbol{r}_\perp$, can also be written in the form of a gradient as $\boldsymbol{\nabla}\left(\frac{1}{2}\Omega^2 r_\perp^2\right)$. This allows, without loss of generality, to incorporate this term in the pressure gradient, such that $\boldsymbol{\nabla} p$ becomes $\boldsymbol{\nabla}\left(p - \frac{1}{2}\Omega^2 r_\perp^2\right)$, where the latter term is commonly referred to as the reduced pressure. Therefore, dropping the subscripts, the momentum equation that describes rotating Rayleigh–Bénard convection is

$$\frac{\partial \boldsymbol{u}}{\partial t} + (\boldsymbol{u}\cdot\boldsymbol{\nabla})\,\boldsymbol{u} + 2\boldsymbol{\Omega}\times\boldsymbol{u} = -\frac{1}{\rho_0}\boldsymbol{\nabla} p + \nu\nabla^2\boldsymbol{u} + g\alpha T\hat{\boldsymbol{z}} \tag{2.11}$$

where the Coriolis acceleration is represented by the third term on the left-hand side.

2.3. Dimensionless parameters

Equations (2.8), (2.9) and (2.11) involve a large number of dimensional quantities: parameters $(\Omega, \rho_0, \nu,\ \kappa,\ \alpha,\ g)$, dependent variables $(\boldsymbol{u},\ p,\ T)$ and independent variables $(\boldsymbol{x},\ t)$. A reduction of the parameter space can be attained through nondimensionalisation. For the task, we normalise length by the domain height H (distance between bottom and top walls), velocity by the characteristic velocity scale U, time by H/U, temperature fluctuations by ΔT and pressure by $\rho_0 U^2$ (typical for inertia-dominated flows). The result is

$$\frac{\partial \boldsymbol{u}}{\partial t} + (\boldsymbol{u}\cdot\boldsymbol{\nabla})\,\boldsymbol{u} + \frac{2\Omega H}{U}\hat{\boldsymbol{z}}\times\boldsymbol{u} = -\boldsymbol{\nabla} p + \frac{\nu}{UH}\nabla^2\boldsymbol{u} + \frac{g\alpha\Delta T H}{U^2}T\hat{\boldsymbol{z}}, \tag{2.12}$$

$$\frac{\partial T}{\partial t} + (\boldsymbol{u}\cdot\boldsymbol{\nabla})\,T = \frac{\kappa}{UH}\nabla^2 T, \tag{2.13}$$

$$\boldsymbol{\nabla}\cdot\boldsymbol{u} = 0. \tag{2.14}$$

In RRBC, it is reasonable to assume the leading role of the buoyancy force by setting $g\alpha\Delta T H/U^2 \sim \mathcal{O}(1)$, which leads to a relevant and convenient velocity scale: the so-called "free-fall" convective velocity $U_{\mathrm{ff}} = \sqrt{g\alpha\Delta T H}$ [109]. This velocity scale serves as an upper bound for buoyancy-generated velocity, as it evaluates the limit case where all the heating power goes towards fluid motions [31, 110, 111]. We now introduce the "traditional" dimensionless parameters in rotating Rayleigh–Bénard convection: the Rayleigh number, the Prandtl number and the Rossby number [81]

$$Ra = \frac{g\alpha\Delta T H^3}{\nu\kappa}, \tag{2.15}$$

$$Pr = \frac{\nu}{\kappa}, \tag{2.16}$$

$$Ro = \frac{U}{2\Omega H}, \tag{2.17}$$

respectively. The Rayleigh number measures the strength of the thermal forcing as the ratio between buoyancy and dissipation, the Prandtl number involves the diffusive properties of the fluid, and the Rossby number parametrises the strength of rotation as the ratio between inertial force and Coriolis force. We immediately see that, in Eq. (2.12),

$$\frac{2\Omega H}{U} = \frac{1}{Ro}, \quad \frac{\nu}{UH} = \sqrt{\frac{Pr}{Ra}} \text{ and } \frac{\kappa}{UH} = \frac{1}{\sqrt{RaPr}}.$$

which yields the desired reduction of the parameter space. That is, the original number of parameters is reduced to three dimensionless parameters: Ra, Pr and Ro.

Note that we assumed that the characteristic velocity scale U is equal to the free-fall convective velocity U_{ff}. Under this assumption, a *convective* Rossby number can be defined as

$$Ro_{\mathrm{C}} = \frac{\sqrt{g\alpha\Delta T/H}}{2\Omega}. \tag{2.18}$$

Such that buoyancy is dominant for $Ro_{\mathrm{C}} \gg 1$, whereas Coriolis forces are stronger for $Ro_{\mathrm{C}} \ll 1$.

Alternatively, the strength of rotation can be parametrised by means of the Ekman number

$$Ek = \frac{\nu}{2\Omega H^2}, \tag{2.19}$$

which provides the ratio of viscous to Coriolis force. A convenient relation between the various dimensionless parameters is $Ro_{\mathrm{C}} = Ek\sqrt{Ra/Pr}$.

2.4. Parameter values for onset of convection

Rotation, contrary to convection, has a stabilizing effect on the flow. Therefore, at low values of the Rayleigh number and sufficiently strong rotation (low Ek and Ro_{C}), no convective motions take place, and the heat transfer from bottom to top boundary is exclusively due to conduction. In an infinite fluid layer subject to rapid rotation ($Ek \lesssim 10^{-3}$), the critical Rayleigh number Ra_c for the onset of convection is given by [74,81]

$$Ra_c = \begin{cases} 17.4\,(Ek/Pr)^{-4/3} & \text{for } Pr < 0.68 \\ 8.7Ek^{-4/3} & \text{for } Pr \gtrsim 0.68 \end{cases}. \tag{2.20}$$

Passed this threshold, bulk convection starts in the form of oscillatory structures for $Pr < 0.68$ and steady cells for $Pr \gtrsim 0.68$. Based on this critical value we define supercriticality as Ra/Ra_c, where Ra_c takes either definition in Eq. (2.20) depending on the Prandtl number of a given study case. Our results are presented as a function of Ra/Ra_c throughout this work.

The characteristic horizontal length scale ℓ_c of the onset structures is given by [81,112,113]

$$\ell_c = \begin{cases} 2.4\,(Ek/Pr)^{1/3} & \text{for } Pr < 0.68 \\ 2.4Ek^{1/3} & \text{for } Pr \gtrsim 0.68 \end{cases}, \tag{2.21}$$

again, valid for an infinite layer of fluid and rapid rotation ($Ek \lesssim 10^{-3}$).

2.5. Convective heat transfer

Upon the onset of convection, one of the primary results of many investigations of Rayleigh–Bénard convection is the convective heat transport from the bottom to the top wall. A convenient way to express this convective heat transport in dimensionless form consists of scaling the total heat transfer (convection and conduction) with the heat transfer by conduction alone. This ratio is known as the Nusselt number

$$Nu \equiv \frac{\langle q\rangle H}{k\Delta T}, \tag{2.22}$$

where $\langle q\rangle$ is the mean total heat-current density, which is equal to the sum of the vertical contributions of the mean local convective flux $\langle q_{\text{conv}}\rangle = \rho c_p \langle wT\rangle = (k/\kappa)\,\langle wT\rangle$ and its conductive counterpart $\langle q_{\text{cond}}\rangle = -k\langle \partial T/\partial z\rangle$. Therefore, making velocity, temperature and length dimensionless as above, we arrive at the fully dimensionless formulation

$$Nu = \sqrt{RaPr}\,\langle wT\rangle - \left\langle \frac{\partial T}{\partial z} \right\rangle. \tag{2.23}$$

In practice, two forms of this equation are very useful for the calculation of Nu in numerical simulations. The first one considers the estimation of Nu at the horizontal plates, where convection is zero (because $w = 0$) and the entire heat flux is solely provided by conduction:

$$Nu = -\left\langle \frac{\partial T}{\partial z} \right\rangle_{A,t} \quad \text{at } z = 0, 1, \tag{2.24}$$

with $\langle \cdot \rangle_{A,t}$ indicating averaging over the area of the (bottom or top) plate and in time. The second form involves the averaging of Eq. (2.23) over the entire volume, such that the conductive part is $-\langle \partial T / \partial z \rangle_{V,t} = 1$, and thus

$$Nu = 1 + \sqrt{RaPr}\, \langle wT \rangle_{V,t} \,. \tag{2.25}$$

where $\langle \cdot \rangle_{V,t}$ denotes averaging over the entire fluid volume and in time.

In the absence of rotation, the Nusselt number can be related to the thickness of the thermal boundary layer, δ_θ, which develops near the top/bottom wall. That is, without rotation, turbulent convection tends to mix the fluid in the bulk very well. As a consequence, the temperature in this region is constant. In turn, the temperature drop across the fluid layer, ΔT, is accomplished almost entirely within the thermal boundary layers [114,115]. Within these layers, each one of thickness δ_θ, the transfer of heat is nearly entirely conductive. Therefore, $\langle q \rangle \approx \langle q_{\text{cond}} \rangle \approx k|\Delta T|/(2\delta_\theta)$, where the total heat flux $\langle q \rangle$ relates to the Nusselt number Nu through Eq. (2.22). Hence, a very appropriate approximation for the thermal boundary layer thickness δ_θ is found:

$$\frac{\delta_\theta}{H} = \frac{1}{2Nu}. \tag{2.26}$$

2.6. Geostrophic flow

The dynamics of large-scale flows in geophysics and astrophysics is predominantly controlled by the Coriolis force and the pressure-gradient force. The equilibrium between these two forces is known as the *geostrophic* balance [116]. Thus, regimes of RRBC that exhibit such leading contribution of Coriolis force and the pressure-gradient force are of particular importance to these natural flows. In Chapter 4 we investigate, thoroughly, the force balance of the distinct flow regimes observed in our explored parameter space. In this section, we discuss the fundamental aspects of geostrophic flows.

We start off by considering the quasi-steady flow of a homogeneous fluid (i.e. density variation $\rho' = 0$) subject to rapid rotation (i.e. $Ro \ll 1$ and $Ek \ll 1$). In such a case, inertial and viscous forces are negligible compared to the Coriolis force. Several terms in Eq. (2.11) can then be discarded, leading to the following force balance per component

$$-2\Omega v = -\frac{1}{\rho_0}\frac{\partial p}{\partial x}, \tag{2.27}$$

$$2\Omega u = -\frac{1}{\rho_0}\frac{\partial p}{\partial y}, \tag{2.28}$$

$$0 = -\frac{1}{\rho_0}\frac{\partial p}{\partial z}. \tag{2.29}$$

The horizontal balance between the Coriolis and pressure-gradient forces establishes the geostrophic balance [116]. This states that fluid particles move along isobars, and thus that isobars are streamlines.

Using Eqs. (2.27) to (2.29), it can be shown that $\partial u/\partial z = \partial v/\partial z = 0$. Furthermore, from Eqs. (2.27) and (2.28), and the incompressibility condition $\boldsymbol{\nabla} \cdot \boldsymbol{u} = 0$, it can be shown that $\partial w/\partial z = 0$. Therefore,

$$\frac{\partial \boldsymbol{u}}{\partial z} = \boldsymbol{0}. \tag{2.30}$$

This result is known as the Taylor–Proudman theorem [117, 118], and states that the horizontal velocity field has no vertical shear and that all particles on the same vertical move in concert. It also establishes that the vertical velocity, too, is independent of height. Thus, if the fluid is limited in the vertical by an impenetrable boundary, such that the vertical velocity w is zero there, then w is zero everywhere. As a consequence, the flow is strictly two-dimensional. In reality, geostrophic flows in nature do exhibit non-zero vertical velocities as well. The existence of these flows, so called *ageostrophic*, entails a relaxation of the idealised Taylor–Proudman constraint.

2.7. Boundary layers

Until now, we have introduced theoretical concepts that pertain solely to the flow far from any boundaries. Yet, in realistic settings, flows are heavily affected by the bounding surfaces. In Chapters 4 to 6 we investigate the flow dynamics near the vertical boundaries, where Ekman layers develop. In Chapter 7 we study RRBC in a domain with lateral boundaries, where a recently observed sidewall circulation is established, along with the Stewartson boundary layers. In this section, we present the fundamental aspects of Ekman and Stewartson boundary layers.

Ekman boundary layer

We begin by considering the quasi-steady, rapidly rotating flow ($Ro \ll 1$) of a homogeneous fluid ($\rho' = 0$) near a solid wall at $z = 0$. Here, the angular velocity vector $\boldsymbol{\Omega}$ is perpendicular to the wall. In this scenario the velocity is geostrophic in the bulk, i.e. $\boldsymbol{u} = \boldsymbol{u}_b$ at $z \to \infty$, but it rapidly reduces to $\boldsymbol{u} = \mathbf{0}$ at $z = 0$ as the no-slip condition must be met at the wall. This reduction is carried out by viscous forces within a thin region adjacent to the wall, the so-called Ekman boundary layer [97]. It is then assumed that wall-normal derivatives are much larger than derivatives along the wall [116]. Thus, for example, $\partial u/\partial x \ll \partial u/\partial z$ and $\partial v/\partial y \ll \partial v/\partial z$. Applying these approximations on Eq. (2.11), the near-wall flow is described by [116]

$$-2\Omega v = -\frac{1}{\rho_0}\frac{\partial p}{\partial x} + \nu\frac{\partial^2 u}{\partial z^2}, \tag{2.31}$$

$$2\Omega u = -\frac{1}{\rho_0}\frac{\partial p}{\partial y} + \nu\frac{\partial^2 v}{\partial z^2}, \tag{2.32}$$

$$0 = -\frac{1}{\rho_0}\frac{\partial p}{\partial z}, \tag{2.33}$$

whereas in the bulk

$$-2\Omega v_b = -\frac{1}{\rho_0}\frac{\partial p_b}{\partial x}, \tag{2.34}$$

$$2\Omega u_b = -\frac{1}{\rho_0}\frac{\partial p_b}{\partial y}, \tag{2.35}$$

$$0 = -\frac{1}{\rho_0}\frac{\partial p_b}{\partial z}. \tag{2.36}$$

From Eq. (2.33) we notice that $\partial(\partial p/\partial x)/\partial z = \partial(\partial p/\partial z)/\partial x = 0$ (likewise in the y-direction). This indicates that the horizontal pressure gradient is independent of z near the wall. The same conclusion can be drawn in the bulk by means of Eq. (2.36). Therefore, the horizontal pressure gradient near the wall is actually equal to that in the bulk. The horizontal pressure gradient is therefore determined entirely by the geostrophic velocity $\boldsymbol{u}_b$ far from the boundary:

$$\frac{1}{\rho_0}\frac{\partial p}{\partial x} = \frac{1}{\rho_0}\frac{\partial p_b}{\partial x} = 2\Omega v_b \quad \text{and} \quad \frac{1}{\rho_0}\frac{\partial p}{\partial y} = \frac{1}{\rho_0}\frac{\partial p_b}{\partial y} = -2\Omega u_b,$$

and Eqs. (2.31) and (2.32) can now be written as

$$-2\Omega v = -2\Omega v_b + \nu \frac{\partial^2 u}{\partial z^2}, \tag{2.37}$$

$$2\Omega u = 2\Omega u_b + \nu \frac{\partial^2 v}{\partial z^2}. \tag{2.38}$$

The exact solutions to Eqs. (2.37) and (2.38), that satisfy the boundary conditions: $\boldsymbol{u} = \boldsymbol{u}_b$ at $z \to \infty$ and $\boldsymbol{u} = \mathbf{0}$ at $z = 0$, are

$$u = u_b - \left[u_b \cos\left(z/\delta_u\right) + v_b \sin\left(z/\delta_u\right)\right] \exp\left(-z/\delta_u\right), \tag{2.39}$$

$$v = v_b + \left[u_b \sin\left(z/\delta_u\right) - v_b \cos\left(z/\delta_u\right)\right] \exp\left(-z/\delta_u\right), \tag{2.40}$$

where $\delta_u = \sqrt{\nu/\Omega}$ is a length scale that characterizes the thickness of the Ekman boundary layer. Note that

$$\frac{\delta_u}{H} \sim Ek^{1/2} \tag{2.41}$$

according to Eq. (2.19).

The vertical velocity w can be determined by using Eqs. (2.39) and (2.40) in the incompressibility condition $\partial w/\partial z = -(\partial u/\partial x + \partial v/\partial y)$. After integration (and noting that $\boldsymbol{u} = \mathbf{0}$ at $z = 0$), we obtain:

$$w = \frac{\omega_b \delta_u}{2} \left\{1 - \exp\left(-z/\delta_u\right)\left[\sin\left(z/\delta_u\right) + \cos\left(z/\delta_u\right)\right]\right\}, \tag{2.42}$$

where $\omega_b = \partial v_b/\partial x - \partial u_b/\partial y$ is the vertical vorticity in the bulk. At $z \to \infty$, where $\boldsymbol{u} = \boldsymbol{u}_b$:

$$w_b = \frac{\omega_b \delta_u}{2}. \tag{2.43}$$

That is, the Ekman boundary layer is able to actively influence the bulk flow through vertical motion, which is known as *Ekman pumping*. For $\omega_b < 0$, the flux is from the bulk into the boundary layer; this is referred to as *Ekman suction*. Eq. (2.43) is valid near the bottom wall. Near the top wall, a minus sign needs to be added in Eq. (2.43).

To illustrate the dynamics of the Ekman boundary layer, let us assume $v_b = 0$ for simplicity, so that Eqs. (2.39) and (2.40) become

$$u = u_b\left[1 - \cos\left(z/\delta_u\right)\exp\left(-z/\delta_u\right)\right], \tag{2.44}$$

$$v = u_b \sin\left(z/\delta_u\right)\exp\left(-z/\delta_u\right). \tag{2.45}$$

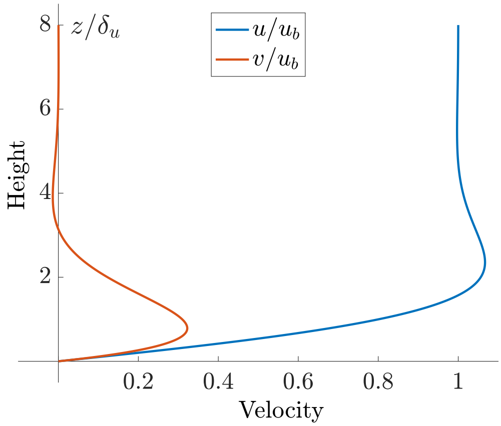

Figure 2.1.: *Vertical profile of the x- and y-component of the flow velocity scaled by the geostrophic velocity u_b, i.e. u/u_b and v/u_b, respectively. The vertical coordinate z is scaled by the Ekman-layer thickness δ_u.*

Figure 2.1 shows the profiles of the velocity components u and v. Far from the wall the velocity is equal to the geostrophic velocity, i.e. $(u, v) = (u_b, 0)$, and so it is entirely in the x-direction. The pressure gradient in the y-direction, independent of z, is balanced at infinity by the y-component of the Coriolis force (see Eq. (2.35)). As the wall is approached, friction decreases u, weakening the Coriolis force. As a consequence, the now unbalanced pressure force in the y-direction produces a velocity v in that direction, which is reduced by friction alone. Therefore, in the presence of the wall, the effect of friction is to break the constraint of exact geostrophic balance (as represented by Eqs. (2.31) and (2.32)) and produce a flow across the isobars from high to low pressure. This implies that work is being done on the fluid in the Ekman layer by the pressure force of the geostrophic flow. This work supplies the necessary energy to maintain the Ekman layer in the presence of frictional dissipation.

Stewartson boundary layer

In confined domains, the bottom/top Ekman layers can drive a secondary circulation, of magnitude $\mathcal{O}(Ek^{1/2})$ (see Eq. (2.41)), which must be somehow compensated. It turns out that this *inward* or *outward* flux is typically balanced by the boundary layer on the sidewall. Such boundary layers are known as *Stewartson layers* [107, 119, 120].

Consider an upright cylindrical vessel bounded by no-slip walls (simulations in this geometry are considered much later in Chapter 7). The cylinder height and diameter are both H. As before, the bulk is geostrophic, and Ekman layers are found next to the top and bottom plates. Let us assume that the geostrophic flow has a negative constant vorticity ω_b. Because of the Ekman suction, there is a net $\mathcal{O}(Ek^{1/2})$ radial outward flux found in each of the Ekman layers. These fluxes flow into the Stewartson layer on the sidewall, which hence must contain an $\mathcal{O}(Ek^{1/2})$ vertical flux.

In Refs. [119–121], it is shown that a layer of thickness

$$\delta_{S,1/4} \sim HEk^{1/4} \tag{2.46}$$

can carry the $\mathcal{O}(Ek^{1/2})$ vertical flux and, moreover, match the $\mathcal{O}(1)$ bulk flow. However, this layer cannot subsequently connect to the sidewall where $v = 0$. Instead, an additional layer is found within the $Ek^{1/4}$ layer. The extra layer has a thickness

$$\delta_{S,1/3} \sim HEk^{1/3} \tag{2.47}$$

from the sidewall. The flows inside these two layers close the circulation set up by the Ekman layers.

2.8. Convective turbulence

In Section 2.6 we discussed RRBC in the limit of high rotation rates, which led to a simplified description of the flow where its temporal and spatial variations were neglected. Nevertheless, large-scale geostrophic flows in nature can exhibit turbulent behaviour at smaller scales. In this section, we introduce some useful definitions of convective turbulence.

In rotating Rayleigh–Bénard convection, the flow becomes turbulent when the temperature difference between the bottom/top plates is sufficiently large. The energy introduced into the system, in the form of buoyant production, is transferred to ever smaller length scales up until it is dissipated by viscosity at the Kolmogorov length scale (defined below). Thus, in equilibrium, a continuous input of energy is matched by dissipation. The rate of dissipation of kinetic energy ϵ_u and of thermal variance ϵ_θ are [122], in dimensionless form:

$$\epsilon_u = \sqrt{Pr/Ra}\,|\boldsymbol{\nabla u}|^2\,, \tag{2.48}$$

$$\epsilon_\theta = \frac{1}{\sqrt{PrRa}}\,|\boldsymbol{\nabla} T|^2\,, \tag{2.49}$$

respectively. The corresponding smallest, active length scales for energy and thermal dissipation are given by the (nondimensionalised) Kolmogorov and Batchelor length scales [122]

$$\eta_K = \left(\frac{Pr}{Ra}\right)^{3/8} {\epsilon_u}^{-1/4}, \tag{2.50}$$

$$\eta_B = \eta_K Pr^{-1/2}. \tag{2.51}$$

In direct numerical simulations, as those performed in this study, these length scales determine the grid resolution. Namely, the grid spacings should be small enough so that these lengths are still resolved (see Section 3.5).

The local dissipation rates, ϵ_u and ϵ_θ, are a function of the vertical position (and the radial position, in cylindrical geometries). In particular, near the boundaries they may attain considerably larger values than in the bulk. Exact relations for their global (volume-averaged) values can be derived for (non)rotating Rayleigh–Bénard convection as [123, 124]

$$\langle\epsilon_u\rangle_{V,t} = \frac{Nu - 1}{\sqrt{PrRa}} \tag{2.52}$$

$$\langle\epsilon_\theta\rangle_{V,t} = \frac{Nu}{\sqrt{PrRa}} \tag{2.53}$$

where $\langle\cdot\rangle_{V,t}$, as before, denotes averaging over the entire fluid volume and in time.

Equations (2.52) and (2.53) provide two estimates for the convective heat transport Nu, which can be compared to those given by Eqs. (2.24) and (2.25). The agreement of these estimates provides further validation of the accuracy of the simulations, as it is discussed in Section 3.5.

Chapter 3

Numerical methods

In this chapter we introduce the numerical methodology used in this thesis. First, we present the governing equations of rotating Rayleigh–Bénard convection in dimensionless form, which are solved by means of direct numerical simulations. We motivate the use of three codes for the simulations: a single-grid Cartesian code, a multiple-grid Cartesian code, and a (single-grid) cylinder code. A detailed description of these codes, as well as details on their performance, is provided. We then discuss the domain aspect-ratio, boundary conditions and initial conditions, and describe the validation process of the numerical results. In the last section, we present a complete list of the explored simulation cases.

3.1. Direct numerical simulations

The set of equations of motion, in dimensionless form, to be solved numerically are

$$\frac{\partial \boldsymbol{u}}{\partial t} + (\boldsymbol{u}\cdot\boldsymbol{\nabla})\,\boldsymbol{u} + \frac{1}{Ro_{\mathrm{C}}}\hat{\boldsymbol{z}}\times\boldsymbol{u} = -\boldsymbol{\nabla}p + \sqrt{\frac{Pr}{Ra}}\nabla^2\boldsymbol{u} + T\hat{\boldsymbol{z}}, \tag{3.1}$$

$$\frac{\partial T}{\partial t} + (\boldsymbol{u}\cdot\boldsymbol{\nabla})\,T = \frac{1}{\sqrt{RaPr}}\nabla^2 T, \tag{3.2}$$

$$\boldsymbol{\nabla}\cdot\boldsymbol{u} = 0. \tag{3.3}$$

where the parameters Ra, Pr and Ro_{C} are given by Eqs. (2.15), (2.16) and (2.18), respectively. The direct numerical simulations (DNSs) are performed using three codes, all of them based on the principal setup of the Verzicco code [125, 126], well-known in the convection community. Two of them solve Eqs. (3.1) to (3.3) in a Cartesian domain with periodic lateral boundaries. This setup is relevant to natural settings where the horizontal dimensions are much larger than the vertical. The last code simulates the flow confined in a cylinder. This geometry is widely used in laboratory experiments of rotating Rayleigh–Bénard convection.

The difference between the two Cartesian codes lies in their approach to resolve the temperature field: one of them resolves both velocity and temperature on a single grid, whereas the other resolves velocity on a coarse grid and temperature on a finer grid. This distinction is closely related to the diffusive properties of the fluid, parametrised by the Prandtl number. More specifically, Eqs. (2.50) and (2.51) provide the smallest active length scales for velocity and temperature fluctuations, i.e. the Kolmogorov length scale η_K and the Batchelor length scale η_B, respectively. Equation (2.51) reveals that $\eta_K < \eta_B$ for fluids with low Prandtl number $Pr < 1$, whereas η_B is smaller for high $Pr > 1$. In other words, fluids with relatively lower momentum diffusion (i.e. $\nu < \kappa$) exhibit smaller *flow* features, whilst relatively larger momentum diffusion instead leads to smaller *temperature* features. The latter property is exploited by the multiple-grid code mentioned above, which uses a fine grid to resolve the smaller temperature features, and a coarser grid to resolve the velocity field (i.e. all three velocity components). In conclusion, we use the single-grid code to simulate low-Pr fluid flows, and the multiple-grid code for cases at high Pr; both of them, again, for a Cartesian geometry with periodic lateral boundaries.

3.2. DNS codes

Single-grid Cartesian code

For cases at low Prandtl number ($Pr < 1$), we use a version of the original Verzicco cylinder convection code [125, 127] adapted to a Cartesian domain. Most of the numerical approaches remain the same. Equations (3.1) to (3.3) are discretised by second-order finite-differences on a staggered grid. For the time advancement of the discretized system, the time-step size is computed dynamically by maintaining the stability limit $CFL < \sqrt{3}$, required by the third-order Runge–Kutta scheme. The non-linear terms are treated explicitly in time, and the viscous/diffusive terms implicitly. The Poisson equation for pressure is solved with a 2D Fast Fourier Transform in the periodic directions and a direct tridiagonal solver in the vertical direction.

Multiple-grid Cartesian code

For simulation cases at high Prandtl number ($Pr \geq 1$), we use the same code described before with an extension, the multiple-grid strategy detailed in Ref. [126]. The numerical scheme stays the same, but now the temperature field is evaluated on a grid with high spatial resolution, whilst the velocity field is resolved on a coarser grid. In this way, the unnecessary computational overhead produced by integrating both fields on a single grid tailored to the most demanding variable is avoided. In particular, the multiple-grid Cartesian code allows to refine the grid for temperature in the x-, y- and z-direction independently, through the refinement factors m_x, m_y and m_z. In this research we consider Cartesian domains with lateral sides of equal length, thus $m_y = m_x$. The refinement factors for temperature, relative to the grid for velocity, can then be selected based on the reference value provided by the ratio $\eta_K/\eta_B = Pr^{1/2}$ (see Eq. (2.51)) and making sure to allocate an appropriate number of grid points within the thermal boundary layers (discussed in detail in Section 3.5). A multiple resolution strategy is also used in the time integration in order to maintain the stability of the temperature field on the finer grid. The optimal refinement factor for time coincides with $\max(m_x, m_y, m_z)$. The multiple-grid method becomes more advantageous as the thermal diffusivity κ decreases with respect to the kinematic viscosity ν, therefore it is particularly well suited for high-Pr fluid flows (see Eq. (2.16)).

Cylinder code

The cylinder code is an updated version of the original Verzicco code [125] with extensions for better parallel performance. The finite-difference discretisation of the governing equations is done in cylindrical coordinates as further detailed in [125, 127]. This numerical setup is aimed to replicate the conditions of the laboratory experiment TROCONVEX [76, 128]. The comparison of simulation results with those from the experimental setup are presented in Chapter 7.

3.3. Performance

The simulations are performed on the Dutch national supercomputer: Cartesius, which consists of 47,776 Intel® Xeon® CPU cores (processor frequency of 2.4-2.6 GHz) [129]. To determine the optimum number of CPU cores to use per run, we evaluate the real-time performance (iterations per minute) and CPU-time performance (iterations per CPU-hour) of the codes as a function of the number of cores. The results of this performance assessment are shown in Fig. 3.1. We use 384 cores (or 16 so-called thin nodes) on Cartesius for simulations using the single-grid Cartesian code, 192 cores (or 6 so-called fat nodes) for cases using the multiple-grid Cartesian code, and 192 cores (or 8 thin nodes) for cases using the cylinder code. It can be observed in Fig. 3.1 that these numbers of CPU cores provide an appropriate trade-off between real-time and CPU-time performance. For reference, the example case shown in Fig. 3.1(a), which, recall, is carried out at low Pr (specifically at $Pr = 0.1$),

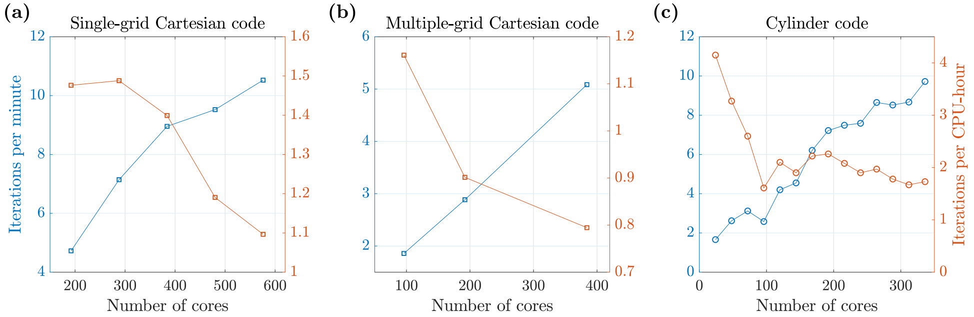

Figure 3.1.: *Real-time performance (iterations per minute) and CPU-time performance (iterations per CPU-hour) of the numerical codes as a function of the numbers of CPU cores. The tests are carried out using (a) the single-grid Cartesian code with* $640 \times 640 \times 1280$ *grid points, (b) the multiple-grid Cartesian code with* $384 \times 384 \times 768$ *grid points for velocity and refinement factor of 2 (i.e.* $768 \times 768 \times 1536$ *points) for temperature (refinement factor for time is also 2), and (c) the cylinder code with* $769 \times 351 \times 1025$ *grid points in the azimuthal, radial and vertical direction.*

requires about 430,000 CPU-hours to simulate the flow over 500 convective time units (approximately 600,000 iterations). This is about 1.5 months on 384 CPU cores. This low-Pr case is amongst the ones with lowest resolution (see Table 3.1 at the end of the chapter for a complete list of the simulation cases at $Pr = 0.1$). In general, the computational resources for one of our simulation cases ranges between 150,000 and 650,000 CPU-hours to be completed.

3.4. Numerical setup, transient state and statistical equilibrium

For all simulations the domain aspect ratio $\Gamma = W/H$ is selected to permit a sufficiently large sampling of convective structures, whose characteristic length scale ℓ_c is given by Eq. (2.21). This procedure ensures the convergence of spatially averaged statistics. At low Pr, we use domains of size $10\ell_c \times 10\ell_c \times 1$ (normalised by the domain height H). As discussed in Sections 3.1 and 3.2, the multiple-grid strategy allows to simulate high-Pr fluid flows much more efficiently compared to the single-grid Cartesian code. This facilitates the exploration of wider domains of size $20\ell_c \times 20\ell_c \times 1$ at high Pr. Equivalent low-Pr simulations using the single-grid code would demand four times more computational resources than in their current setup. For instance, the case in Fig. 3.1(a) would require a minimum of 1.7 million CPU-hours to be completed instead of 430,000 (i.e. a minimum of 6 months instead of 1.5 months on 384 cores). Whilst such expensive lasting runs are certainly possible, we divert our limited computational resources ($\sim$ 8 million CPU-hours per year) to the exploration of a wider range of parameter values. Finally, in a cylindrical geometry, $\Gamma = D/H$, where D is the diameter of the cylinder. The simulations in this geometry are aimed to replicate the operating conditions of the laboratory experiment TROCONVEX in our group, for which $\Gamma = 0.2$. We thus use this aspect ratio instead of $\Gamma = 20\ell_c = 0.224$ (at $Ek = 10^{-7}$).

At the top and bottom walls of both Cartesian and cylindrical domains, we consider the following impenetrable, no-slip boundary conditions:

$$\boldsymbol{u} = \mathbf{0} \text{ at } z = 0, 1. \tag{3.4}$$

Nonetheless, for comparison, we do simulate some selected Cartesian cases with stress-free boundary conditions

$$\frac{\partial u}{\partial z} = \frac{\partial v}{\partial z} = 0 \text{ and } w = 0 \text{ at } z = 0, 1. \tag{3.5}$$

On the other hand, for all cases (no-slip and stress-free), we consider the constant-temperature boundary conditions

$$T = 1 \text{ at } z = 0 \text{ and } T = 0 \text{ at } z = 1. \tag{3.6}$$

For simulations in a cylinder, the sidewalls are also no-slip, and adiabatic:

$$\frac{\partial T}{\partial r} = 0 \text{ at the sidewalls,} \tag{3.7}$$

where r represents the radial coordinate in the cylinder.

The simulations are started either from the fluid at rest (and a linearly unstable temperature profile perturbed by small-amplitude random noise) or from an already developed turbulent flow from a previous simulation. In either case, the flow exhibits an initial transient state, albeit shorter when the latter approach is used, allowing savings in computation time. Figure 3.2 shows an example where the fluid is started at rest. Figure 3.2(a) plots the root-mean-square (RMS) of all three velocity components as a function of time, where, for instance, $u_{\mathrm{RMS}} = \sqrt{\langle u^2 \rangle_V}$ with $\langle \cdot \rangle_V$ denoting volume averaging; a similar procedure yields v_{RMS} and w_{RMS}. Figure 3.2(b) shows the convective heat transfer measured through five different methods (discussed in Section 3.5 in detail) also as a function of time. From the initial stagnant state, the system takes a few time units before convection starts. Once the flow is established, a large overshoot peak is observed. In the following time units, the system describes a period of adjustment where the distinct measurements start to converge, statistically, towards a common value. Notice that the time advancement is carried out with respect to the convective time unit $\tau_{\mathrm{ff}} = H/U_{\mathrm{ff}}$. As the system evolves in time, the velocity fluctuations and heat transport converge to a statistical equilibrium state, at approximately 100 convective time units in Figs. 3.2(a) and 3.2(b). From this point on, the time averaging of several physically relevant quantities starts. The flow is simulated for long enough to ensure statistical converge of these quantities. It is observed (in the literature and in our research) that relevant statistical quantities (such as mean, variance, skewness and kurtosis of several physical quantities) converge over simulation times of the order of 10^2 convective time units. The quality of the convergence of the heat transport measurements, for example, is discussed in the next section.

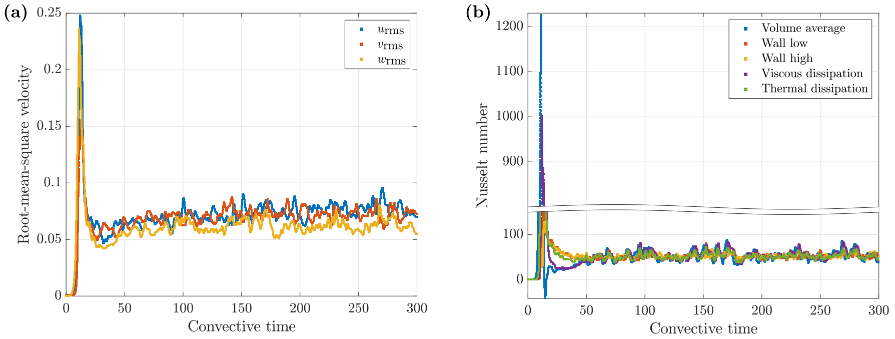

Figure 3.2.: *(a) Root-mean-square of all velocity components and (b) heat transport measurements through five different methods (discussed in Section 3.5) as a function of time. The initial transient behaviour displayed by the time series converges to a statistically stationary state after approximately 100 convective time units. The data is shown for a case at* $Pr = 0.1$, $Ra = 10^{10}$ *and* $Ro_C = 0.253$, *nonetheless similar curves are observed for the rest of the simulation cases.*

3.5. Validation

The Cartesian codes described above in Section 3.2 consider a grid with uniform horizontal spacing and non-uniform vertical distribution. In this way, a larger density of grid points can be attained near the walls in order to resolve the thin boundary layers. We verify, *a posteriori*, that a minimum of 11 grid points is allocated within the thinner (Ekman or thermal) boundary layer, which is enough to appropriately resolve it.

To validate the bulk resolution, we compare the grid spacing with the Kolmogorov and Batchelor length scales, η_K and η_B. The range of scales that need to be accurately represented is dictated by the physics. In turbulent flows, it is well-known that reliable statistics are achieved for resolutions *of the order of* η_K, as they accurately capture most of the energy dissipation [130, 131]. We estimate height-dependent values of η_K and η_B by computing the time- and plane-average of the energy dissipation rate ϵ_u (given by Eq. (2.48)) and employing Eqs. (2.50) and (2.51), respectively. We find that for low-Pr runs the bulk resolution is $\Delta z_u/\eta_K < 3$ and $\Delta z_\theta/\eta_B < 1$, where Δz_u and Δz_θ are the vertical grid spacing for the velocity and temperature field, respectively. For simulations at high Pr, we find $\Delta z_u/\eta_K < 3$ and $\Delta z_\theta/\eta_B < 3.7$. For all cases the horizontal grid spacing is smaller than the vertical one.

In the cylinder code the points are evenly spaced along the azimuthal direction. In the radial and axial directions the grids become finer near the sidewalls, more so in the axial direction given that the Ekman boundary layers forming near bottom and top plates are significantly thinner than the sidewall boundary layer. We find that there are 15 grid points within the Ekman layers. For the bulk resolution we find that $\Delta z_u/\eta_K < 3.5$ and $\Delta z_\theta/\eta_B < 4$. We see that the largest grid-point separation never exceeds four times the local η_B, as deemed adequate in [127], but for the largest-Ra simulation where the maximal grid-point separation always remains below five times the local η_B.

The time-step size for the time integration is also subject to physical constraints. It can be shown that at $Ro_\mathrm{C} < 1$ (and at any Pr), the shortest time scale is the rotational time scale $\tau_\Omega = 1/(2\Omega)$. We must therefore ensure that $\tau_\Omega = Ro_\mathrm{C}\tau_\mathrm{ff}$ is resolved. We do so by setting the maximum time-step size to be smaller than Ro_C. For runs where $Ro_\mathrm{C} > 1$, the smallest time scale is τ_ff, which is immediately resolved as this is the time unit over which the time integration of the governing equations is carried out.

To further confirm the adequacy of the grid, we compute the time-averaged convective heat transfer Nu in five different ways:

- Two of the them at the walls: as the plane-averaged wall-normal temperature gradient at the bottom and at the top wall, given by Eq. (2.24).
- As the volume-averaged convective flux, as in Eq. (2.25).
- And the last two from the dissipation rates of kinetic energy, as in Eq. (2.52), and of thermal variance, as in Eq. (2.53) [123].

These estimates are susceptible to insufficient resolution. Specifically, the Nusselt numbers calculated near the walls are susceptible to under-resolution of the boundary layers, whereas Nu computed using velocity and temperature gradients (as in the last two methods) are greatly affected by inadequate resolution of the velocity and temperature field, respectively. For most of our cases (about two-thirds of them) the maximum difference between a given Nu and the mean of all Nu's converges to better than 2% (see, e.g., Fig. 3.3), the others converge to better than 5%. The relatively larger discrepancy is caused by slow convergence of the heat transfer measurements. Two causes for this are identified. First, for near-onset cases the flow is quasi steady, and thus its time evolution is rather slow. Specifically, the Nusselt number measurements converge for simulation times of the order of 10^3 convective time units, instead of 10^2 as seen for the turbulent case in Fig. 3.3. Second, for turbulent flows the increased temporal- and spatial-resolution requirements lead to very demanding computations. The statistical equilibrium state of these cases is then simulated for about 100 convective times units, which requires about 600,000 CPU-hours. We refer the reader to the discussion presented in Section 3.3.

Finally, our results in cylindrical domains are moreover validated by the excellent agreement with the experimental measurements. We present these results in Chapter 7.

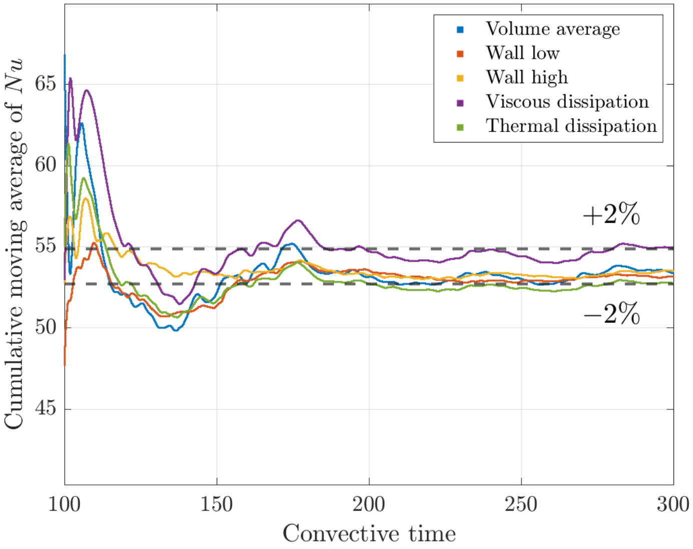

Figure 3.3.: *Cumulative moving average of the various Nusselt numbers in Fig. 3.2(b). The averaging is done in the statistically stationary state, i.e. for times larger than 100 convective time units. The horizontal dashed lines serve as a reference of ±2% of the average of all Nusselt numbers.*

3.6. Summary of simulation cases

Our RRBC survey spans over a wide range of parameter values that jointly resolve over three decades of supercriticality Ra/Ra_c. This allows us to identify distinct flow states: from quasi-steady cellular convection to more turbulent states. Specifically, we identify rotating convection regimes displaying cells (C), convective Taylor columns (T), plumes (P), large-scale vortices (LSVs) and rotation-affected (RA) convection. These flow structures will be described in more detail in Chapter 5. A complete list of the cases investigated can be found in Table 3.1 for simulations in a horizontally periodic layer, and in Table 3.2 for cases confined in a cylinder. The tables also list the domain aspect ratio, numerical resolution and flow type.

Pr	Ek	Ra	Ro_C	Ra/Ra_c	Γ	N_x	N_z	m_x	m_z	Flow
0.1	2.00×10^{-7}	1.00×10^{10}	0.063	14.48	0.302	1024	1408	-	-	LSV
0.1	2.24×10^{-7}	1.00×10^{10}	0.071	16.84	0.314	1024	1408	-	-	LSV
0.1	2.50×10^{-7}	1.00×10^{10}	0.079	19.50	0.326	768	1280	-	-	LSV*
0.1	3.00×10^{-7}	1.00×10^{10}	0.095	24.87	0.346	768	1280	-	-	LSV
0.1	4.00×10^{-7}	1.00×10^{10}	0.126	36.49	0.381	640	1280	-	-	LSV
0.1	8.00×10^{-7}	1.00×10^{10}	0.253	91.95	0.480	640	1280	-	-	RA
0.1	1.05×10^{-6}	1.00×10^{10}	0.332	132.14	0.526	768	1280	-	-	RA
0.1	2.80×10^{-6}	1.00×10^{10}	0.885	488.65	0.729	1088	1280	-	-	RA
0.1	6.00×10^{-6}	1.00×10^{10}	1.897	1349.95	0.940	1408	1280	-	-	RA
5.5	3.00×10^{-7}	5.50×10^{9}	0.009	1.27	0.323	256	640	2	1	C
5.5	3.00×10^{-7}	8.00×10^{10}	0.011	1.85	0.323	256	640	2	1	C
5.5	3.00×10^{-7}	1.00×10^{10}	0.013	2.31	0.323	384	640	2	1	T
5.5	3.00×10^{-7}	1.50×10^{10}	0.016	3.46	0.323	384	640	2	1	T
5.5	3.00×10^{-7}	2.00×10^{10}	0.018	4.62	0.323	384	640	2	1	T
5.2	1.00×10^{-7}	1.40×10^{11}	0.016	7.47	0.224	384	640	2	2	P*
5.2	1.00×10^{-7}	2.10×10^{11}	0.020	11.20	0.224	384	640	2	2	P
5.2	1.00×10^{-7}	3.20×10^{11}	0.025	17.07	0.224	512	640	2	2	P*
5.2	1.00×10^{-7}	6.00×10^{11}	0.034	32.01	0.224	512	640	2	2	P†
5.2	1.00×10^{-7}	9.50×10^{11}	0.043	50.68	0.224	640	896	2	2	LSV
5.2	1.00×10^{-7}	1.50×10^{12}	0.054	80.03	0.224	768	1024	2	2	LSV
100	3.00×10^{-7}	1.30×10^{11}	0.011	30.01	0.323	384	512	3	3	P
100	3.00×10^{-7}	2.10×10^{11}	0.014	48.48	0.323	384	512	3	3	P
100	3.00×10^{-7}	3.40×10^{11}	0.017	78.49	0.323	512	512	3	3	P
100	3.00×10^{-7}	6.00×10^{11}	0.023	138.50	0.323	512	768	3	3	P
100	3.00×10^{-7}	9.50×10^{11}	0.029	219.30	0.323	512	768	3	3	P
100	3.00×10^{-7}	1.50×10^{12}	0.037	346.26	0.323	512	768	3	3	P
100	3.00×10^{-7}	2.50×10^{12}	0.047	577.10	0.323	384	768	4	4	P

*Also independently simulated with stress-free boundaries.

†Even though there is evidence of upscale energy transfer, no LSVs develop.

Table 3.1.: *Parameters for the simulations: Prandtl number Pr, Ekman number Ek, Rayleigh number Ra, convective Rossby number Ro_C and supercriticality Ra/Ra_c. The slight difference in Pr between the $Pr \approx 5$ simulation series is for comparison with (ongoing) experiments in our group [76,128]. Also included, the domain aspect-ratio Γ, number of grid points N_x, $N_y = N_x$ and N_z used to resolve the velocity field, and refinement factors m_x, $m_y = m_x$ and m_z used for temperature. For instance, at $Pr = 100$, $Ek = 3 \times 10^{-7}$ and $Ra = 2.5 \times 10^{12}$, a coarse grid with $384 \times 384 \times 768$ points resolves velocity, whereas a finer grid with $1536 \times 1536 \times 3072$ is used for temperature. The last column indicates the flow morphology in each case: convective cells (C), convective Taylor columns (T), plumes (P), large-scale vortices (LSVs) or rotation-affected convection (RA). All cases are simulated with no-slip top/bottom boundaries. Some cases, denoted with the superscript "$*$", are also independently simulated with stress-free boundaries.*

Pr	Ek	Ra	Ro_{C}	Ra/Ra_c	Γ	$N_\theta \times N_r \times N_z$
5.2	1.00×10^{-7}	5.00×10^{10}	0.010	2.67	0.200	$769 \times 351 \times 1025$
5.2	1.00×10^{-7}	7.00×10^{10}	0.012	3.73	0.200	$769 \times 351 \times 1025$
5.2	1.00×10^{-7}	1.40×10^{11}	0.016	7.47	0.200	$769 \times 351 \times 1025$
5.2	1.00×10^{-7}	3.20×10^{11}	0.025	17.07	0.200	$769 \times 351 \times 1025$
5.2	1.00×10^{-7}	4.30×10^{11}	0.029	22.94	0.200	$769 \times 351 \times 1025$

Table 3.2.: *Parameters for simulations in cylindrical domains: Pr, Ek, Ra,Ro_C, Ra/Ra_c and Γ are as in Table 3.1. The last column displays the number of grid points N_θ, N_r and N_z in the azimuthal, radial and vertical direction, respectively.*

Chapter 4

Force balances

In this chapter we investigate the interplay between the governing forces of RRBC as a function of the supercriticality Ra/Ra_c of the flow. We analyse the force balance, and changes therein between flow regimes, in the bulk and near the no-slip walls. We find that geostrophy is indeed the primary force balance in the so-called geostrophic regime, but that this rotational constraint is lost at larger values of Ra/Ra_c. As a result, the flow displays a transition to a rotation-affected state of convection. Near the no-slip walls, the flow is also found to be dominated by geostrophy in the geostrophic regime. Although, remarkably, inertia becomes increasingly more important near the boundaries compared to the bulk.

4.1. Introduction

In Chapter 1 (also in Tables 3.1 and 3.2) we anticipated the observation of several different flow states for the explored parameter values. In general, the parameter space can be divided into three main regimes: “rotation-dominated”, “rotation-affected” and “non-rotating” regime. As their names suggest, the partition is based on the importance of rotational forces in the flow dynamics. In particular, in the rotation-dominated regime, Coriolis forces exert a dominant role on the flow, that is primarily balanced by pressure-gradient forces. As a result, the flow is prominently geostrophic [33, 41, 51, 132]. This regime, which is therefore also known as the “geostrophic” regime, can be moreover subdivided into several other regimes. They display cells, convective Taylor columns, plumes and geostrophic turbulence (where large-scale vortices may develop). In Fig. 4.1 we present visualisations of the temperature fluctuations in these regimes (from Ref. [45]). The cellular regime (in Fig. 4.1(a)) is typically found in the range $1 \lesssim Ra/Ra_c \lesssim 2$ and consists of quasi-steady cells with horizontal size ℓ_c given by Eq. (2.21) [81]. Convective Taylor columns (Fig. 4.1(b)) manifest at larger values of Ra/Ra_c, and consist of vortical columns surrounded by “shields” of opposite vertical vorticity and opposite temperature

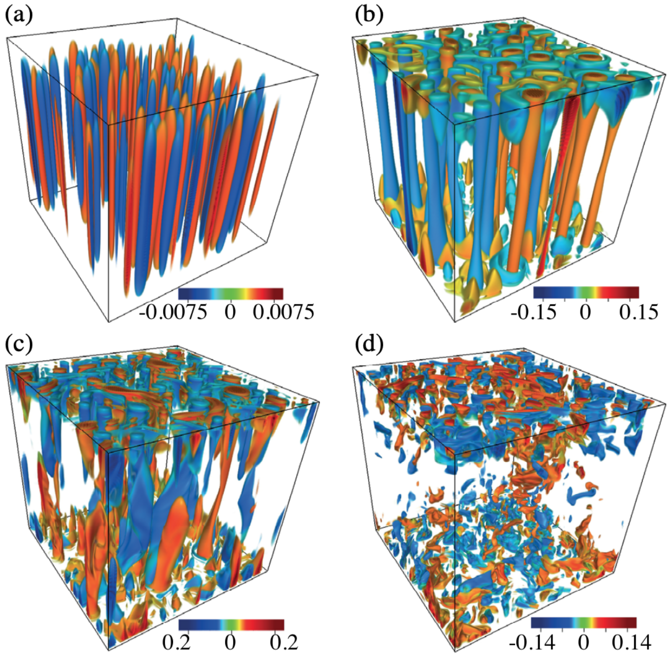

Figure 4.1.: *Temperature fluctuations in direct numerical simulations at $Ek = 10^{-7}$ with no-slip boundary conditions. (a) Cells at $Ra/Ra_c \approx 1.1$ and $Pr = 1$, (b) convective Taylor columns at $Ra/Ra_c \approx 2.9$ and $Pr = 7$, (c) plumes at $Ra/Ra_c \approx 8$ and $Pr = 7$, (d) geostrophic turbulence at $Ra/Ra_c \approx 10.3$ and $Pr = 1$. The domains are stretched horizontally by a factor of 4.5 for better visibility. Source: [45].*

(stronger near the walls) [33, 40, 41, 63, 72, 77, 88–91]. With increasing Ra/Ra_c, the shields are weaker and the vortical columns interact with each other. As a consequence, their vertical coherence is affected, leading to the development of plumes (Fig. 4.1(c)) [33, 41, 72, 88]. In the geostrophic turbulence regime (Fig. 4.1(d)), the flow becomes turbulent, albeit it does remain rotationally constrained. The combination leads to a quasi-two-dimensional dynamics that enables the transfer of kinetic energy from small to large spatial scales. This upscale energy transfer can lead to the development of large-scale vortices (LSVs) in the flow [33, 41, 44–46, 50, 58, 92]. We will discuss several aspects of this phenomenon in Chapter 6.

To identify flow regimes in our simulation cases we consider the force balance of the flow (to be discussed in Section 4.3) and its statistical properties (addressed in Chapter 5). In our set of simulations at $Pr \approx 5$, we also observe the regimes of cells, convective Taylor columns, plumes and large-scale vortices. We present visualisations of the temperature fluctuations in these regimes in

Figs. 4.2(a) to 4.2(d), respectively. The large-scale vortices in Fig. 4.2(d) are better visualised in terms of the horizontal kinetic energy of the flow, as we show in Fig. 6.3(c). All of our simulation cases at $Pr = 100$ lie within the plumes regime; we show two example cases in Figs. 4.2(e) and 4.2(f). For the exploration of highly supercritical regimes we make use of a lower Prandtl number, $Pr = 0.1$. The reason is that sufficiently small values of Pr (i.e. smaller than 0.68, see Eq. (2.20)) act to decrease the critical Rayleigh number for onset of convection Ra_c. Thus, for a given value of Ra and Ek, low-Pr fluid flows can achieve a larger degree of supercriticality than those at high Pr. In other words, inertial effects are amplified in low-Pr fluids [41,74]. At $Pr = 0.1$ we also observe large-scale vortices and, at larger Ra/Ra_c, we identify rotation-affected convection; see Figs. 4.2(g) and 4.2(h), respectively. Just like at $Pr \approx 5$, LSVs are more clearly visualised in terms of the horizontal kinetic energy of the flow; we show this in Fig. 6.3(a). In the rotation-affected regime, rotation no longer exerts a dominant role, and thus convection becomes more three-dimensional. In the particular case displayed in Fig. 4.2(h), the large parcel of hot fluid (red patch at the top) and large parcel of cold fluid (blue patch) resemble a large overturning cell similar to that observed in non-rotating convection. However, the magnitude of the Coriolis force is still appreciable as we shall discuss in Section 4.3. Finally, in order to discuss the observed flow regimes with increasing supercriticality, we present our results starting from simulations at $Pr \approx 5$ and 100, and then at $Pr = 0.1$.

Numerous investigations on the interplay amongst the forces governing RRBC are primarily focussed on the determination of the relevant forces in geophysical and astrophysical settings. These studies aim to determine the dominant force balance of the large-scale flows in order to estimate the characteristic flow velocity and length scale of convection [42,133–139]. However, the role of subdominant forces has not been addressed extensively. In particular, a complete view of the interplay between all forces is required to effectively characterise the flow and the transitions between regimes. In this chapter, we focus on fully understanding the force balance, from the leading contributors to the subdominant forces. Previous efforts have been made in this direction in the field of rotating magneto-convection [140–145]. Self-sustained convective dynamos in planetary systems operate in a rotationally constrained regime. There, a balance is thought to hold between the Coriolis, pressure-gradient, buoyancy and Lorentz forces, also known as *magneto-Archimedean-Coriolis* (MAC) balance. Hence, many studies seek to determine the specific parameter values and length scales at which the contribution of viscous and inertial forces becomes negligible, and therefore a MAC balance is possible. In our simulations

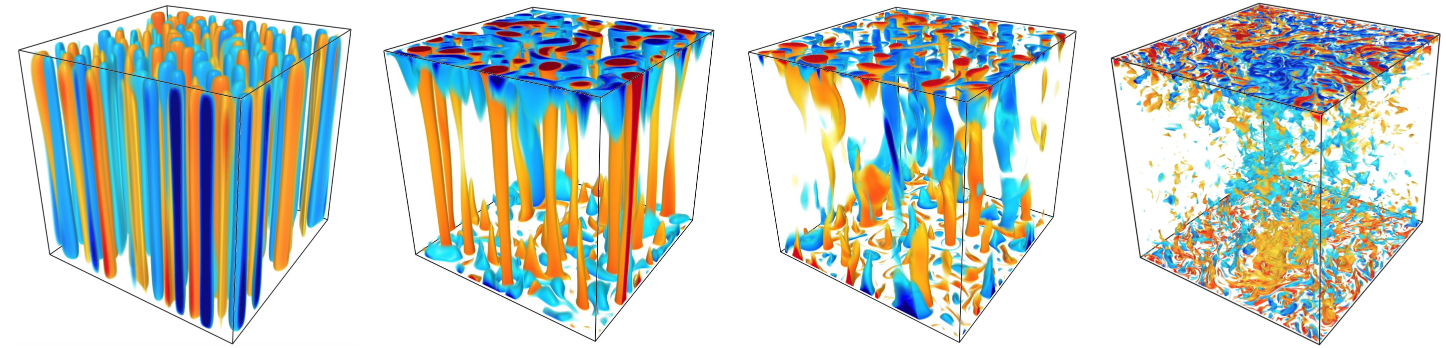

(a) $Pr = 5.5,\ Ra/Ra_c = 1.3$ **(b)** $Pr = 5.5,\ Ra/Ra_c = 3.5$ **(c)** $Pr = 5.2,\ Ra/Ra_c = 7.5$ **(d)** $Pr = 5.2,\ Ra/Ra_c \approx 80$

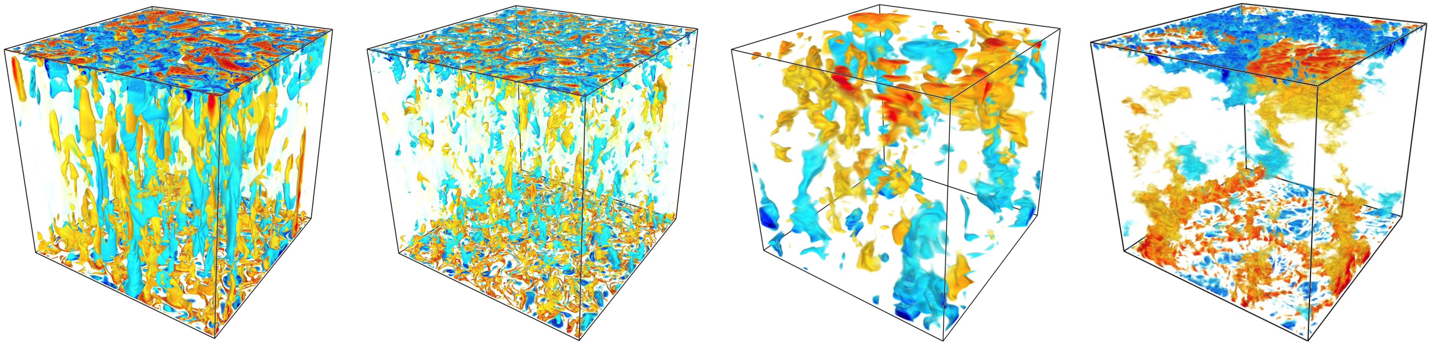

(e) $Pr = 100,\ Ra/Ra_c \approx 78$ **(f)** $Pr = 100,\ Ra/Ra_c \approx 346$ **(g)** $Pr = 0.1,\ Ra/Ra_c \approx 20$ **(h)** $Pr = 0.1,\ Ra/Ra_c \approx 489$

Figure 4.2.: *Temperature fluctuations for selected cases in the regimes of (a) cells, (b) convective Taylor columns, (c,e,f) plumes, (d,g) large-scale vortices and (h) rotation-affected convection. The captions indicate the corresponding Prandtl number Pr and supercriticality Ra/Ra_c. Owing to the low $Ek \sim 10^{-7}$ considered for all cases, the domain aspect ratio $\Gamma = W/H = \mathcal{O}(Ek^{1/3})$ (W and H are its width and height) is smaller than unity, i.e. the computational domains are narrower than they are tall. Thus, for clarity, the domains are stretched horizontally by a factor $1/\Gamma$. The colour scale is chosen to highlight the flow features. Red denotes above-average temperature and blue is for below-average temperature.*

of non-magnetic, rotating convection in a horizontal plane fluid layer, we access both low-supercriticality flow regimes, where viscous effects are expected to be significant, and highly-supercritical regimes, where we foresee an increased importance of inertial forces. Similar low- and high-supercriticality RRBC flows have been studied by means of asymptotically reduced equations [33, 41, 51, 59], valid at $Ek, Ro \to 0$. In these studies the geostrophic regime (where cells, columns, plumes and large-scale vortices manifest) is charted. Here, we assess the force balance of the full Navier–Stokes equations in the geostrophic regime, but also at larger Ra/Ra_c beyond this regime. A particular aspect of the asymptotic studies is the intrinsic consideration of stress-free top and bottom boundaries. Here, we consider the case of no-slip walls. This type of boundary condition is specially relevant to realistic settings such as laboratory experiments and large-scale flows in nature. Yet we do consider some stress-free cases for comparison (simulation cases denoted with the superscript “$*$” in Table 3.1).

This chapter is structured as follows. In Section 4.2 we briefly introduce the equations used to calculate the magnitude of the governing forces. In Section 4.3 we discuss the estimated values of the forces at mid-height plotted as a function of the supercriticality Ra/Ra_c. Moreover, we identify the characteristic force balance of the distinct flow regimes. In Section 4.4 we investigate the interplay amongst the forces close to the walls, where the no-slip boundary condition is imposed. Finally, in Section 4.5 we present our conclusions.

4.2. Magnitudes of the governing forces

We begin our analysis by explicitly calculating the various forces governing rotating convection. From Eq. (3.1), in dimensionless form, the inertial, Coriolis, pressure-gradient, viscous, and buoyancy forces are

$$\boldsymbol{F}_I = (\boldsymbol{u} \cdot \boldsymbol{\nabla})\boldsymbol{u}, \tag{4.1}$$

$$\boldsymbol{F}_C = \frac{1}{Ro_{\mathrm{C}}} \hat{\boldsymbol{z}} \times \boldsymbol{u}, \tag{4.2}$$

$$\boldsymbol{F}_P = \boldsymbol{\nabla} p, \tag{4.3}$$

$$\boldsymbol{F}_V = \sqrt{\frac{Pr}{Ra}} \nabla^2 \boldsymbol{u}, \tag{4.4}$$

$$\boldsymbol{F}_B = T \hat{\boldsymbol{z}}, \tag{4.5}$$

respectively. Thus, the geostrophic balance ${Ro_{\mathrm{C}}}^{-1} \hat{\boldsymbol{z}} \times \boldsymbol{u} = -\boldsymbol{\nabla} p$, discussed in Section 2.6, can be written as $\boldsymbol{F}_C = -\boldsymbol{F}_P$. Concretely, we compare the plane-averaged root-mean-square (RMS) value of these forces. That is, for a given force $\boldsymbol{F}(\boldsymbol{x})$ with x-, y- and z-components $F_x(\boldsymbol{x})$, $F_y(\boldsymbol{x})$ and $F_z(\boldsymbol{x})$, the RMS value is here defined as

$$F(z) = \sqrt{\left\langle (F_x - \langle F_x \rangle)^2 + (F_y - \langle F_y \rangle)^2 + (F_z - \langle F_z \rangle)^2 \right\rangle}, \tag{4.6}$$

where $\langle \cdot \rangle$ denotes averaging along the horizontal directions and, therefore, F is a function of the vertical coordinate z only. In practice, the force components are calculated at each grid position on a horizontal cross-section. For that, we consider one single-time volume snapshot well within the statistically stationary state; for other snapshots within this state the results agree within 5% in average. The underlying consideration behind the plane-averaging process is that the flow is statistically homogeneous in the horizontal directions. In other words, it is assumed that the average flow dynamics does not depend on the horizontal coordinate. This is a valid assumption in our horizontally periodic domains. Hence, we are able to evaluate the spatial dependence of the force balance solely in terms of the vertical coordinate. Note that we use the deviations from the mean force components, e.g. $F_x - \langle F_x \rangle$, in order to disregard the underlying mean vertical profiles of pressure and temperature ($\langle p \rangle (z)$ and $\langle T \rangle (z)$; e.g., see Fig. 5.1(a)).

4.3. Force balance in the bulk

In Figs. 4.3(a), 4.3(c) and 4.3(e) we plot the magnitudes of the governing forces as a function of Ra/Ra_c. The plots correspond to our results from simulations at Prandtl numbers $Pr \approx 5$, 100 and 0.1, respectively. The forces are calculated at half the domain height; we find that these results are representative of the bulk dynamics. Figure 4.3(a) shows the forces at $Pr \approx 5$, where we observe cells (C), convective Taylor columns (T), plumes (P) and large-scale vortices (LSVs). The figure shows that in these regimes not only the Coriolis and pressure-gradient forces are larger than the other forces in the flow, but they also are in close balance with each other. Thus, the flows are indeed in geostrophic balance at leading order. This is also observed for plumes at $Pr = 100$, in Fig. 4.3(c), and LSVs at $Pr = 0.1$, in Fig. 4.3(e). The simulation cases with stress-free boundary conditions at $Pr \approx 5$ and 0.1 are also directed by the geostrophic balance, as seen in Figs. 4.3(a) and 4.3(e), respectively. The presence of a leading-order geostrophy balance in rotationally constrained convection is exploited in quasi-geostrophic models [8, 33, 41, 92, 113, 146–153] to simplify the governing equations in the limit of rapid rotation. To further

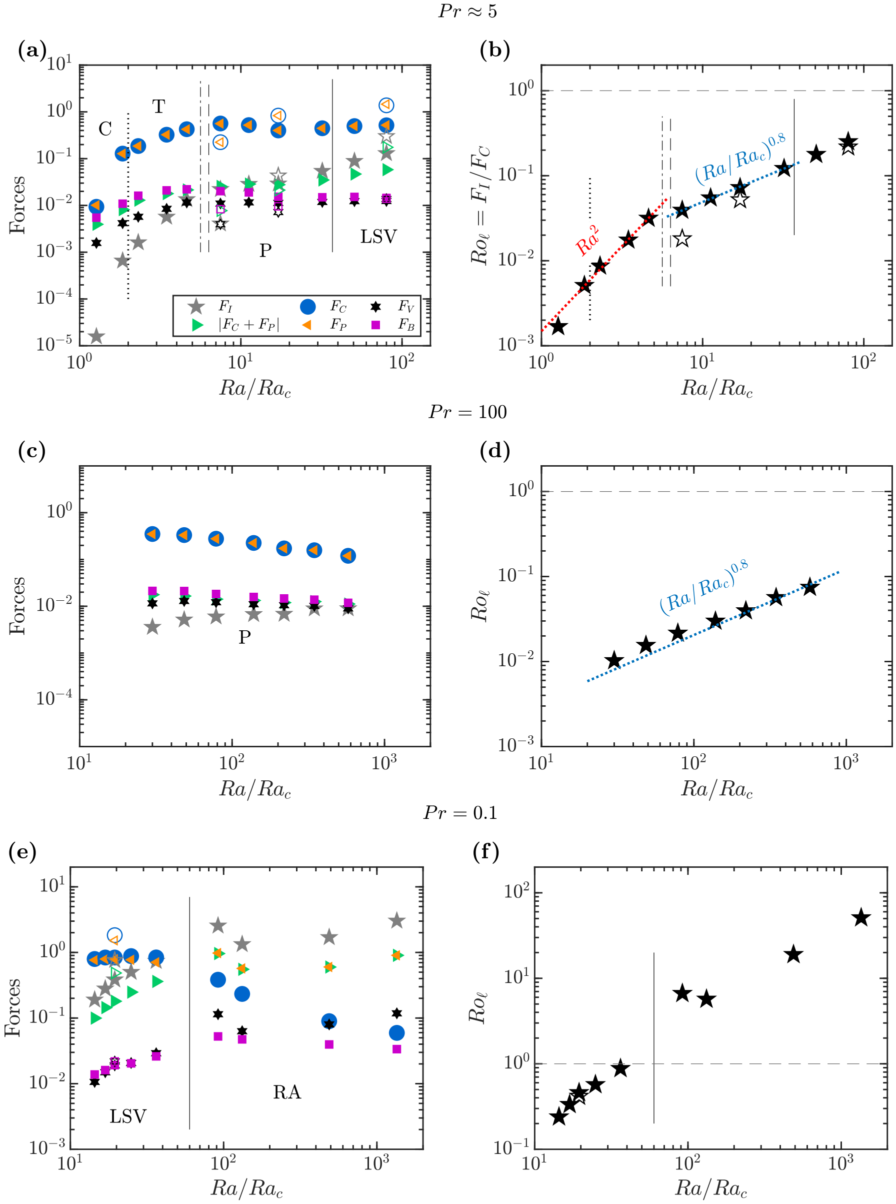

Figure 4.3.: *Force balance (left column) and local Rossby number Ro_ℓ (right column), both at mid-height, as a function of supercriticality Ra/Ra_c for simulations at (a,b) $Pr \approx 5$, (c,d) 100 and (e,f) 0.1. Filled and open symbols correspond to simulations with no-slip and stress-free boundary conditions, respectively. Vertical dotted lines denote our estimated transition between cells (C) and convective Taylor columns (T). Vertical dash-dotted and dashed lines are the predicted transitions between convective Taylor columns (T) and plumes (P) in Ref. [71] and [132], respectively. Vertical solid lines are our estimated transitions between plumes and large-scale vortices (LSVs; at $Pr \approx 5$), and between LSVs and rotation-affected (RA) convection (at $Pr = 0.1$). Horizontal dashed lines indicate $Ro_\ell = 1$, the red dotted line is the predicted scaling in Ref. [42], and the blue dotted line is the least-squares fit of cases with plumes at $Pr \approx 5$.*

illustrate the dominant role of rotation, we directly compute the Rossby number as the ratio of inertial to Coriolis forces $Ro = F_I/F_C$ as a function of Ra/Ra_c. Notice that this Rossby number is different from the *convective* Rossby number Ro_C in Eq. (3.1). Because F_I and F_C represent local estimates of the inertial and Coriolis forces, we henceforth refer to Ro as the *local* Rossby number Ro_ℓ. Figure 4.3(b) shows that $Ro_\ell < 1$ for all cases in the geostrophic regime (i.e. cellular, columnar, plumes and LSVs regimes), which is a clear sign of rotational constraint. Figures 4.3(d) and 4.3(f) reveal the same for plumes at $Pr = 100$ and LSVs at $Pr = 0.1$, respectively. Nevertheless, in Fig. 4.3(f) for $Pr = 0.1$ cases, we see that Ro_ℓ becomes larger than 1 for values of supercriticality larger than 60. This is due to the decrease in strength of the Coriolis force and the increase in inertial force at $Ra/Ra_c > 60$, as evidenced in Fig. 4.3(e). This indicates that the flow transitions to a state where rotation affects the flow, but no longer dominates it. In this so-called regime of rotation-affected (RA) convection, geostrophy does not constitute the primary force balance in the flow. Instead, pressure-gradient and inertial forces are dominant. The green symbols in Fig. 4.3(e) represent the quantity $|F_C + F_P|$, which is only comparable to F_P in this regime because F_C is much smaller; we shall discuss this quantity below. In Fig. 4.3(b), the local Rossby number Ro_ℓ for cells and columns is fitted by the predicted scaling Ra^2 for rotationally constrained convection in Ref. [42] with a root-mean-square error of 3.7%. This scaling is suggested for $RaEk^{3/2} < 10$, or $Ra/Ra_c \lesssim 14$ at $Ek = 3 \times 10^{-7}$, as in our simulations (see Table 3.1). Moreover, the predicted scaling is for a flow in *visco-Archimedean-Coriolis* (VAC) balance, i.e. the triple balance between viscous, buoyancy and rotational forces. Below we confirm that these regimes do exhibit this force balance, and show that it is subdominant in our simulations (see, e.g., Table 4.1). Also in Fig. 4.3(b), a least-squares fit of the Ro_ℓ values for plumes at $Pr \approx 5$ yields a scaling $(Ra/Ra_c)^{0.8}$. This scaling fits the Ro_ℓ data of plumes at $Pr = 100$, too, with an RMS error of about 10%.

Whilst the force balances for cells, columns, plumes and LSVs are led by Coriolis and pressure-gradient forces, Figs. 4.3(a), 4.3(c) and 4.3(e) reveal that other forces (buoyancy, viscous and inertial) also participate in the force balance. The deviations from geostrophic balance, denoted by the difference between Coriolis and pressure-gradient forces $|F_C + F_P|$, are caused by the presence of these forces. This indicates that these geostrophic flows are actually *ageostrophic* at higher order. Namely, a relaxation of the Taylor–Proudman constraint (see Eq. (2.30) in Section 2.6) is permitted at higher order. Figure 4.3(a) shows that for cells and columns, at $Ra/Ra_c < 6$, $|F_C + F_P|$ mostly originates from buoyancy with some contribution of the viscous force, whereas the inertial force remains relatively small. The absence of inertial forces, and thus the presence of a VAC balance in rotationally constrained convection is leveraged in single-mode theories in Refs. [89, 154] to provide an analytical model for the convective Taylor columns. Nonetheless, inertia does increase rapidly with Ra/Ra_c. In fact, at $Ra/Ra_c \gtrsim 6$, inertia becomes part of the subdominant force balance. The participation of inertial forces in this subdominant balance affects the vertical coherence of the flow, which results in its transition from vertically aligned columns to plumes with weaker vertical coherence. For the $Pr = 100$ cases shown in Fig. 4.3(c), the magnitude of the inertial force is smaller due the larger kinematic viscosity of the fluid (relative to its thermal diffusivity). However, inertia becomes increasingly important with Ra/Ra_c, leading to plumes with an ever greater degree of vertical incoherence, as displayed in Figs. 4.2(e) and 4.2(f). In the LSV regime at $Pr \approx 5$ and $Ra/Ra_c \gtrsim 37$, inertia becomes larger than $|F_C + F_P|$, although it does remain smaller than F_C and F_P. This is also observed at $Pr = 0.1$, see Fig. 4.3(e). Whilst inertial forces are the main source of ageostrophy for plumes and LSVs, buoyancy also participates in the force balance. This is more clearly evidenced in Fig. 4.4, where the force balance of cases at $Pr \approx 5$ is decomposed into its horizontal and vertical component (similar results are obtained at $Pr = 0.1$ and 100; combination of the horizontal and vertical components according to Eq. (4.6) results in the full force balance displayed in Fig. 4.3(a)). In Fig. 4.4(a), as expected, the geostrophic balance in all cases is seen to dominate the horizontal force balance, whereas the role of inertia as the primary cause of ageostrophy in the plumes and LSV regimes is also observed. On the other hand, Fig. 4.4(b) reveals that for all cases there is an approximate balance between the buoyancy force and vertical pressure-gradient force. The presence of this so-called hydrostatic balance highlights the importance of buoyancy. It is therefore reasonable to assume that the dynamics of plumes and LSVs results from the balance between the Coriolis, inertial and buoyancy forces, also known as *Coriolis-Inertia-Archimedean* (CIA) balance, with some contribution of the viscous force in the plumes regime. These observations are consistent with results from asymptotic simulations [41]. In Fig. 4.3(e), we see that at $Ra/Ra_c \gtrsim 60$ the inertial force becomes part of the dominant force balance, and the flow transitions to the rotation-affected regime. Finally, from Figs. 4.3(a) and 4.3(b), we can estimate an upper limit for the LSV regime or, equivalently, the transition to RA convection, as the Ra/Ra_c value at which the inertial force becomes part of the dominant force balance or, similarly, the value at which Ro_ℓ becomes larger than one. We estimate that this occurs at $Ra/Ra_c \approx 400$. In Table 4.1 we present a summary of the dominant and subdominant force balances in all flow states.

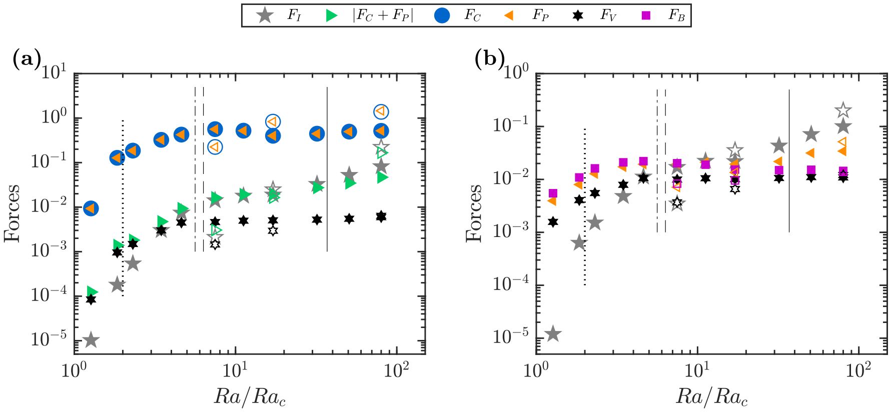

Figure 4.4.: *(a) Horizontal and (b) vertical force balance at mid-height as a function of the flow supercriticality Ra/Ra_c, for simulations at $Pr \approx 5$. Symbols and vertical lines are as in Fig. 4.3.*

To further illustrate how changes in the force balance affect the flow, we analyse the RMS values of the horizontal velocity u_{RMS} and vertical velocity w_{RMS} as a function of Ra/Ra_c. Here, $u_{\text{RMS}} = \sqrt{\langle u^2 \rangle + \langle v^2 \rangle}$ and $w_{\text{RMS}} = \sqrt{\langle w^2 \rangle}$ are also computed at mid-height ($\langle \cdot \rangle$ denotes time- and plane-averaging). At all heights, we have verified that $\langle u \rangle \approx \langle v \rangle \approx 0$, so that no mean horizontal flows are established across the periodic domain and that $\langle w \rangle \approx 0$ owing to the incompressibility constraint. Figure 4.5 shows that for cells and columns, at $Ra/Ra_c \lesssim 6$, the participation of buoyancy in the subdominant force balance yields large vertical velocity fluctuations. Conversely, the smaller contribution of inertial forces may be associated with low variability of horizontal velocities, which moreover can be attributed to the strong vertical alignment of the flow structures in this regime. In the plumes regime, where inertial forces are as

Flow	Dominant force balance	Subdominant force balance
Cells	$F_C = -F_P$	$F_{\text{ageos}} = F_V + F_B$
Columns	$F_C = -F_P$	$F_{\text{ageos}} = F_V + F_B$
Plumes	$F_C = -F_P$	$F_{\text{ageos}} = -F_I + F_V + F_B$
LSVs	$F_C = -F_P$	$F_{\text{ageos}} = -F_I$
RA convection	$F_I = -F_P$	$F_C = F_V + F_B$

Table 4.1.: *Dominant and subdominant force balances at mid-height ($z = 0.5$) for each flow regime. Here, $F_{\text{ageos}} \equiv |F_C + F_P|$ measures the ageostrophy of the flow, i.e. the deviation from geostrophic balance caused by the presence of the remaining forces.*

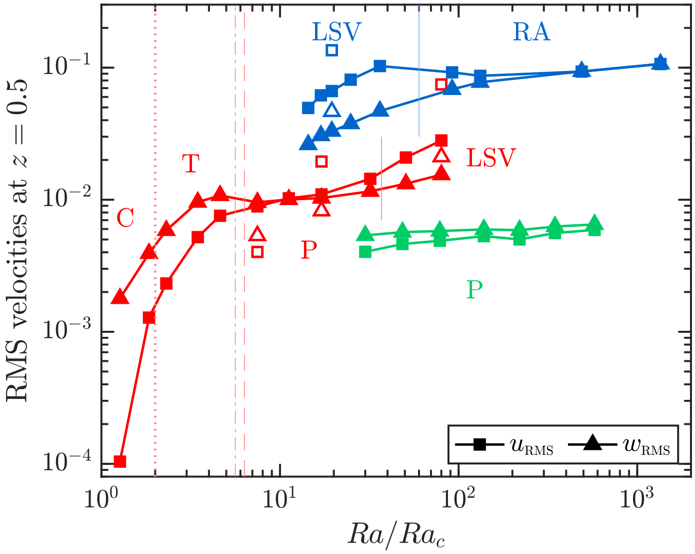

Figure 4.5.: *Root-mean-square (RMS) of horizontal and vertical velocities, u_{RMS} and w_{RMS}, respectively, at mid-height $z = 0.5$. Filled and open symbols correspond to simulations with no-slip and stress-free boundary conditions, respectively. Red, green and blue symbols are results from simulations at $Pr \approx 5$, 100 and 0.1, respectively. Colour-coded vertical lines and regime labels are as in Fig. 4.3.*

important as buoyancy, we see that the magnitude of horizontal velocity fluctuations is comparable to that of vertical fluctuations. Throughout the LSV regime at both $Pr \approx 5$ and 0.1, where the magnitude of inertial forces is even larger, horizontal velocity fluctuations are larger. As a consequence, the flow becomes largely dominated by a 2D (depth-independent) barotropic mode. In this nearly two-dimensional turbulent state, energy can be transferred from small to large scales, leading to the formation of LSVs (see Chapter 6). Finally, in the rotation-affected regime, seen at $Pr = 0.1$ and $Ra/Ra_c \gtrsim 60$, u_{RMS} shows little variation with Ra/Ra_c, whereas the loss of rotational constraint (i.e. the decreasing importance of the Coriolis force) allows for larger vertical velocity fluctuations. In fact, their magnitude becomes as large as the horizontal fluctuations. This suggests that the flow approaches a rather isotropic dynamics, such as the one for non-rotating convection.

We have thus identified and discussed the characteristic force balance of the observed flow regimes of RRBC. In particular, we have evaluated the RMS value of the governing forces at mid-height, and as such representative of the bulk. In the next section, we analyse the force balance close to the no-slip walls, and provide a comparison with the balance in the bulk.

4.4. Force balance near no-slip walls

In this section, we investigate the interplay between forces at a close distance from the no-slip walls. Specifically, we analyse the force balance at a distance δ_u from the bottom wall, where δ_u is the thickness of the kinetic boundary layer. The discrepancy between the force balances at this height and those at a distance δ_u from the top wall is better than 5%. To determine the thickness δ_u of this layer, we adopt the conventional definition that uses the location of the peak value in the vertical profile of the RMS horizontal velocity $u_{\mathrm{RMS}}(z)$ (the profiles are time- and plane-averaged; the profile of selected cases are shown in Fig. 5.2(b)). We then employ Eq. (4.6) to determine the magnitudes of the forces at this height. The results are shown in Figs. 4.6(a), 4.6(c) and 4.6(e) for simulations at $Pr \approx 5$, 100 and 0.1, respectively. These figures show that also near the walls the flow is primarily geostrophic in regimes displaying cells, columns, plumes and LSVs, whereas the rotational constraint is lost once it transitions to the rotation-affected regime. In particular, in Fig. 4.6(f), the transition from rotation-dominated ($Ro_\ell \lesssim 1$) to rotation-affected ($Ro_\ell \gtrsim 1$) convection occurs at approximately the same supercriticality as at mid-height, i.e. $Ra/Ra_c \approx 60$ (at $Pr = 0.1$; compare Figs. 4.3(f) and 4.6(f)). Therefore, with increasing supercriticality, the flow loses rotational constraint at roughly equal Ra/Ra_c at both considered heights.

Figures 4.6(a) and 4.6(c) shows that, overall, the near-wall magnitude of the forces in the subdominant balance of cells, columns, plumes and LSVs is considerably larger than in the bulk. For instance, $|F_C + F_P| \sim 10^{-2}$ in the bulk and 10^{-1} near the walls (compare, e.g., the green symbols in Figs. 4.3(a) and 4.6(a)). This indicates that the flow is more ageostrophic near the walls. In the cellular and columnar regimes, such ageostrophy is largely caused by viscous forces (see Fig. 4.6(a)). An analysis of the force balance per component, as the one employed in the bulk (discussed in Section 4.3), reveals that the buoyancy force is closely balanced by the vertical pressure-gradient force (also in the plumes and LSV regime). Thus, cells and columns also exhibits a VAC balance close to the walls, in fair agreement with asymptotic simulations. Nonetheless, as in the bulk, the inertial force is seen to steeply increase with Ra/Ra_c, in fact, more sharply and dominantly near the walls than in the bulk (compare the gray stars in Figs. 4.3(a) and 4.6(a)). Consequently, F_I is part of the subdominant force balance in the columnar regime. The effects of inertia persist in the subdominant balance of plumes and LSVs. Therefore, in these two regimes, similar to the bulk, the near-wall flow adopts a CIA balance, with some participation of viscous forces. Eventually, F_I takes over the dominant force balance that, along with the reduction of the Coriolis force, leads to the

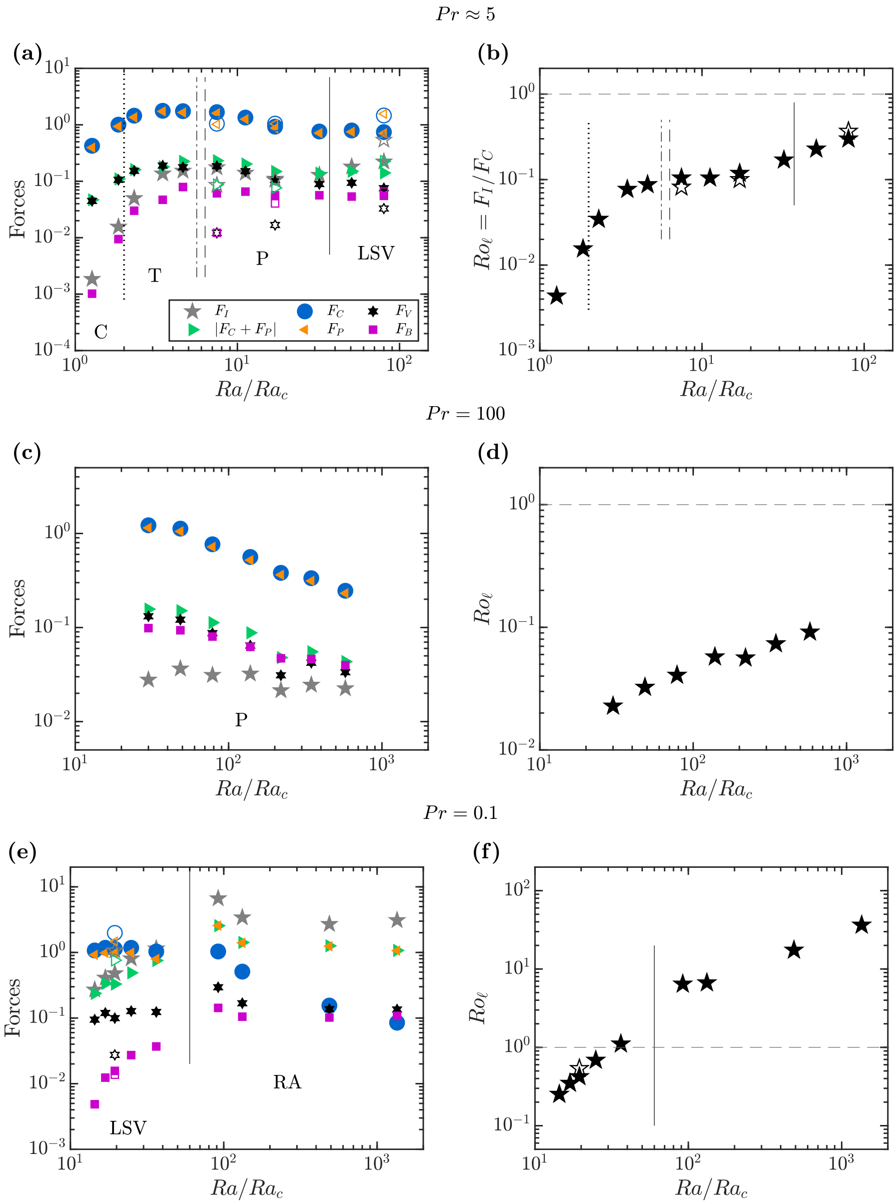

Figure 4.6.: Force balance (left column) and local Rossby number Ro_ℓ (right column), both at the kinetic boundary layer, as a function of Ra/Ra_c for simulations at (a,b) $Pr \approx 5$, (c,d) 100 and (e,f) 0.1. Filled and open symbols correspond to simulations with no-slip and stress-free boundary conditions, respectively. Vertical and horizontal lines, as well as regime labels, are as in Fig. 4.3.

transition to the rotation-affected regime. A summary of the dominant and subdominant force balances for all regimes is shown in Table 4.2.

The early influence of inertial forces near the walls can be associated with the presence of large horizontal velocity fluctuations u_{RMS} at the site of convergence (divergence) of fluid due to Ekman pumping (suction); compare the red squares in Figs. 4.5 and 4.7. That is, the vertical flux wA_{cross} in a column/plume of cross-sectional area $A_{\mathrm{cross}} = \pi R^2$ is fed by a boundary-layer flux uA_{cyl}

Flow	Dominant force balance	Subdominant force balance
Cells	$F_C = -F_P$	$F_{\mathrm{ageos}} = F_V$
Columns	$F_C = -F_P$	$F_{\mathrm{ageos}} = -F_I + F_V$
Plumes	$F_C = -F_P$	$F_{\mathrm{ageos}} = -F_I + F_V$
LSVs	$F_C = -F_P$	$F_{\mathrm{ageos}} = -F_I$
RA convection	$F_I = -F_P$	$F_C = F_V + F_B$

Table 4.2.: *Dominant and subdominant force balances at the kinetic boundary layer ($z = \delta_u$) for each flow regime. As in Table 4.1, $F_{\mathrm{ageos}} \equiv |F_C + F_P|$ measures the ageostrophy of the flow.*

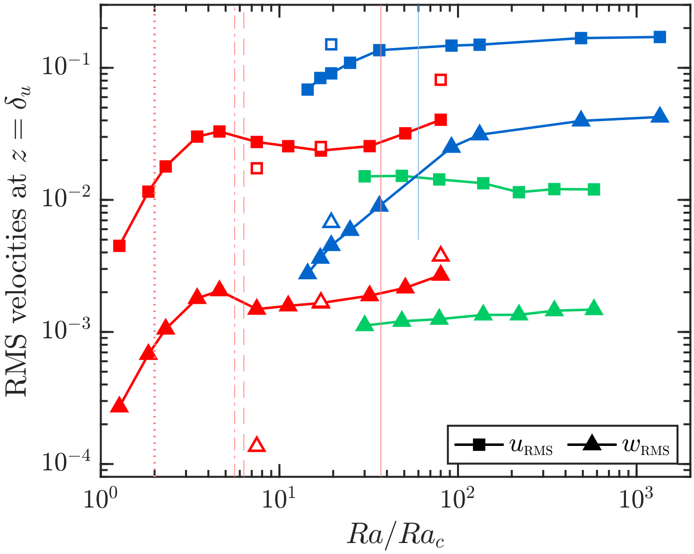

Figure 4.7.: *Root-mean-square (RMS) of horizontal and vertical velocities, u_{RMS} and w_{RMS}, respectively, at the kinetic boundary layer $z = \delta_u$. Filled and open symbols correspond to simulations with no-slip and stress-free boundary conditions, respectively. Red, green and blue symbols are results from simulations at $Pr \approx 5$, 100 and 0.1, respectively. Colour-coded vertical lines and regime labels are as in Fig. 4.3.*

through a cylindrical area $A_{\mathrm{cyl}} = 2\pi R\delta_u$, where R is the typical radius of the columns/plumes. Hence, the fluxes must be equal, i.e. $wA_{\mathrm{cross}} = uA_{\mathrm{cyl}}$, from which we get $w/u = 2\delta_u/R$. From Eqs. (2.21) and (2.41), $R \approx \ell_c/2 \sim Ek^{1/3}$ and $\delta_u \sim Ek^{1/2}$. Therefore, $w/u \sim Ek^{1/6} \ll 1$. Thus, based on the Ekman boundary layer theory [116] we expect that horizontal flow ($\sim u_{\mathrm{RMS}}$) near the wall (inside the Ekman layer) is much larger than vertical flow ($\sim w_{\mathrm{RMS}}$) emanating from the boundary layer. This is observed in Fig. 4.7. We note that also for stress free cases (open symbols in Fig. 4.7), u_{RMS} is larger than w_{RMS}. In this case, a near-wall flux is also expected to feed the columns/plumes, though no estimation on its scaling can be currently made due to the scarcity of stress-free cases. Finally, the presence of inertial forces in the near-wall subdominant force balance does not necessarily imply the loss of vertical coherence as it does in the bulk (which causes the regime transition between columns and plumes). Yet, at larger Ra/Ra_c, the loss of rotational constraint close to the walls, which happens at roughly the same Ra/Ra_c as in the bulk, does suggest a nearly complete relaxation of the Taylor–Proudman constraint. This has a great impact on the structure of the kinetic boundary layer. We discuss this topic in Chapter 5.

4.5. Conclusions

To summarise, we find that in rapidly rotating Rayleigh–Bénard convection the dominant force balance is geostrophy, the balance between the Coriolis force and the pressure-gradient force, as anticipated in previous literature [33,41,51,132]. The geostrophic regimes display cells, convective Taylor columns, plumes and large-scale vortices. Furthermore, we find that in these regimes the flow is also in leading geostrophic balance near the no-slip walls.

In simulations at $Pr = 0.1$, we find that the geostrophic balance breaks down at large supercriticality past the geostrophic regime. This results in the flow transition from the rotation-dominated state to rotation-affected convection. Specifically, the transition originates from the sudden decrease of the magnitude of the Coriolis force, along with an increment in the strength of inertial forces. Remarkably, we find that this loss of rotational constraint occurs synchronously (at about the same Ra/Ra_c) in the bulk and in the boundary-layer region.

The geostrophic flows are ageostrophic at higher order, caused by the contribution of the remaining forces (inertia, viscous and buoyancy forces). For cells and columns, ageostrophy is due to viscosity and buoyancy, thus leading to a VAC balance. Inertia is smaller, but steeply increases with Ra/Ra_c. For plumes, inertial forces enter the subdominant balance, along with viscous and buoyancy forces. For LSVs, inertia becomes the main source of ageostrophy. Plumes and LSVs can be considered in CIA balance, with some participation of viscous forces in the plumes regime. In rotation-affected convection, inertial and pressure-gradient forces constitute the dominant force balance; the subdominant balance is formed by the Coriolis, viscous and buoyancy forces.

In the bulk, the presence of inertial forces in the subdominant force balance marks the loss of vertical coherence of the columnar structures in the flow, and thus the commencement of the plumes regime. Near the no-slip boundaries, inertial effects become part of the subdominant force balance at smaller Ra/Ra_c within the columnar regime, although, remarkably, without deteriorating their structure. The reason is that, near the walls, this enhanced inertial force results from the convergence (and divergence) of fluid to the site of formation of vortical structures at the Ekman boundary layer.

In contrast with the bulk, the buoyancy force does not form part of the subdominant balance near the walls for cells, columns and plumes. This is despite having about the same order of magnitude ($\sim 10^{-2}$) at both locations. The reason is that viscous forces (for cells, columns and plumes) and inertial forces (for columns and plumes) are about one order of magnitude larger close to the boundaries, thus increasing the overall degree of ageostrophy of the flow by one order of magnitude in this region.

Chapter 5

Flow statistics

In this chapter, we investigate the flow and temperature structures that result from the dynamical balances presented in Chapter 4. The resulting thermal mixing in the fluid layer and the heat transfer are discussed in terms of the mean temperature profile and the RMS values of temperature as well as horizontal and vertical velocity. The near-wall profile of the RMS horizontal velocity is used to determine the thickness δ_u *of the kinetic boundary layer. We find that* $\delta_u \sim Ek^{1/2}$*, consistent with linear Ekman boundary layer theory, in the geostrophic regime. Deviations from this scaling are observed in the rotation-affected regime. There, the thermal boundary layer thickness* δ_θ *approaches the non-rotating scaling* $1/(2Nu)$*. Finally, we find that the distribution of temperature at the kinetic boundary layer depends on the relative thickness of the kinetic and thermal boundary layers.*

5.1. Introduction

In Chapter 4, we performed a thorough investigation on the interplay between the governing forces of rotating Rayleigh–Bénard convection. The results were used to characterise the observed flow regimes according to their specific force balance. In this chapter, we investigate the flow and temperature structures that result from these dynamical balances. For the task, we adopt a statistical approach. In Chapter 4, we already presented some of the results derived from statistical analysis of the flow. Namely, we utilised measurements of the RMS of horizontal and vertical velocity to illustrate the connections between the force balance and actual flow features in each regime. Here, we discuss how variations of the magnitude of horizontal and vertical velocity fluctuations relate to changes of the mean temperature profile across the fluid layer and the convective heat transfer Nu. In the literature special interest is given to these measurements. This is, on the one hand, due to their feasibility in laboratory experiments of rotating convection [71, 76] and, on the other hand, because they can be used to identify transitions between the flow regimes [41, 50, 71, 76].

For instance, the mean temperature profile, often characterised by its gradient $-d\langle T\rangle/dz$ at mid-height ($\langle\cdot\rangle$ indicates time- and plane-averaging), varies non-monotonically with Ra/Ra_c, giving it diagnostic properties of the various flow phenomenologies. Concretely, the mean temperature gradient decreases with Ra/Ra_c in the cellular and columnar regimes, it then increases in the plumes regime, and saturates in the geostrophic turbulence regime [41]. Beyond the latter regime, it has been observed that $-d\langle T\rangle/dz$ decreases again with Ra/Ra_c [76]. Eventually, it is expected that $-d\langle T\rangle/dz \approx 0$ at sufficiently large Ra/Ra_c, as the flow becomes insensitive to rotation and the bulk becomes nearly isothermal.

Close to the walls, the peak maxima in the vertical profiles of RMS temperature and horizontal velocity are often used to determine the thickness of the thermal boundary layer δ_θ and the kinetic boundary layer δ_u (see, e.g., [50]). The scaling of δ_u with Ek is fundamentally relevant to assess rotational control in the boundary layer. In linear Ekman boundary layer theory it is established that $\delta_u \sim Ek^{1/2}$ for geostrophic flows [107] (see Section 2.7). In this chapter, we evaluate whether the observed regimes of cells, columns, plumes and LSVs abide by this scaling. We certainly do not expect this for the kinetic boundary layer in the rotation-affected regime, as we found that the flow therein is not rotationally constrained (see Section 4.4); we shall verify this.

Detailed information on the spatial organisation of the flow and temperature structures can be obtained through characterisation of the probability distribution of the related physical quantities. This can be done by estimating their skewness and kurtosis. The skewness provides a measure of the asymmetry of the probability distribution. For instance, when the distribution of temperature is positively skewed, large above-average temperature fluctuations are preferred by the system, with smaller below-average values occupying a larger portion of the domain; the opposite is true for a negatively skewed distribution. The vertical profile of the skewness of vertical velocity (similar to temperature) is found to be antisymmetric about mid-height [31, 32, 155, 156]. For example, in Ref. [32], it is found that the fluid flow directed away from the walls is dominated by localised intense structures, so that the vertical velocity skewness is positive near the bottom and negative near the top wall. In this situation, the profile of vertical vorticity skewness is, on the other hand, symmetric about mid-height [31, 63, 157]: both the localised rising flows from the bottom and the localised sinking flows from the top display positive vertical vorticity. Finally, the kurtosis of the probability distribution of a certain quantity measures the feasibility of extreme values in the distribution, e.g. large values of kurtosis indicate that extreme fluctuations are very likely to occur.

In homogeneous isotropic turbulence, the distribution of velocity fluctuations is practically Gaussian, with kurtosis equal to 3 [158, 159], whereas the distribution of vorticity is strongly non-Gaussian, with kurtosis larger than 3 and increasing with the turbulence intensity [160]. The presence of localised coherent structures (plumes) in the flow raises the probability of extreme events, so that kurtosis larger than 3 is expected. Interestingly, in Ref. [41], low values of vertical velocity kurtosis at mid-height, close to 3, are also reported in the cellular regime, i.e. similar to the kurtosis value in turbulent flows. Whilst we do not doubt that this value does indeed characterise this nearly laminar regime, we would like to briefly discuss the underlying averaging process from which it derives. In [72, 132], temporal autocorrelations of temperature show that these vertically coherent structures remain nearly stagnant in time. The cellular regime is found to display slow modulations in time and space. This indicates that the assumption of a temporal and spatial ensemble average of independently fluctuating variables, often employed in the literature and in this thesis, merits careful use. To further illustrate this point, we refer the reader to Fig. 6 in Ref. [132], where the probability density functions of temperature time series for cells (panel a) and geostrophic turbulence (panel d) are shown. There, it can be seen that these distributions exhibit a similar Gaussian shape (their exact kurtosis values are quantified in Ref. [41]), even though the flows are markedly different.

The relevance of this study resides in the possibility to compare our numerical results with laboratory experiments of RRBC (although this task surpasses the scope of this thesis). This possibility stems from the fact that the statistical quantities studied in this chapter can be employed in laboratory experiments. For instance, the vertical profile of temperature can be determined using temperature measurements from a vertical arrangement of thermistors at the sidewalls of a rotating container [76] or inside the working fluid [161–164]. Other statistics based on the velocity field can be studied through particle image velocimetry (PIV) measurements [34, 38, 38, 64, 69, 72, 77, 165–167] or particle tracking velocimetry (PTV) [73].

Previous numerical and experimental studies on the statistical properties of the RRBC flow are presented, for example, in Refs. [41, 72, 132]. Both investigations in Refs. [41, 132] employ simulations of a set asymptotically reduced equations that are valid in the limit of rapid rotation ($Ek, Ro \to 0$) and stress-free boundary conditions. In Ref. [72], time-resolved PIV and three-dimensional PTV are employed. In Ref. [41], the mean temperature gradient, and RMS and kurtosis of various quantities are used to characterise the flow in the geostrophic regime of RRBC (cells, columns, plumes and large-scale vortices).

In Ref. [132], temporal and spatial auto-correlations and cross-correlations of several quantities are used to determine the temporal scales, horizontal length scales, velocity scales and transport properties of the flow in the aforementioned regime. In Ref. [72], experimental measurements of the vorticity field are used to compute spatial auto-correlations; their results are in good agreement with most of the observations reported in Ref. [132]. Nevertheless, some of the underlying aspects of flows under realistic conditions may not exhibit an asymptotic behaviour. For example, in the asymptotic limit of rapid rotation, a symmetric state is obtained where the skewness of the distributions of temperature, vertical velocity and vertical vorticity are zero over horizontal planes at all heights. As a result, there is a great degree of symmetry of the distribution of cyclonic and anticyclonic structures. However, a significant asymmetry of cyclonic and anticyclonic vortices in rotating flows has been reported in several laboratory experiments [168–171], numerical simulations [172–175] and studies of geophysical flows [176–179]. This asymmetry in natural flows may be linked to the finite character of the rotation rate to which they are subject [168–170, 172, 174]. Thus, for instance, a finite positive rotation rate would bias the skewness of vertical vorticity towards positive values. Here, we perform numerical simulations of the full Navier–Stokes equations subject to finite rotation rates. Another unavoidable aspect of flows in real life concerns their dynamics near bounding surfaces, where kinetic boundary layers form. These layers are absent in the asymptotic formulation, since stress-free conditions at the boundaries are explicitly considered. In our study, we consider the case of no-slip walls to mimic experimentally realisable boundary conditions. In Chapter 4, we found that the near-wall force balance is notably affected by the kinetic boundary layer. We thus anticipate that the flow structures and the statistical properties of the flow are also modified in this region.

The remainder of this chapter is structured as follows. In Section 5.2, we investigate the mid-height mean temperature gradient and the heat transport across the fluid layer, and in the subsequent Section 5.3, we discuss the (scaling) characteristics of the thermal and kinetic boundary layer thicknesses. In Section 5.4 we gain insight into the flow and temperature structures by means of the temperature, vertical velocity and vertical vorticity skewness. We further characterise the flow and thermal features by evaluating the likelihood of extreme values of the relevant physical quantities in Section 5.5. Lastly, in Section 5.6, we present our conclusions.

5.2. Mean temperature and heat transport

A known feature of rotating Rayleigh–Bénard convection is the gradual decrease of the mean temperature with height across the fluid layer, from a large value at the hot bottom wall to a lower temperature at the top [31, 76, 157, 180]. We illustrate this in Fig. 5.1(a), where we plot the vertical profile of time- and plane-averaged temperature for selected cases at $Pr \approx 5$ (notice the slight lack of antisymmetry of the red curve at $Ra/Ra_c = 3.5$, we shall discuss this in Section 5.4). This vertical variation of the mean temperature is often used to characterise the flow and to distinguish the different regimes, specifically, employing the mean temperature gradient $-d\langle T\rangle/dz$ measured at mid-height $z = 0.5$ [41, 45, 50, 76]. As a function of Ra/Ra_c, this quantity can be evaluated in two limit cases. At $Ra/Ra_c < 1$, where no convection is present, the heat transfer from the bottom wall to the top wall is carried out by conduction alone. In this state the temperature profile is linear and the temperature gradient is maximal, $-d\langle T\rangle/dz = 1$. In the limit of very large Ra/Ra_c, the influence of rotation is minimal, and the flow approaches a non-rotating style of convection. In this state the bulk is well mixed and thus its temperature is uniform, therefore $-d\langle T\rangle/dz \to 0$ (in the bulk outside the boundary layers). For values of Ra/Ra_c between these two extreme cases, the temperature gradient exhibits variations that are specific to the distinct flow regimes, and thus provide a way to characterise them.

In Fig. 5.1(b), we plot the mean temperature gradient $-d\langle T\rangle/dz$ at $z = 0.5$ as a function of Ra/Ra_c for all Prandtl numbers explored. At $Pr \approx 5$, we observe that the temperature gradient decreases with Ra/Ra_c throughout the cellular and columnar regimes. This can be explained as follows. At the lowest Ra/Ra_c, rotation heavily suppresses vertical velocity fluctuations w_{RMS} (see Fig. 5.1(c)). As a result, the vertical convective mixing in the fluid layer is greatly inhibited; the temperature fluctuations $T_{\mathrm{RMS}} = \sqrt{\langle (T - \langle T\rangle)^2\rangle}$ at mid-height (Fig. 5.1(d)) also attain their smallest value. Hence, the temperature gradient is largest at this Ra/Ra_c. Moreover, the vertical transport of heat across the fluid layer, estimated as the mean of all convective Nusselt numbers described in Section 3.5, is lowest (see Fig. 5.1(e)). With increasing supercriticality, vertical convection is augmented (w_{RMS} and T_{RMS} increase) and thus $-d\langle T\rangle/dz$ decreases. It is worth noting that cells and columns interact weakly with each other [89, 181], and thus provide little to no horizontal mixing. The decrease of $-d\langle T\rangle/dz$ in the cellular and columnar regimes agrees within 3.6% with the asymptotic scaling $d\langle T\rangle/dz \sim (RaEk^{4/3})^{0.96}$ in Ref. [41] (see dotted line in Fig. 5.1(b)). This drop in temperature gradient is moreover accompanied by an increment in heat transport. For the four cases at $Pr \approx 5$ and lowest

Ra/Ra_c in Fig. 5.1(e), a scaling $Nu \sim (Ra/Ra_c)^{2.7}$ fits the data with an RMS error of about 4.8% (not shown). This scaling agrees reasonably well with the scaling $Nu \sim (RaEk^{4/3})^2 \sim (Ra/Ra_c)^2$ reported in Ref. [41] (see dotted line in Fig. 5.1(e)). Note that these changes in $-d\langle T\rangle/dz$, w_{RMS}, T_{RMS} and Nu are very steep. This can be attributed to the strong vertical alignment of cells and columns, which enables them to efficiently transport warmer (cooler) fluid close to the bottom (top) across the fluid layer (see Figs. 4.2(a) and 4.2(b)).

At larger Ra/Ra_c, in the plumes regime, conversely, the temperature gradient is seen to increase with Ra/Ra_c (also observed for plumes at $Pr = 100$). In this regime, w_{RMS} varies marginally, whereas the horizontal mixing is enhanced (u_{RMS} gradually increases) due to the ever stronger interaction amongst plumes. In other words, horizontal mixing is fostered over vertical mixing. Therefore, due to the limited vertical mixing, the magnitude of temperature fluctuations gradually decreases with Ra/Ra_c (see Fig. 5.1(d)), whilst the temperature gradient increases (Fig. 5.1(b)). The interaction between the plumes reduces the efficiency of the transport of fluid, with high thermal contrast, across the fluid layer. As a consequence the increase of Nu with Ra/Ra_c is shallower. A least-squares fit of the Nusselt number for plumes at $Pr \approx 5$ (i.e. for $6 \leq Ra/Ra_c \leq 37$ in Fig. 5.1(e)) yields a scaling $Nu \sim (Ra/Ra_c)^{0.4}$ (RMS error of 2.3%), a reduction of about 85% in the scaling exponent respect to the cellular and columnar regimes. For plumes at $Pr = 100$, the scaling is $Nu \sim (Ra/Ra_c)^{0.2}$ within 4.3%.

In the regime of large-scale vortices at $Ra/Ra_c > 37$ (at $Pr \approx 5$), the temperature gradient gradually reverses back to a downwards trend. In this regime, vertical velocity fluctuations, again, increase with supercriticality, thus enhancing vertical mixing (though T_{RMS} shows little variation with Ra/Ra_c at this Pr). Regarding the scaling of Nu with Ra/Ra_c, it is not clear from our explored parameter cases whether or not this is affected in the transition from plumes to LSVs. However, we do anticipate a slightly steeper scaling in the LSV regime, in accordance with the moderate increase of w_{RMS} with Ra/Ra_c. To evaluate this potential change in the Nu scaling, we consider the scaling law in Ref. [36]: $Nu_* = aRa_*^b$, where $Nu_* = NuEk/Pr$ and $Ra_* = RaEk^3Nu/Pr^2$, with best-fit parameters $a = 0.17$ and $b = 0.55$. Here, a is adjusted to account for the different definitions of Ek used in Ref. [36] and in this thesis. This scaling law is independent of the diffusive properties (thermal diffusivity κ and kinematic viscosity ν) of the fluid. Whilst the presence of LSVs in the simulations in Ref. [36] is not mentioned, this scaling is proposed for a rotation-dominated flow, at $Pr = 0.7$ and 7, subject to competing non-linear effects, in presence of stress-free walls. In Ref. [44], $Nu_* = 0.17Ra_*^{0.55}$ is shown to

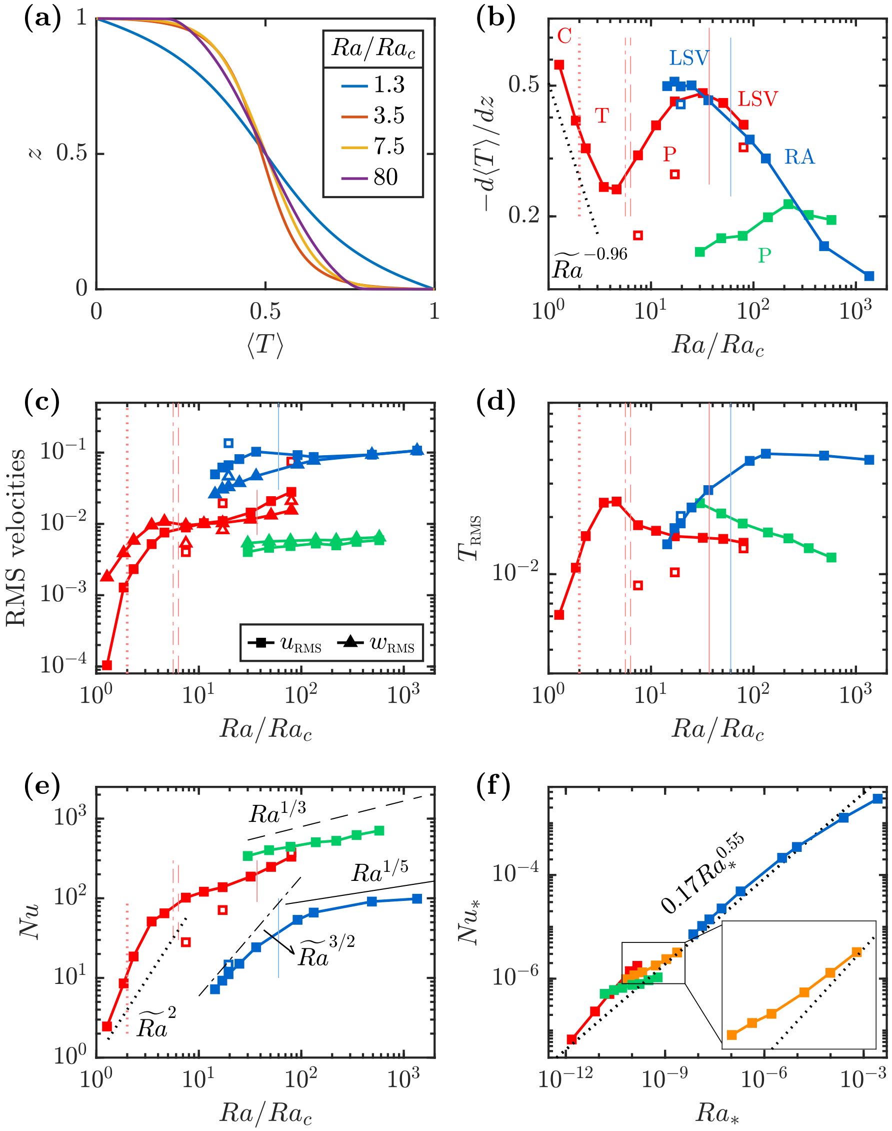

Figure 5.1.: *(a) Vertical profiles of plane-averaged temperature for selected cases at $Pr \approx 5$ (visualised in Figs. 4.2(a) to 4.2(d)). (b) Mean temperature gradient at mid-height $z = 0.5$; the black dotted line is the asymptotic scaling in both cellular and columnar regimes [41]. (c) RMS horizontal and vertical velocity, u_{RMS} and w_{RMS}, at mid-height (same plot as in Fig. 4.5). (d) Mid-height RMS temperature. (e) Convective Nusselt number Nu; black dotted and dash-dotted lines are asymptotic scalings in the cellular/columnar and LSV regimes, respectively; black dashed and solid lines are predicted scalings for non-rotating RBC at $Pr \approx 5$ [115, 182, 183] and 0.1 [115, 182–184], respectively. Red, green and blue symbols are cases at $Pr \approx 5$, 100 and 0.1, respectively. Colour-coded vertical lines and regime labels are as in Fig. 4.3. (f) Nu_* versus Ra_*; cases at $Pr = 5.5$ are shown in red and at $Pr = 5.2$ in orange. The dotted line is the scaling $Nu_* = 0.17Ra_*^{0.55}$ as proposed in Ref. [36]. The inset is a close-up for $Pr = 5.2$ cases for $5\times10^{-11} \le Ra_* \le 4\times10^{-9}$ and $8\times10^{-7} \le Nu_* \le 5\times10^{-6}$. In all panels, filled and open symbols are for no-slip and stress-free simulations, respectively.*

fit fairly well Nu measurements of LSV cases at $Pr = 1$, also for stress-free boundary conditions. In Fig. 5.1(f) we plot Nu_* as a function of Ra_* for all our simulation cases. In the close-up of the $Pr \approx 5$ data, shown in the inset, we notice that the data appear to approach the proposed scaling. In the LSV regime at $Pr = 0.1$ (for $Ra/Ra_c < 60$), the mid-height temperature gradient displays little variation with Ra/Ra_c for the four cases with lowest supercriticality, yet $-d\langle T\rangle/dz$ is smaller for the fifth case at $Ra/Ra_c \approx 36$, suggesting that $-d\langle T\rangle/dz$ decreases with Ra/Ra_c also at this Prandtl number. The Nusselt number scaling is quite steep (see blue symbols at $Ra/Ra_c < 60$ in Fig. 5.1(e)), which may be associated with the clear increase of both vertical velocity fluctuations and temperature fluctuations (see Figs. 5.1(c) and 5.1(d), respectively). This scaling is in fairly good agreement (RMS error of 5.8%) with the asymptotic scaling $Nu \sim (RaEk^{4/3})^{3/2} \sim (Ra/Ra_c)^{3/2}$ for the geostrophic turbulence regime reported in Ref. [41] (see dash-dotted line in Fig. 5.1(e)). Similar to the Nu_* versus Ra_* scaling in Ref. [36], this scaling is independent of κ and ν. We also evaluate the scaling behaviour of our $Pr = 0.1$ data in the LSV regime in terms of Nu_* in Fig. 5.1(f). We find that the $Ra_*^{0.55}$ scaling fits these Nu data with an approximate RMS error of 2.7%. Finally, in the rotation-affected regime at $Ra/Ra_c > 60$ (at $Pr = 0.1$), $-\partial T/\partial z$ continues to decrease with Ra/Ra_c as the influence of rotation weakens and the bulk becomes more isothermal. In this regime, the heat transport scaling is shallower than for LSVs, as it approaches the scaling $Ra^{1/5}$ for non-rotating Rayleigh–Bénard convection (at $Pr = 0.1$; black solid line in Fig. 5.1(e)) predicted in Refs. [115,182,183]. At $Pr \approx 5$, the predicted scaling is $Ra^{1/3}$ (black dashed line) [115,182–184].

5.3. Boundary layers

In this section, we investigate the vertical profiles of RMS temperature $T_{\mathrm{RMS}}(z)$ and horizontal velocity $u_{\mathrm{RMS}}(z)$ in the region close to the no-slip walls. In Fig. 5.2 we present these profiles for the lower half of the domain for selected cases at $Pr \approx 5$; other cases at different Ra/Ra_c and Pr display profiles that are qualitatively similar to the ones shown in this figure. In the vertical profile of T_{RMS}, in Fig. 5.2(a), we see that temperature fluctuations are zero at the bottom wall (also at the top wall, not shown). There, the temperature field must meet the constant-temperature boundary condition $T = 1$ at $z = 0$ (for the top wall $T = 0$ at $z = 1$). Away from the wall, but still at a short distance from it, T_{RMS} increases rapidly. In fact, T_{RMS} attains its maximum values in this region. The location of the peak value in the vertical profile is often used

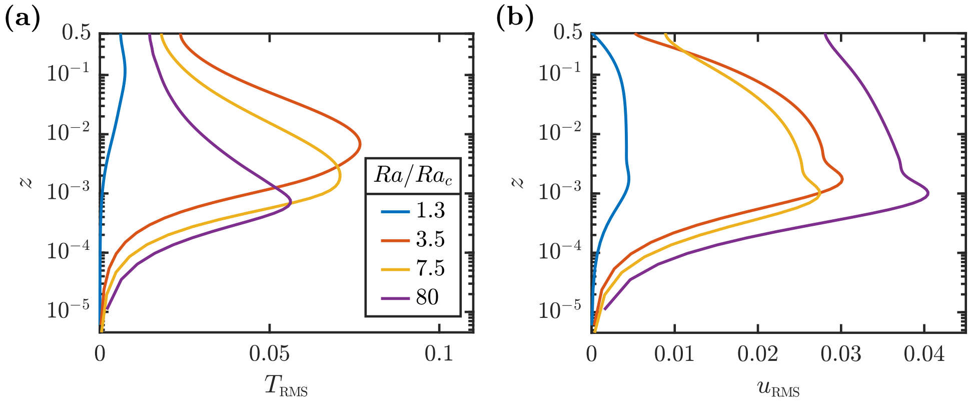

Figure 5.2.: *RMS vertical profiles of (a) temperature and (b) horizontal velocity for selected cases at $Pr \approx 5$ (same as those shown in Fig. 5.1(a)). Other cases at different Ra/Ra_c and Pr exhibit profiles that are qualitatively similar to the ones shown here. The profiles, which are symmetric about $z = 0.5$, are shown for the lower half of the domain. The vertical axes have been made logarithmic to highlight the boundary layer structure.*

as a measure of the thickness δ_θ of the thermal boundary layer. For the case with the lowest supercriticality, at $Ra/Ra_c = 1.3$ (blue curve in Fig. 5.2(a)), the signature of the thermal layer is weaker compared to the other cases, which reflects the near-laminar state of the flow at such a low supercriticality. In the vertical profile of u_{RMS}, in Fig. 5.2(b), we observe that large values of RMS horizontal velocity are also found near the walls. Just like for T_{RMS}, the u_{RMS} maxima are frequently used to define the thickness δ_u of the kinetic boundary layer [41, 50].

Figure 5.3(a) presents the plots of the thermal and kinetic boundary layer thicknesses, δ_θ and δ_u, as a function of Ra/Ra_c for all our simulations at all Prandtl numbers. Starting from δ_θ at $Pr \approx 5$, we see that the thermal layer is thickest at the lowest supercriticality and that it decreases with Ra/Ra_c. This decrease is quite steep for low values of Ra/Ra_c, and gradually becomes shallower towards larger supercriticalities. The kinetic boundary layer thickness δ_u, on the other hand, remains constant for our two sets of simulations at $Pr \approx 5$ and fixed Ek: $\delta_u \approx 1.7 \times 10^{-3}$ for cases at $Ek = 3 \times 10^{-7}$ (red triangles) and $\delta_u \approx 10^{-3}$ for those at $Ek = 10^{-7}$ (orange triangles). For cells and columns, the thermal boundary layer is thicker than the kinetic layer. This is also observed in the plumes regime, although, in contrast, plumes at $Pr = 100$ exhibit a thicker kinetic boundary layer. A similar situation occurs in the LSV regime: $\delta_u > \delta_\theta$ at $Pr \approx 5$, whereas $\delta_\theta > \delta_u$ for LSVs at $Pr = 0.1$. This all suggests that the bulk flow state does not significantly depend on

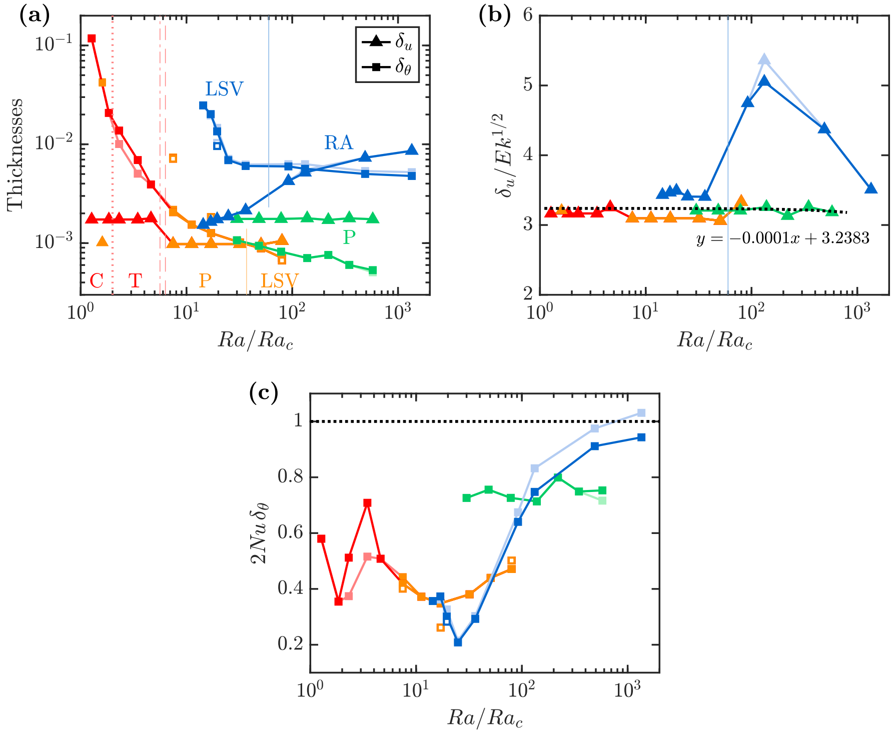

Figure 5.3.: *(a) Kinetic and thermal boundary layer thicknesses, δ_u and δ_θ, near the bottom wall (dark-coloured symbols) and the top wall (light-coloured symbols), as a function of Ra/Ra_c. Filled and open symbols are for no-slip and stress-free simulations, respectively. Red, orange, green and blue symbols are cases at $Pr = 5.5$ (at $Ek = 3 \times 10^{-7}$), 5.2 (at $Ek = 10^{-7}$), 100 (at $Ek = 3 \times 10^{-7}$), and 0.1 (at fixed $Ra = 10^{10}$ and varying Ek), respectively. Colour-coded vertical lines and regime labels are as in Fig. 4.3. (b) Kinetic boundary layer thickness scaled by $Ek^{1/2}$, the theoretical scaling for linear Ekman boundary layers [107]. The dotted line is a linear fit for values of $\delta_u/Ek^{1/2}$ below 3.5 (i.e. the four cases at $Pr = 0.1$ with largest Ra/Ra_c are excluded). A case at $Pr = 5.2$ and $Ra/Ra_c = 1.6$ is included in Figs. 5.3(a) and 5.3(b) to demonstrate the overlap between simulations at $Pr = 5.2$ and 5.5. (c) Thermal boundary layer thickness multiplied by two times the convective Nusselt number Nu. This quantity is equal to one for non-rotating convection (see Eq. (2.26)).*

the relative thickness of the boundary layers. In the LSV regime at $Pr = 0.1$, the thickness of the thermal layer steeply decreases with Ra/Ra_c, whereas it becomes much shallower, quite quickly, towards the rotation-affected regime. On the other hand, the kinetic boundary layer thickness increases with Ra/Ra_c in the regimes of LSV and rotation-affected convection. This is because in our set of simulations at $Pr = 0.1$, Ek is varied, whilst Ra is kept fixed. Specifically, δ_u is predicted to scale as $Ek^{1/2}$ in linear Ekman boundary layer theory [107] for rotationally constrained flows (see Eq. (2.41)). To evaluate this scaling, in Fig. 5.3(b) we plot $\delta_u/Ek^{1/2}$ as a function of the supercriticality of the flow. The figure reveals that all cases in the geostrophic regime (cells, columns, plumes and LSVs; at all Prandtl numbers) comply with the $Ek^{1/2}$ scaling with an RMS error just under 4%. Even the prefactor, approximately equal to 3.24 (see linear fit in Fig. 5.3(b)), is only weakly dependent on Pr. However, in the rotation-affected regime (at $Pr = 0.1$), where the kinetic boundary layer is no longer rotationally constrained (discussed in Section 4.4), this layer does not exhibit the theoretical scaling $Ek^{1/2}$. Therefore, the kinetic boundary layer at Ra/Ra_c values beyond the geostrophic regime is certainly not of Ekman type. The thermal boundary layer is also affected by the loss of rotational constraint. Namely, in non-rotating convection, δ_θ relates to the convective Nusselt number Nu through the expression $\delta_\theta = 1/(2Nu)$ (see Eq. (2.26), recall that δ_θ is already normalised by H). In Fig. 5.3(c), we plot the quantity $2Nu\,\delta_\theta$ for all simulation cases. We observe that rotationally dominated regimes are poorly described by $2Nu\,\delta_\theta = 1$, whereas cases at $Pr = 0.1$ in the rotation-affected regime tend towards this theoretical prediction as Ra/Ra_c increases. Similar results are reported in Ref. [42] for rotationally constrained regime at $RaEk^{3/2} < 10$, or $Ra/Ra_c \lesssim 124$ (at $Pr = 0.1$ and $Ra = 10^{10}$), and weakly rotating convection at $RaEk^{3/2} > 10$, or $Ra/Ra_c \gtrsim 124$.

5.4. Temperature, velocity and vorticity skewnesses

To gain insight into the temperature and velocity structures in the flow, we evaluate the third-order moment, or skewness, of these quantities. In Section 5.1, we explained that positive values of the temperature skewness $T_{\text{SKEW}} = \langle (T - \langle T \rangle)^3 \rangle / T^3_{\text{RMS}}$ indicate that large above-average temperature fluctuations are localised in small portions of the domain, whereas smaller below-average values are distributed over a larger portion of the domain; and vice versa for a negatively skewed distribution. This is also valid for the skewness of vertical velocity $w_{\text{SKEW}} = \langle w^3 \rangle / w^3_{\text{RMS}}$ and of vertical vorticity $\omega_{z,\text{SKEW}} = \langle \omega_z^3 \rangle / \omega^3_{z,\text{RMS}}$. As before, $\langle \cdot \rangle$ indicates averaging over time and over horizontal planes at a given height. Figure 5.4 shows the vertical profiles of skewness for selected cases at $Pr \approx 5$. For most cases, including those at different Ra/Ra_c and Pr not shown in Figs. 5.4(a), 5.4(c) and 5.4(e), the vertical profiles of T_{SKEW} and w_{SKEW} are antisymmetric about mid-height, whereas the profiles of $\omega_{z,\text{SKEW}}$ are symmetric. As discussed in Section 5.1, this is certainly expected, as it is consistent, for instance, with the presence of localised hot rising cyclonic flows in the lower half of the domain and localised cold sinking cyclonic flows in the upper

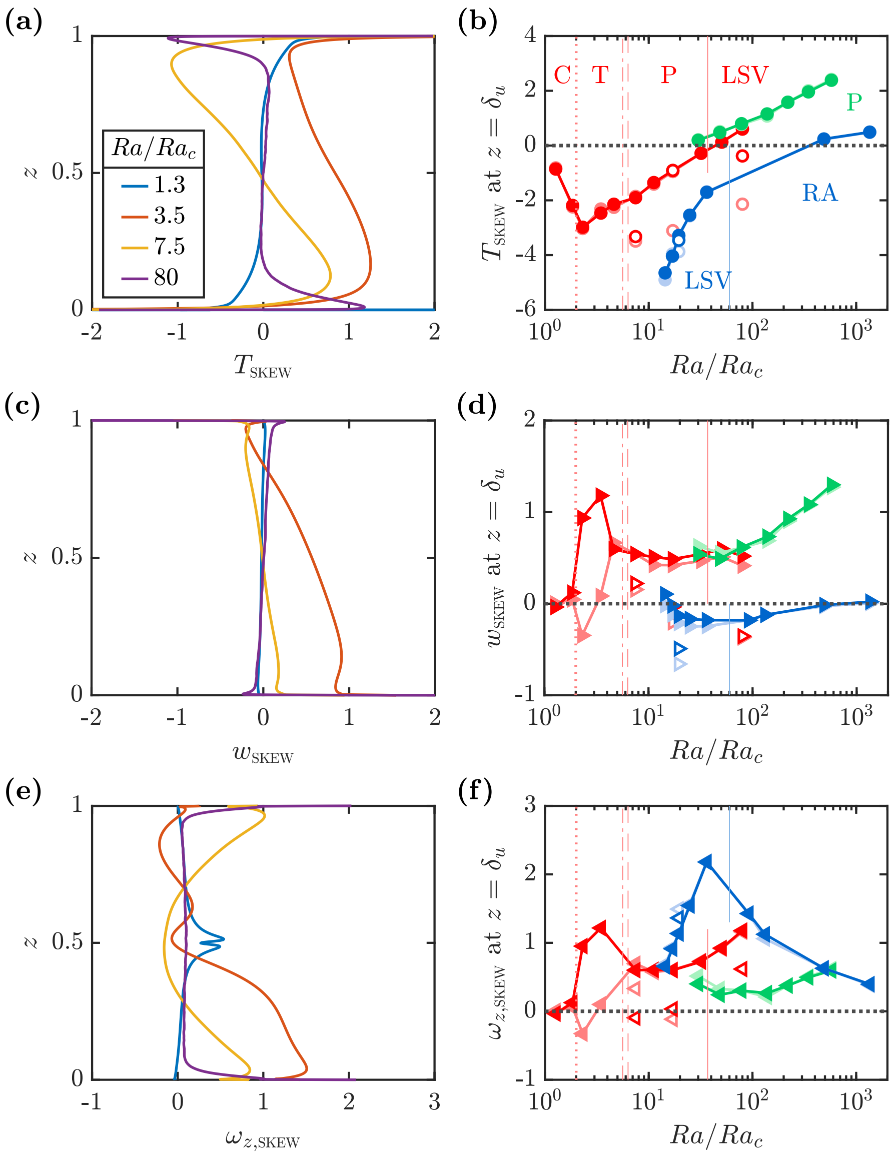

Figure 5.4.: *Vertical profiles of skewness of (a) temperature, (c) vertical velocity and (e) vertical vorticity, for selected cases at $Pr \approx 5$. (b) Temperature, (d) vertical-velocity and (f) vertical-vorticity skewness at the bottom kinetic boundary layer ($z = \delta_u$; dark-coloured symbols). Also in (b), (d) and (f), we plot the values of T_{SKEW}, w_{SKEW} and $\omega_{z,SKEW}$ (where T_{SKEW} and w_{SKEW} are multiplied by minus one) at the top kinetic boundary layer ($z = 1 - \delta_u$; light-coloured symbols), respectively. Filled and open symbols are for no-slip and stress-free simulations, respectively. Red, green and blue symbols are cases at $Pr \approx 5$, 100 and 0.1, respectively. Colour-coded vertical lines and regime labels are as in Fig. 4.3.*

half [50, 63, 89, 157] (see, e.g., the thermal plumes at $Pr \approx 5$ and $Ra/Ra_c = 7.5$ in Fig. 4.2(c)). However, we notice that the vertical profiles of T_{SKEW} and w_{SKEW} at $Pr \approx 5$ and $Ra/Ra_c = 3.5$ are clearly not antisymmetric, and the profile of $\omega_{z,\text{SKEW}}$ is not symmetric. Visualisation of the temperature fluctuations in Fig. 4.2(b) reveal that in this case the flow is dominated by localised hot rapidly rising convective columns surrounded by cool slowly sinking fluid. A similar situation is found for the case at $Pr \approx 5$ and $Ra/Ra_c = 2.3$ (not shown). A possible reason for this asymmetry in the number of hot and cold columns may be that this arrangement emerges during the early development of the columnar structures, and it then persists over time due to the strong stability of the flow at low supercriticality. The net effect is that skewness curves in Figs. 5.4(a) and 5.4(c) are shifted towards positive values, whilst they should be zero at $z = 0.5$, and ω_{SKEW} should be vertically symmetric (Fig. 5.4(e)). We expect that this asymmetric arrangement will equilibrate into the expected distribution with equal number of hot and cold columns at sufficiently long simulation times, of the order of the viscous diffusion time scale $\tau_\nu = \sqrt{Ra/Pr}\tau_{\text{ff}}$, or $\sim 10^4$ convective time units (at $Ra \sim 10^{10}$ and $Pr \approx 5$). We must acknowledge, however, that the question why this is not observed in other cases in the columnar regime, or even for cells and plumes, warrants further investigation.

For most cases, the largest values of T_{SKEW}, w_{SKEW} and $\omega_{z,\text{SKEW}}$ are found near the walls. This reveals a strong asymmetry in the statistical distribution of temperature, vertical velocity and vertical vorticity in this region. In Figs. 5.4(b), 5.4(d) and 5.4(f), we plot the values of skewness at the bottom kinetic boundary layer ($z = \delta_u$; dark-coloured symbols) and at the top kinetic boundary layer ($z = 1 - \delta_u$; light-coloured symbols), as a function of Ra/Ra_c. The values of T_{SKEW} and w_{SKEW} at $z = 1 - \delta_u$ are plotted with a minus sign to be able to compare their magnitude to that at $z = \delta_u$. Notice the excellent agreement of the skewness values at these two heights for most of our simulation cases, barring those at $Ra/Ra_c = 2.3$ and 3.5, both at $Pr \approx 5$ (here, the discrepancy results from the asymmetry of hot and cold columns in these two cases, discussed above). In these two cases, the values of $-w_{\text{SKEW}}$ and $\omega_{z,\text{SKEW}}$ (notice the minus sign in w_{SKEW}; as plotted in Figs. 5.4(d) and 5.4(f)) at the top kinetic boundary layer are expected to shift towards positive values, as a state of equal number of hot and cold columns is achieved at longer simulation times. In such a case, the vertically antisymmetric profile of T_{SKEW} and w_{SKEW}, and vertically symmetric profile of $\omega_{z,\text{SKEW}}$, about mid-height would be recovered for these cases. Bearing in mind these expected symmetries and asymmetries, let us then use measurements taken at the bottom kinetic boundary layer as a starting point for our discussions. At $Pr \approx 5$, w_{SKEW} and $\omega_{z,\text{SKEW}}$ are positive for all flow regimes (cells, convective Taylor columns, plumes and LSVs), which reveals the presence of localised flows with cyclonic vorticity emanating from the boundary layer (e.g., see visualisations in Figs. 5.5(b) and 5.5(c)). On the other hand, $T_{\text{SKEW}} < 0$ for cells, columns and plumes. Interestingly, in Section 5.3 we observed that in these cases the kinetic boundary layer is embedded within the thermal boundary layer (i.e. $\delta_u < \delta_\theta$ in Fig. 5.3(a)). This indicates that localised flow structures within the thermal boundary layer do not lead to localisation of hot fluid in this region. Instead, fluid with above-average temperature in the thermal boundary layer interior is distributed over large portions of the horizontal domain (large red patches in Fig. 5.5(a)). This can be attributed to fluid parcels with below-average temperature that penetrate into the thermal boundary layer, and that are concentrated in smaller regions (the area occupied by the blue patches in Fig. 5.5(a) is about 1.7 times smaller than for red patches). In the LSV regime (at $Pr \approx 5$), where the kinetic boundary layer becomes thicker than the thermal boundary layer, T_{SKEW} becomes positive. Thus, hot fluid is now localised at $z = \delta_u$ (e.g., in Fig. 5.5(d), it occupies 45% of the total cross-sectional area), which can be associated with the localisation of positive vertical velocity and cyclonic vorticity at this height (Figs. 5.5(e) and 5.5(f)). Similarly, for plumes at $Pr = 100$, we find that the statistical distribution of temperature is positively skewed ($T_{\text{SKEW}} > 0$), where $w_{\text{SKEW}}, \omega_{z,\text{SKEW}} > 0$ and $\delta_u > \delta_\theta$. At $Pr = 0.1$, it is also seen that cases in which $\delta_\theta > \delta_u$, the temperature skewness is negative (e.g., in Fig. 5.5(g), hot fluid within the thermal layer is distributed over 68% of the cross-sectional area, whereas the cold fluid occupies the remaining 32%). Just like for cells, columns and plumes at $Pr \approx 5$, where the same is observed, $\omega_{z,\text{SKEW}}$ is positive (see, e.g., the localised cyclonic vortices in Fig. 5.5(i)); here the vertical-velocity skewness is very small. This again highlights the idea that localisation of upward flows and/or vertical vorticity in the interior of the thermal boundary layer does not lead to localised parcels of fluid with positive thermal contrast in this region. Finally, the two cases at $Pr = 0.1$ with largest Ra/Ra_c exhibit $T_{\text{SKEW}} > 0$ and $\delta_u > \delta_\theta$ in agreement with the description discussed.

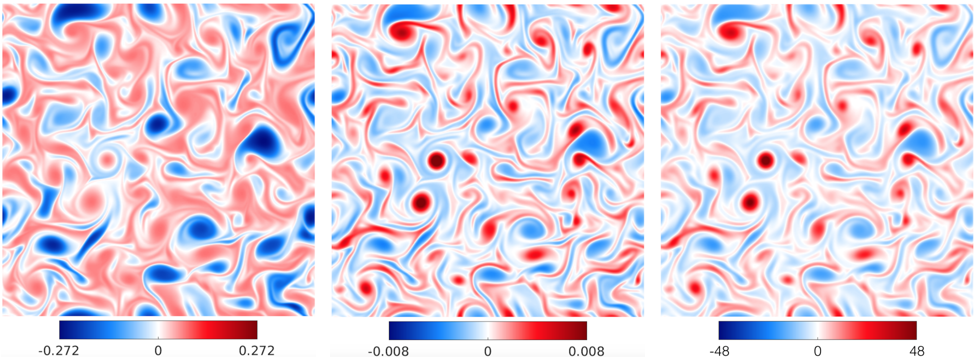

(a) $T - \langle T \rangle$ **(b)** w **(c)** ω_z

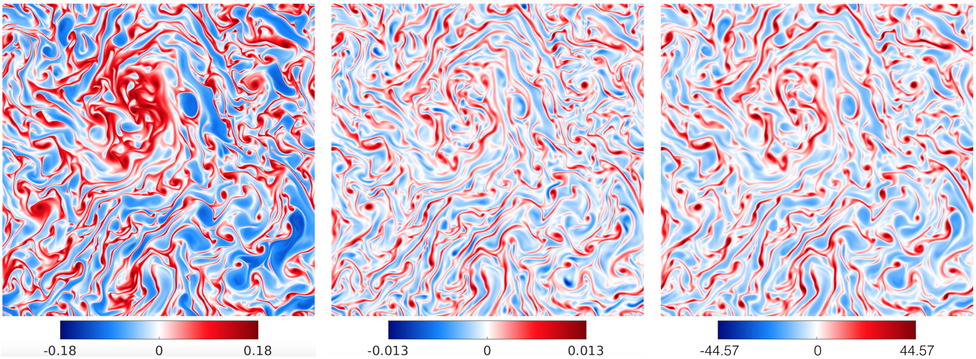

(d) $T - \langle T \rangle$ **(e)** w **(f)** ω_z

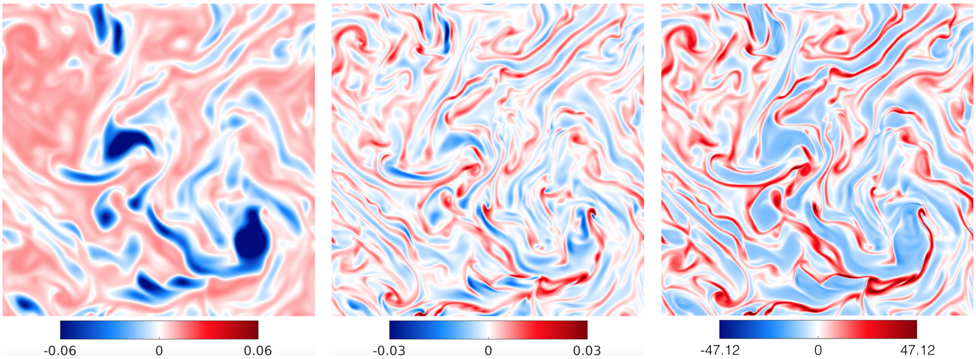

(g) $T - \langle T \rangle$ **(h)** w **(i)** ω_z

Figure 5.5.: *Snapshot of (a,d,g) temperature fluctuations, (b,e,h) vertical velocity, and (c,f,i) vertical vorticity, at the kinetic boundary layer edge ($z = \delta_u$) for cases (a-c) at $Pr \approx 5$ and $Ra/Ra_c = 7.5$ (visualised in Fig. 4.2(c)), (d-f) at $Pr \approx 5$ and $Ra/Ra_c = 80$ (in Fig. 4.2(d)), and (g-i) at $Pr = 0.1$ and $Ra/Ra_c = 20$ (in Fig. 4.2(g)).*

5.5. Temperature, velocity and vorticity kurtoses

Further understanding of the flow and temperature structures can be gained by computing the kurtosis of relevant physical quantities. The kurtosis of the temperature distribution is $T_{\mathrm{KURT}} = \langle (T - \langle T \rangle)^4 \rangle / T^4_{\mathrm{RMS}}$, for vertical velocity is $w_{\mathrm{KURT}} = \langle w^4 \rangle / w^4_{\mathrm{RMS}}$ and for vertical vorticity is $\omega_{z,\mathrm{KURT}} = \langle \omega_z^4 \rangle / \omega^4_{z,\mathrm{RMS}}$. We present the kurtosis profiles in Fig. 5.6 for selected cases at $Pr \approx 5$. As it was observed for the skewness, the kurtosis profiles of the case at $Ra/Ra_c = 3.5$ (also at $R = 2.3$, not shown) display asymmetries about mid-height, albeit less evident than for skewness thanks to the even parity of the kurtosis function. Figures 5.6(a), 5.6(c) and 5.6(e) show that the likelihood of extreme fluctuations in the bulk varies with supercriticality. In Figs. 5.6(b), 5.6(d) and 5.6(f), we plot the kurtosis values at mid-height as a function of Ra/Ra_c for all cases.

In the cellular and columnar regimes at $Pr \approx 5$, all values of kurtosis (T_{KURT}, w_{KURT} and $\omega_{z,\mathrm{KURT}}$) increase with supercriticality, in accordance with an increase in the magnitude of the fluctuations of temperature (see Fig. 5.1(d)), vertical velocity (Fig. 5.1(c)) and vertical vorticity. In the plumes regime, T_{KURT}, w_{KURT} and $\omega_{z,\mathrm{KURT}}$ decrease with Ra/Ra_c, as the turbulence in the bulk increases due to the interaction between the plumes. This is also observed for plumes at $Pr = 100$ (green symbols in Figs. 5.6(b), 5.6(d) and 5.6(f)). In the regime of large-scale vortices at both $Pr \approx 5$ and 0.1, the distribution of temperature and vertical velocity is, or is close to, Gaussian, i.e. $T_{\mathrm{KURT}} \to 3$ and $w_{\mathrm{KURT}} \approx 3$; the latter resembles the velocity distribution for turbulent flows. These changes of w_{KURT} with Ra/Ra_c are also reported in Ref. [41] at various Prandtl numbers. In this regime, the vertical-vorticity kurtosis, on the other hand, remains larger than 3: $\omega_{z,\mathrm{KURT}} \approx 4$ and potentially increasing at $Pr \approx 5$, and increasing $\omega_{z,\mathrm{KURT}} > 5$ at $Pr = 0.1$. This indicates that, in the LSV regime, the likelihood of large values of vertical vorticity increases with supercriticality, as observed in turbulent flows. In the rotation-affected regime at $Pr = 0.1$, the turbulent bulk yields a Gaussian distribution for temperature and vertical velocity ($T_{\mathrm{KURT}}, w_{\mathrm{KURT}} \approx 3$). Conversely, the vertical-vorticity kurtosis is larger than 3, revealing that extreme values of ω_z are more likely to occur in this regime. Furthermore, this tendency appears to be constant, i.e. $\omega_{z,\mathrm{KURT}} \approx 10$, for all cases in this regime.

In Fig. 5.7, we plot the kurtosis values at the bottom kinetic boundary layer against the supercriticality of the flow (dark-coloured symbols; light-coloured symbols are kurtosis values at the top kinetic boundary layer). At $Pr \approx 5$, in the cellular and columnar regimes, the behaviour of T_{KURT}, w_{KURT} and $\omega_{z,\mathrm{KURT}}$ is similar to that in the bulk. That is, these quantities increase with Ra/Ra_c within these regimes. For plumes at $Pr \approx 5$, similar to the bulk, the kurtosis

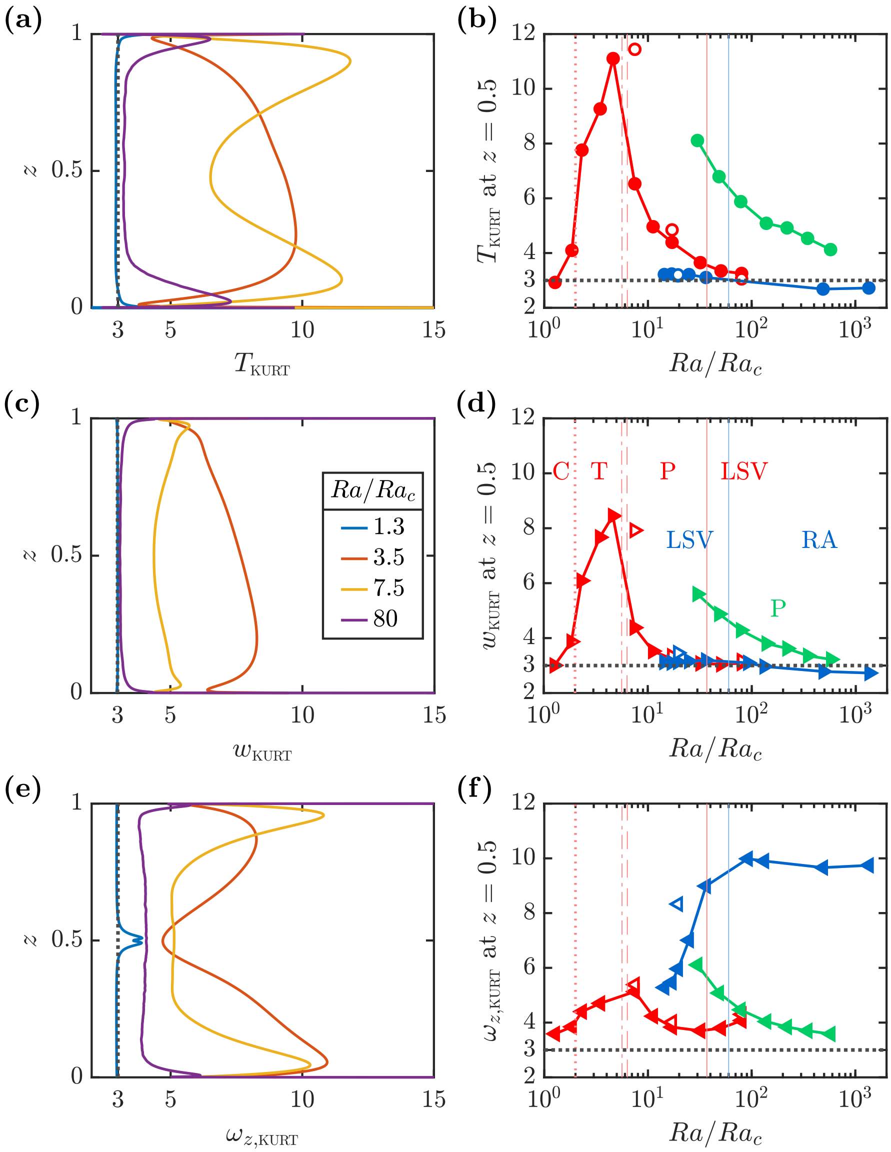

Figure 5.6.: *Vertical profiles of kurtosis of (a) temperature, (c) vertical velocity and (e) vertical vorticity, for selected cases at $Pr \approx 5$. (b) Temperature, (d) vertical-velocity and (f) vertical-vorticity kurtosis at mid-height ($z = 0.5$) plotted against Ra/Ra_c for all simulation cases. Filled and open symbols are for no-slip and stress-free simulations, respectively. Red, green and blue symbols are cases at $Pr \approx 5$, 100 and 0.1, respectively. Colour-coded vertical lines and regime labels are as in Fig. 4.3.*

values decrease with Ra/Ra_c close to the wall. This indicates that, also in the near-wall region, the likelihood of large values of temperature, vertical velocity and vertical vorticity decreases with supercriticality. For plumes at $Pr = 100$, the behaviour of T_{KURT}, w_{KURT} and $\omega_{z,\text{KURT}}$ is markedly different (also different from its behaviour in the bulk). We observe that T_{KURT} and w_{KURT} increase with Ra/Ra_c instead, whereas $\omega_{z,\text{KURT}} \approx 5$ remains approximately unchanged for the parameter values considered. This implies that, for plumes at this Prandtl number, there is an increasing probability of localised hot rising fluid near the bottom (with nearly invariable likelihood of large values of cyclonic vorticity), consistent with positive T_{SKEW}, w_{SKEW} and $\omega_{z,\text{SKEW}}$ (Figs. 5.4(b), 5.4(d) and 5.4(f)). This can be understood as the prevalence of coherent, longer-lived flow structures near the walls owing to the larger Prandtl number. In the LSVs regime at $Pr \approx 5$ and 0.1, the vertical-velocity kurtosis presents considerable differences in comparison to the bulk: it is larger than 3 and increases with Ra/Ra_c. The increased likelihood of large vertical-velocity fluctuations, as well as vertical-vorticity fluctuations, is consistent with increasingly frequent emergence of localised flows with cyclonic (anticyclonic) vorticity that pump (suction) fluid from (into) the Ekman boundary layer. Whilst these vertical flows develop close to the domain boundaries, their presence may influence the flow far from the walls. In Chapter 6 we discuss the role of these boundary-layer flows in presence of large-scale vortices in the flow. The large values of T_{KURT} at $z = \delta_u$ for LSVs at $Pr = 0.1$ (see Fig. 5.7(a)) are related to the strong asymmetry in the distribution of temperature in this region (T_{SKEW} displays large negative values in Fig. 5.4(b)). Namely, strongly localised parcels of cold fluid (large $T_{\text{SKEW}} < 0$) must necessarily register extreme values of temperature that are well below the mean temperature (large T_{KURT}), whereas extended regions of hot fluid register temperatures much closer to the mean. For instance, in the snapshot of temperature fluctuations shown in Fig. 5.5(g), parcels of fluid with below-average temperature (in blue) occupy 32% of the total cross-sectional area, and whose mean temperature (in absolute terms) that is about two times larger than that for hot parcels (in red). In our two LSV cases at $Pr \approx 5$, the asymmetry of the temperature distribution is small, but seemingly increasing (see Fig. 5.4(b)). We thus expect that the temperature kurtosis for LSVs at $Pr \approx 5$ becomes large with increasing Ra/Ra_c. Finally, in the rotation-affected regime, temperature, vertical velocity and vertical vorticity approach their corresponding statistical distribution for the bulk. That is, Gaussian for temperature and vertical velocity ($T_{\text{KURT}}, w_{\text{KURT}} \to 3$) and larger-than-Gaussian (i.e. $\omega_{z,\text{KURT}} > 3$), but approximately constant for vertical vorticity.

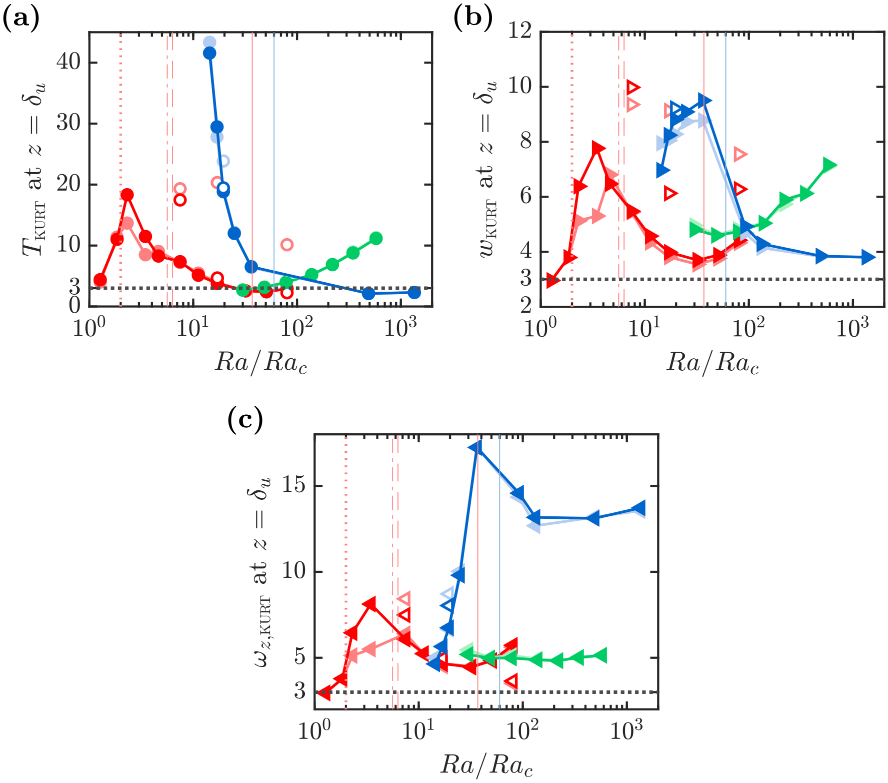

Figure 5.7.: *(a) Temperature, (b) vertical-velocity and (c) vertical-vorticity kurtosis at the bottom kinetic boundary layer ($z = \delta_u$; dark-coloured symbols) and at the top kinetic boundary layer ($z = 1-\delta_u$; light-coloured symbols) plotted against Ra/Ra_c for all simulations cases. Filled and open symbols are for no-slip and stress-free simulations, respectively. Red, green and blue symbols are cases at $Pr \approx 5$, 100 and 0.1, respectively. Colour-coded vertical lines and regime labels are as in Fig. 4.3.*

5.6. Conclusions

We have investigated the flow and temperature features that result from the dynamical balances presented in Chapter 4. For cells and columns, the drop in bulk mean temperature gradient and steep increase of the convective Nusselt number are attributed to the steep increase of the magnitude of temperature and vertical velocity fluctuations. As the coherent columns deteriorate into plumes, these quantities no longer increase. Yet, horizontal velocity fluctuations increase, enough so to enhance horizontal mixing and lead to an increased temperature gradient. Here, the efficiency of the heat transport decreases: from $Nu \sim (Ra/Ra_c)^{2.7}$ in the cellular and columnar regimes to $(Ra/Ra_c)^{0.4}$ in the plumes regime (both scalings at $Pr \approx 5$). For LSVs, T_{RMS} (only for $Pr = 0.1$) and w_{RMS} increase again, enhancing vertical mixing and leading to decreased mid-height temperature gradient. Here, $Nu_* \sim Ra_*^{0.55}$ (Nu_* and Ra_* defined in Section 5.2), in accordance with Ref. [36] within a few percent. For rotation-affected convection (at $Pr = 0.1$), the heat transport scaling is shallower than for LSVs, as it approaches the non-rotating scaling $Ra^{1/5}$ [115, 182–184].

We find that in the geostrophic regime (cells, columns, plumes and LSVs), the kinetic boundary layer thickness scales as $Ek^{1/2}$, a clear indication that this boundary layer is of Ekman type. At larger Ra/Ra_c, beyond the geostrophic regime, for rotation-affected convection, the kinetic boundary layer thickness deviates significantly from the $Ek^{1/2}$ scaling, in agreement with the loss of rotational constraint in this region (discussed in Section 4.4). This change in the dynamics of the near-wall flow is also reflected in the thermal boundary layer: its thickness approaches the non-rotating scaling $\delta_\theta = 1/(2Nu)$ (see Section 2.5).

Overall, the flow and temperature statistics exhibit transitional behaviours at similar Ra/Ra_c for the bulk and near the walls. Nevertheless, their specific patterns (nearly constant, increasing or decreasing) with varying Ra/Ra_c do not always coincide. For LSVs at $Pr \approx 5$, the temperature and vertical velocity distributions in the bulk are Gaussian, a sign of turbulence in this region. At $z = \delta_u$, the distributions are positively skewed and their kurtoses are larger than Gaussian, suggesting the presence of *localised* coherent bursts of hot rising fluid with cyclonic vorticity. Conversely, for LSVs at $Pr = 0.1$, cyclonic vortices with positive thermal contrast are distributed over rather large portions of the horizontal domain. This difference appears to depend on the relative thickness of the kinetic and thermal boundary layers. When the thermal boundary layer is embedded within the kinetic boundary layer, localised Ekman pumping from the kinetic boundary layer is matched by localisation of hot fluid at $z = \delta_u$. In the opposite case, no localisation of thermal structures is observed.

Chapter 6

Large-scale vortices[1]

In this chapter, we investigate the formation of large-scale vortices in presence of no-slip bottom and top boundaries. No-slip boundaries are known to actively promote the formation of plume-like vertical disturbances, through so-called Ekman pumping, that control the ambient flow at sufficiently high rotation rates. Despite this, we demonstrate the presence of competing large-scale vortices (LSVs) in the bulk in simulations at $Pr = 0.1$ *and* ≈ 5*. Strong buoyant forcing and rotation foster the quasi-two-dimensional turbulent state of the flow that leads to the upscale transfer of kinetic energy that forms the domain-filling LSV condensate. The Ekman plumes from the boundary layers are sheared apart by the large-scale flow, yet we find that their energy feeds the upscale transfer. Our results of RRBC simulations substantiate the emergence of large-scale flows in nature regardless of the specific details of the boundary conditions.*

6.1. Introduction

In fluid dynamics, kinetic boundary layers (BLs) adjacent to no-slip surfaces are frictional regions that, despite being relatively thin, can greatly affect the dynamics of the ambient flow. In particular, the so-called Ekman BL in rapidly rotating flows [116] actively enhances vertical velocities far beyond the BL region through Ekman pumping. Likewise, Ekman pumping boosts convective instabilities of the thermal BL in buoyancy-driven flows, a highly relevant problem to many geophysical and astrophysical systems. These flows span the domain height at sufficiently strong rotation [45, 52, 63, 64, 88]. When rotation is much weaker than thermal forcing, however, plumes emerging from the

---

[1] The contents of this chapter have been adopted from A. J. Aguirre Guzmán, M. Madonia, J. S. Cheng, R. Ostilla-Mónico, H. J. H. Clercx, and R. P. J. Kunnen. Competition between Ekman plumes and vortex condensates in rapidly rotating thermal convection. *Phys. Rev. Lett.*, 125(21):214501, 2020 [58], leaving out some introductory parts that have already been covered in this thesis; some symbols have been changed from the article to match with the current notation.

BL organize into a large-scale circulation (LSC) with shearing that ironically sweeps away the plumes formed by the BL [39, 185].

For a surface with stress-free boundary condition, the buoyancy-driven flow fed by the thermal BL is no longer enhanced by Ekman pumping. The thermal plumes are then too weak to affect the ambient flow, which becomes more prone to turbulence under strong thermal forcing. At sufficiently strong forcing and rapid rotation, vertical velocities are largely suppressed, and the resulting turbulent flow is quasi-two-dimensional (Q2D) [41, 44–46, 50, 92]. The flow then mimics pure 2D turbulence with an inverse energy cascade [186, 187]. The upscale energy transfer is eventually balanced by friction in finite-size domains or by imposed large-scale damping. Consequently, energy accumulates at large scales (spectral condensation) and coherent, long-lived large-scale vortices (LSVs; also called vortex condensates) form [188–192]. However, the question is whether similar processes occur for no-slip boundaries; can LSVs sweep away the (Ekman) plumes as the LSC does at low rotation rates? Asymptotic simulations, i.e. valid in the limit of rapid rotation, using parametrized Ekman pumping boundary conditions report upscale transfer of kinetic energy but no persistent LSVs form [51, 113]. In these simulations the kinetic energy of the large-scale, vertically-averaged or (so-called) 2D barotropic flow, associated with the condensate, is reduced by Ekman friction. The kinetic energy of the remaining 3D baroclinic (depth-dependent) convection is enhanced by Ekman pumping at smaller length scales.

Here, we demonstrate for the first time the presence of coherent, long-lived LSVs in rotationally-constrained thermal convection despite Ekman pumping interference from the BLs and frictional drag. We do so for fluids of different Prandtl number (defined below) pertinent to geophysical systems: low $Pr = 0.1$, relevant to liquid metals as in Earth's outer core, and high $Pr \approx 5$, water, popular in experiments and applicable to oceanic processes. We identify nonlocal energy transfer from smaller scales to the largest horizontal scale in the domain, while the Q2D turbulent bulk subdues significant disturbances from the BLs. Our novel observation of LSVs with no-slip walls paves the way to experimentally explore LSV growth in buoyancy-driven rotating turbulence, a process omnipresent in large-scale natural flows. We directly assess the effects of no-slip boundaries on vortex condensates in 3D anisotropic systems.

From our suite of direct numerical simulations with no-slip boundaries (listed in Table 3.1), here we consider those at parameters displayed in Fig. 6.1 (circles). In particular, three reference cases, indicated with stars (Fig. 6.1), are selected for further analysis: LSVs at $Pr = 0.1$, $Ra/Ra_c = 20$ (L01NS; L01SF is a corresponding stress-free run) and at $Pr = 5.2$, $Ra/Ra_c = 80$ (L52NS), and

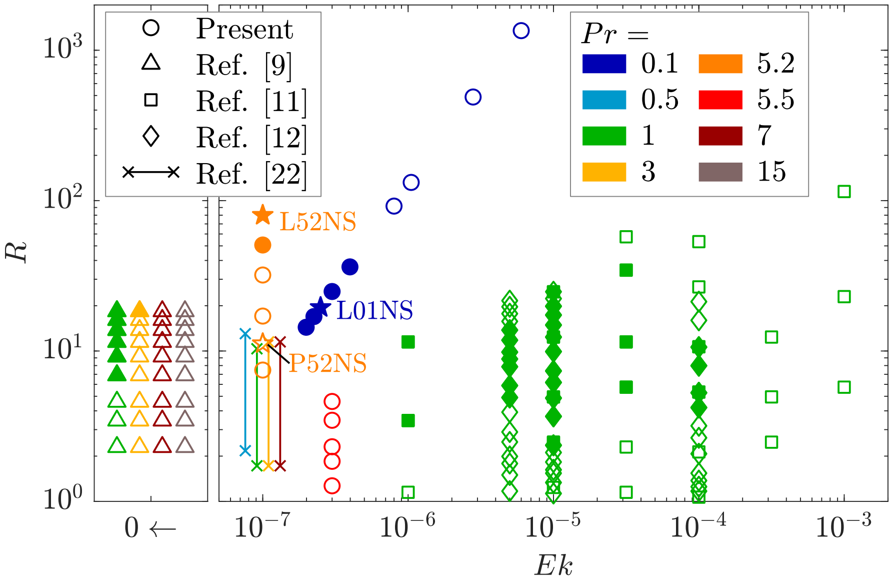

Figure 6.1.: *Phase diagram of rotating convection. Present no-slip DNS; asymptotic ($Ek \rightarrow 0$) simulations, with stress-free [41] and parametrized Ekman-pumping boundaries [51]; stress-free DNS [44, 46]. Filled symbols represent LSV states. Labeled stars are reference cases from the present study.*

plumes at $Pr = 5.2$, $Ra/Ra_c = 11$ (P52NS).

6.2. The quasi-dimensional turbulent state

In the bulk, the relative magnitude of root-mean-square (RMS) horizontal (u_{RMS}) and vertical (w_{RMS}) velocity exhibits significantly different behavior specific to the flow structure that, together with the vertical-velocity kurtosis (w_{KURT}), provides a generic way to distinguish the flow regimes identified in Ref. [41]. For cells (C) and convective Taylor columns (T) vertical velocities are stronger than horizontal, for plumes (P) (and quasi-3D, Q3D, turbulence at $Pr = 0.1$) they are comparable, while for LSVs horizontal velocities are larger (Fig. 6.2). Larger-than-Gaussian kurtosis, i.e., $w_{\mathrm{KURT}} > 3$, indicates increased likelihood of strong vertical velocity fluctuations. Ref. [41] reports $w_{\mathrm{KURT}} > 3$ at mid-height for cells, columns, and plumes, while in the so-called geostrophic turbulence state (where LSVs are observed) $w_{\mathrm{KURT}} \approx 3$ as in homogeneous isotropic turbulence. Our mid-height observations are the same (inset **I** and **II**).

LSV states are emphasized by the decomposition into 2D (vertically av-

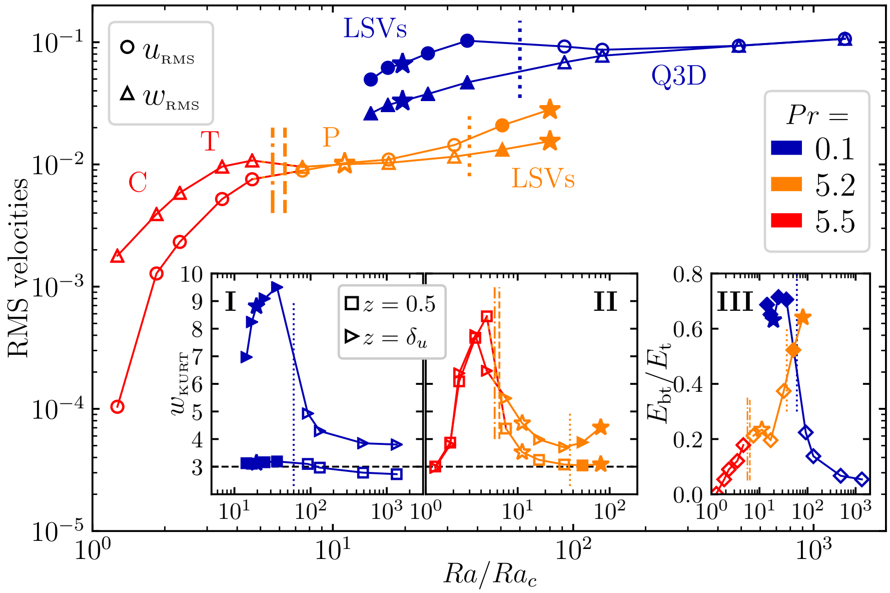

*Figure 6.2.: RMS horizontal (u_{RMS}) and vertical (w_{RMS}) velocities at mid-height ($z = 0.5$) versus Ra/Ra_c (same data as in Fig. 4.5). Vertical dash-dotted and dashed lines indicate predicted transitions from Cells (C)/convective Taylor columns (T) to plumes (P) [71, 132]. Vertical dotted lines are our estimated transitions between plumes and LSVs (orange), and LSVs and Q3D (blue). Inset **I** and **II**: vertical-velocity kurtosis w_{KURT} at mid-height (squares; same data as in Fig. 5.6(d)) and at the kinetic BL thickness ($z = \delta_u$; right triangles; same data as in Fig. 5.7(b)). Horizontal dashed lines at $w_{\mathrm{KURT}} = 3$ indicate Gaussian kurtosis. Inset **III**: ratio of barotropic E_{bt} to total E_{t} kinetic energy. Filled symbols denote LSV cases.*

eraged) barotropic flow and 3D (depth-dependent) baroclinic convection [41, 46, 92]: $\boldsymbol{u} = \langle \boldsymbol{u} \rangle_z + \boldsymbol{u}'$, where $\langle \boldsymbol{u} \rangle_z = \int_0^1 \boldsymbol{u}\, dz$. The ratio of barotropic $E_{\mathrm{bt}} = \frac{1}{2}(\langle u \rangle_z^2 + \langle v \rangle_z^2)$ to total $E_{\mathrm{t}} = \frac{1}{2}\left(u^2 + v^2 + w^2\right)$ kinetic energy is largest for LSVs (inset **III**); the 2D flow dominates as is common in condensate vortices [41, 192, 193]. The large fraction of 2D kinetic energy, larger horizontal than vertical RMS velocity and Gaussian bulk kurtosis are signatures of Q2D turbulence in the LSV flow state.

Near the bottom at height $z = \delta_u$ (the Ekman BL thickness based on the u_{RMS} maxima) kurtosis follows the bulk trend for most of the Ra/Ra_c range, except for LSV states where it remains larger than 3. We hypothesize that deviations from Gaussianity are caused by the prevalence of smaller-scale structures formed by Ekman pumping from the BLs, whose presence, remarkably, does not disrupt the LSVs. This will be addressed later.

6.3. Morphology of the LSVs

Flow visualizations in Fig. 6.3 of the reference cases reveal for both L01NS and L01SF (panels a and b) one large-scale vortical structure with cyclonic (positive) vertical vorticity that extends over the domain height. The vortex is embedded in an environment with weak anticyclonic (negative) vorticity. Figure 6.3(c) shows that L52NS displays both a cyclonic and an anticyclonic vortex. Just as the vortex monopole, the dipole spans the domain height. During the statistically stationary state (approximately 400 convective times H/U_{ff} at $Pr = 0.1$, and about 900 convective times at $Pr = 5.2$), the vortices are long-lived without significant horizontal displacement. For P52NS, in Fig. 6.3(d), plumes dominate the bulk [38, 41, 88].

Cyclonic vortices are favored over anticyclones: when both are present, the anticyclone is weaker than the cyclone. Cyclone–anticyclone asymmetry in rotating flows has been extensively discussed [171, 175, 194, 195]. In Ref. [196] the presence or absence of the anticyclone in vortex condensates is postulated to result from either of two saturation mechanisms of the inverse energy transfer. One of them is due to viscous dissipation at large scales (as in 2D turbulence), and is preferred in the asymptotic limit of rapid rotation. This mechanism allows the development of a vortex dipole, consistent with the cyclone-anticyclone symmetric state observed in Ref. [41, 45, 51, 92]. In the other mechanism, energy saturation occurs when the eddy turnover time of the condensate W/U_{LSV} (W is the domain width and U_{LSV} the characteristic velocity of the condensate) becomes comparable to the rotation rate Ω. In such conditions, the local Q2D conditions in the anticyclone break down, thus strong cyclone-anticyclone asymmetry is expected. For L52NS, the convective Rossby number $Ro_{\mathrm{C}} = Ek\sqrt{Ra/Pr}$ is $Ro_{\mathrm{C}} = 0.017$, which may be low enough to enter the asymptotic symmetric state. For L01NS, $Ro_{\mathrm{C}} = 0.079$ is larger, which may explain the stronger asymmetry.

6.4. Kinetic energy transfer among scales

To study the development of LSVs, we consider the shell-to-shell energy transfer [46, 197–201]. We investigate [92] transfer from baroclinic to barotropic (3D to 2D) flow:

$$T_{\mathrm{bc}}(Q, K) \equiv -\int_V \langle \boldsymbol{u}_K \rangle_z \cdot (\boldsymbol{u}' \cdot \boldsymbol{\nabla}) \boldsymbol{u}'_Q \, dV, \tag{6.1a}$$

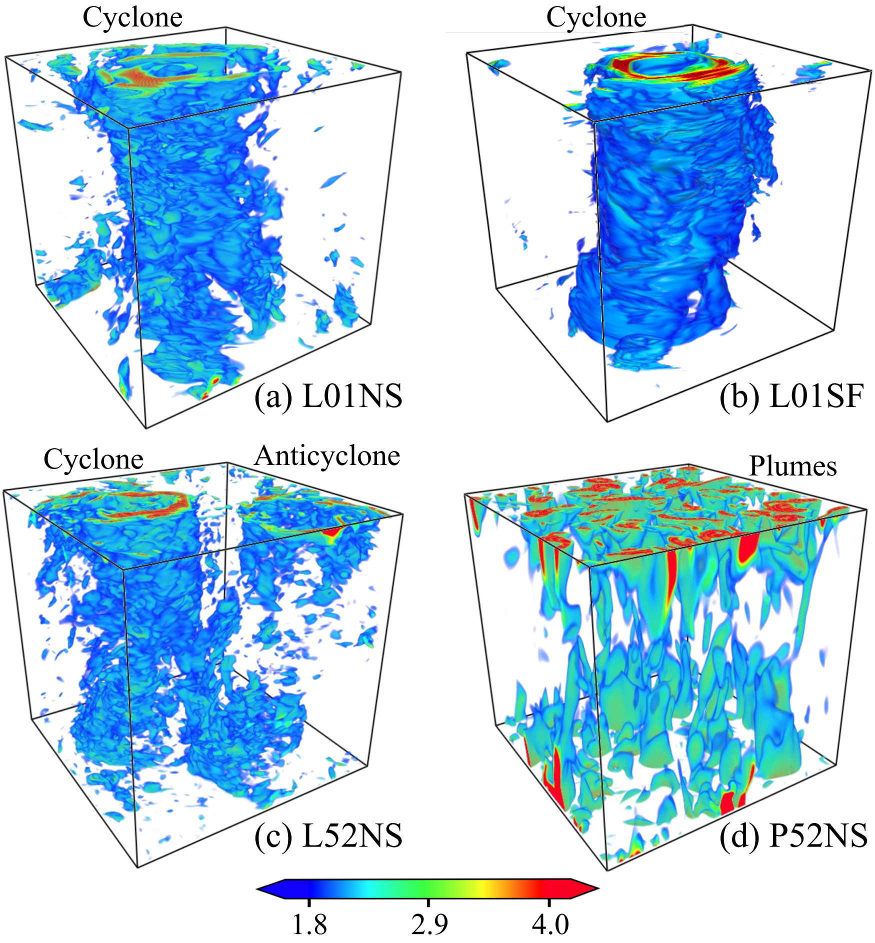

Figure 6.3.: *Snapshots of horizontal kinetic energy* $\frac{1}{2}\left(u^2+v^2\right)$*, scaled by volume-averaged total energy* $\langle E_{\mathrm{t}}\rangle_V$ *for the reference cases. Actual domains are slender; their width-to-height ratio* $\Gamma = W/H = \mathcal{O}(10^{-1})$*. For clarity, they are stretched horizontally by a factor* $1/\Gamma$*.*

and barotropic self-interaction (2D to 2D):

$$T_{\mathrm{bt}}(Q,K) \equiv -\int_V \langle \boldsymbol{u}_K\rangle_z \cdot (\langle \boldsymbol{u}\rangle_z \cdot \boldsymbol{\nabla})\langle \boldsymbol{u}_Q\rangle_z \, dV. \tag{6.1b}$$

The Fourier-filtered 2D field $\langle \boldsymbol{u}_K\rangle_z$ of wavenumber K receives energy from the filtered (2D or 3D) field of wavenumber Q via triadic interactions mediated by the energy giver field; we find that the other transfers to 2D (from 3D mediated by 2D and from 2D mediated by 3D) are negligible. If $T_{\mathrm{bc}}, T_{\mathrm{bt}} > 0$, the mode Q transfers energy to mode K and vice versa. Equations Eqs. (6.1a) and (6.1b) are derived from the budget equation of modal barotropic kinetic energy, where Fourier transforms are performed in the horizontal periodic directions and the Fourier space divided into ring-like shells of different horizontal wavenumbers.

In Fig. 6.4 we plot T_{bc} (left column) and T_{bt} (right column). LSV cases (top three rows) present positive T_{bc} over a wide range of modes $Q \gtrsim 5$ and $K \lesssim 3$, revealing spectrally *nonlocal* upscale transfer of kinetic energy from 3D convection at small scales to the largest 2D scales, i.e., without participation of intermediate scales. We also plot $T_{\mathrm{bc}}^{\geq 5}(K) \equiv \sum_{Q=5}^{40} T_{\mathrm{bc}}(Q,K)/\langle w\theta \rangle_V$ (blue curves), the sum of nonlocal baroclinic transport to mode K, normalized by volume-averaged buoyant energy input $\langle w\theta \rangle_V$ (θ is temperature). The largest contribution is indeed at LSV mode $K = 1$.

For plumes (see Fig. 6.4(g)), a narrower range of baroclinic modes $5 \lesssim Q \lesssim 25$ contributes positively to barotropic modes $2 \lesssim K \lesssim 10$, with virtually no contribution to $K = 1$. We argue that this upscale energy transfer is due to plume–plume interactions and merger (plume scale is $K_p \approx 10$); spectrally local unlike the strong interaction of all Q with $K = 1$ in LSV cases, together with a direct downscale cascade.

In all cases T_{bt} presents positive diagonal $K = Q + 1$, indicating spectrally *local* downscale transfer within the 2D flow. Additionally, LSV cases reveal spectrally nonlocal upscale transfer: positive T_{bt} at $K = 1$ over a wide range of Q modes (likewise, negative T_{bt} for $Q = 1$). Simultaneous downscale and upscale transfers coexist within the 2D flow [92]. Finally, for P52NS (Fig. 6.3(d)), some 2D self-interaction is registered: energy exchanges among plumes lead to short-range upscale transfer toward scales that do not involve the largest scale, with concurrent downscale cascades over a much shorter range than for LSVs.

6.5. Near-walls dynamics

To investigate the near-wall dynamics, we calculate the (nondimensional) height-dependent planar kinetic energy budget [157, 202, 203]:

$$\mathcal{B} + \mathcal{T} + \mathcal{P} + \mathcal{V} - \mathcal{D} = 0, \tag{6.2}$$

where $\mathcal{B} \equiv \langle w\theta \rangle_P$ is buoyant production, $\mathcal{T} \equiv -\partial_z \langle w E_t \rangle_P$ turbulent transport, $\mathcal{P} \equiv -\partial_z \langle wp \rangle_P$ pressure transport, $\mathcal{V} \equiv 2\sqrt{Pr/Ra}\,\partial_z \langle u_i s_{i3} \rangle_P$ viscous transport and $\mathcal{D} \equiv \langle \epsilon \rangle_P = 2\sqrt{Pr/Ra} \langle s_{ij} s_{ij} \rangle_P$ dissipation rate [131]. $\langle \cdot \rangle_P$ denotes horizontal planar averaging, p is pressure and $s_{ij} = \frac{1}{2}(\partial_j u_i + \partial_i u_j)$. Summation is over repeated indices, $i = 1, 2$ denote horizontal directions and $i = 3$ vertical direction ($u_3 = w$). We normalize all terms with $\langle w\theta \rangle_V$. $\mathcal{B}$ indicates

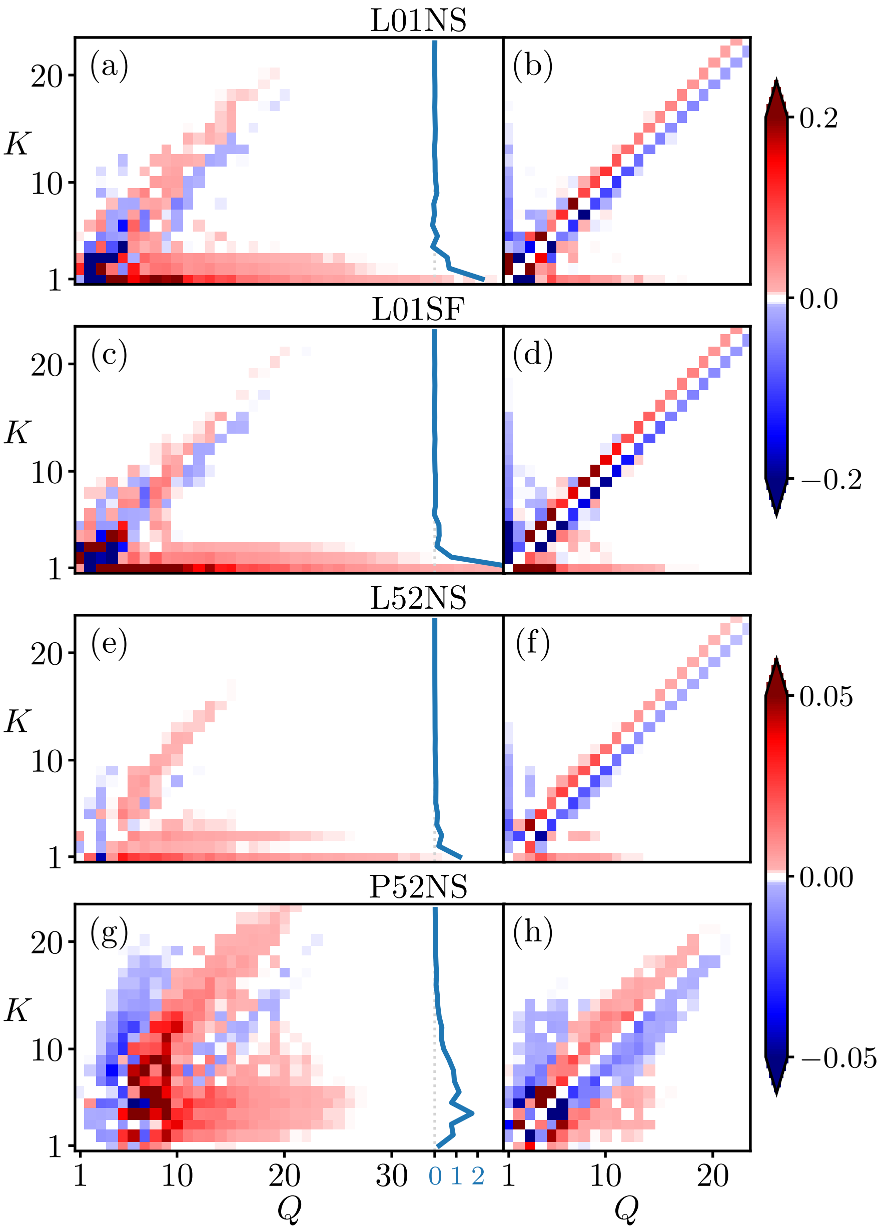

Figure 6.4.: Spectral kinetic energy transfer T_{bc} from (baroclinic) 3D mode Q to (barotropic) 2D mode K (first column) and T_{bt} between (barotropic) 2D modes Q and K (second column), normalized by mean buoyant energy input $\langle w\theta\rangle_V$, for the reference cases. Blue curves represent $T_{\mathrm{bc}}^{\geq 5}(K)$.

energy input; transport terms ($\mathcal{T}, \mathcal{P}, \mathcal{V}$) redistribute kinetic energy vertically; $\mathcal{D}$ extracts energy.

Fig. 6.5 shows the z-dependent budgets for the reference cases; left column for lower half of the domain, right column zoomed in on the bottom BL. For all cases, $\mathcal{B}$ provides energy in the bulk. For L01SF, this energy input is nicely balanced by dissipation, i.e. $\mathcal{D} \approx \mathcal{B}$, whereas $\mathcal{D} < \mathcal{B}$ for no-slip cases. There, $\mathcal{B}$ is compensated by large $\mathcal{D}$ near the walls, as $z/\delta_u \to 0$. The difference between $\mathcal{B}$ and $\mathcal{D}$ in the bulk is redistributed toward the BLs by $\mathcal{P}$; the other two transport terms are marginal and only participate near the walls. For LSVs, this extraction may slightly reduce the amount of energy available for interscale exchanges, but does not prevent its spectral transfer upscale. To emphasize this, we co-plot with blue curves the height-dependent transfer to 2D mode $K = 1$, $T_{\mathrm{bc}}^{\geq 5,1}(z) \equiv \sum_{Q=5}^{40} T_{bc}(Q, K = 1, z)/\langle w\theta \rangle_V$. We find predominantly positive $T_{\mathrm{bc}}^{\geq 5,1}$ throughout the bulk for LSVs, and vanishingly small $T_{\mathrm{bc}}^{\geq 5,1}(z)$ where no large scales develop.

Near the no-slip walls (in Figs. 6.5(b), 6.5(f) and 6.5(h)), the budget resembles that of rotationally constrained flows [157]: pressure transport supplies energy to sustain the Ekman BL against frictional dissipation [116], viscous transport redistributes energy within the BL, while turbulent transport has little to no contribution to the budget. Notably, for LSVs (in Figs. 6.5(b) and 6.5(f)), no 3D-to-2D upscale transfer is sustained within the BL: $T_{\mathrm{bc}}^{\geq 5,1} < 0$ for $z < \delta_u$. Instead, the 2D mode loses energy to smaller-scale 3D motions. $T_{\mathrm{bc}}^{\geq 5,1} > 0$ for $z > \delta_u$ and, strikingly, it peaks just outside the BL to reduce (but remain positive) toward the bulk. As vertical bursts from the BL ($w_{\mathrm{KURT}} > 3$ at $z = \delta_u$, see Fig. 6.2) are sheared apart by the strong horizontal bulk flow, their energy feeds the upscale transfer to the 2D LSV just outside the BL. The thermal BL has no noticeable effect on these profiles.

6.6. Conclusions

We demonstrate that Ekman BLs cannot prohibit LSV formation in no-slip RRBC. They, instead, postpone the occurrence of upscale energy transfers to significantly higher rotation rates (at the same supercriticality) than for stress-free boundaries; vertical bursts due to Ekman pumping require stronger rotational constraint to be diverted into upscale transfer to LSVs. Ekman plumes are swept away by large horizontal velocities from the emerging LSVs. The role of the Prandtl number is similar for no-slip as for stress-free simulations: LSV formation is more easily reached at smaller Pr [41]. We postulate that coherent plumes, formed by the Ekman BLs, with strong temperature contrast,

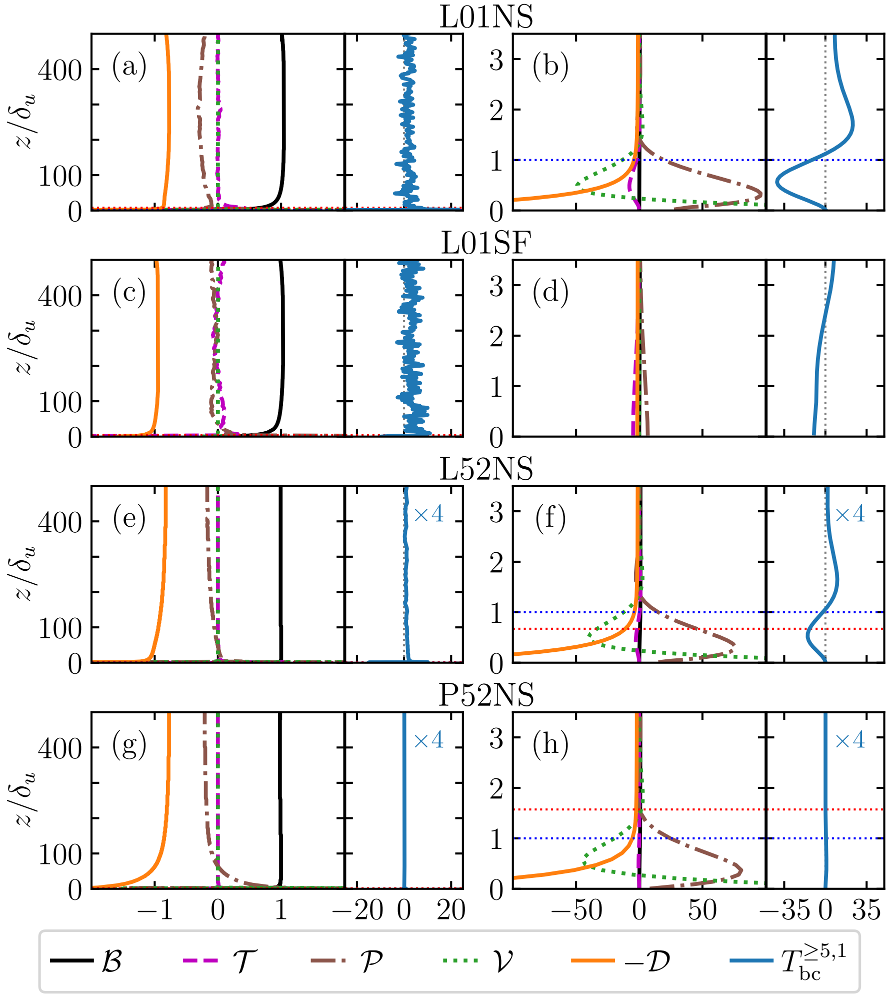

Figure 6.5.: *Kinetic energy budget in the bulk (left column) and near the bottom (right column) for the reference cases. Vertical coordinate scaled by kinetic BL thickness* δ_u *(for L01SF we use* δ_u *from L01NS). Profiles shown for lower half of the domain; mid-height* $z/\delta_u \approx 400$ *for all cases. Dotted blue (red) horizontal lines denote kinetic (thermal) BL thicknesses. The thermal BL is thicker than the plotting interval in (b,d). Blue curves indicate height-dependent nonlocal energy transfer* $T_{\mathrm{bc}}^{\geq 5,1}(z)$ *from 3D modes* $5 \leq Q \leq 40$ *to 2D LSV mode* $K = 1$.

are longer-lived at high Pr given weaker thermal diffusion. Hence they can more proficiently disturb LSV formation.

Large-scale flow organization is ubiquitous in geophysics and astrophysics. Our study identifies that Ekman boundary layers are unable to prevent vortex condensation, opening up laboratory modeling of these flows in the rotating Rayleigh–Bénard configuration [128]. We provide firm evidence that large-scale vortex condensation can develop regardless of the boundary conditions.

Chapter 7

RRBC in a cylinder: the sidewall circulation[1]

This chapter deals with the effect of lateral boundaries in rotating Rayleigh–Bénard convection. In particular, we study the recently observed discrepancy in total heat transport between experiments on a confined cylindrical domain and simulations on a laterally unconfined periodic domain. Near the sidewalls, we find a region of enhanced convection, the sidewall circulation. The sidewall circulation rotates slowly within the cylinder in anticyclonic direction. Through separate analysis of the sidewall region and the inner bulk flow, we find that at larger thermal forcing the heat transport in the inner part of the cylindrical domain, outside the sidewall circulation region, coincides with the heat transport on the unconfined periodic domain. Thus the sidewall circulation accounts for the differences in heat transfer between the two considered domains, while in the bulk the turbulent heat flux is the same as that of a laterally unbounded periodic domain. We also provide experimental evidence for the existence of the sidewall circulation that is in close agreement with the simulation results.

7.1. Introduction

Recent studies of rotating Rayleigh–Bénard convection at high rotation rates and strong thermal forcing have shown a significant discrepancy in total heat transport between experiments on a confined cylindrical domain on the one hand and simulations on a laterally unconfined periodic domain on the other. This chapter addresses this discrepancy using direct numerical simulations on a cylindrical domain.

---

[1] The contents of this chapter have been adopted from X. M. de Wit, A. J. Aguirre Guzmán, M. Madonia, J. S. Cheng, H. J. H. Clercx, and R. P. J. Kunnen. Turbulent rotating convection confined in a slender cylinder: The sidewall circulation. *Phys. Rev. Fluids*, 5(2):023502, 2020 [53], leaving out the introductory parts that have already been covered in this thesis; some symbols have been changed from the article to match with the current notation.

A popular geometry for the study of RRBC using numerical simulation is the horizontally periodic plane layer, for both direct numerical simulations (DNSs) [31, 32, 44–46, 50, 78, 204] and simulations of asymptotically reduced models [33, 41, 45, 51, 100]. The main advantage is that no lateral constraint needs to be applied: the use of sidewalls could affect the flow development by choice of shape (e.g. square cuboid or cylinder) as well as by choice of boundary condition (no-slip or stress-free; zero-heat-flux or constant temperature). In contrast, experiments must resort to lateral confinement, where an upright cylinder is by far the most popular geometry [7, 35, 38, 64, 71, 73]. In that case a parameter describing the geometry is required, for example the diameter-to-height aspect ratio $\Gamma = D/H$. In fact, to push the performance of experiments towards planetary conditions the height of convection experiments has grown, while the diameter remains rather small [71, 76, 128].

There are several issues specific to experiments that can occur in such systems. Examples include centrifugal buoyancy [205, 206] and so-called non-Oberbeck–Boussinesq effects [47]. But it turns out that the choice of domain can also have profound effects.

The starting point for the current investigation is a comparison of results from direct numerical simulations in a horizontally periodic domain and from experiments in an upright cylinder. The efficiency of the convective heat transfer is commonly expressed as the Nusselt number $Nu = q/q_{\mathrm{cond}}$, the total heat flux q normalized by the conductive flux $q_{\mathrm{cond}} = k\Delta T/H$; k is the thermal conductivity of the fluid. In Fig. 7.1 we compare the Nusselt number from experiments and direct numerical simulations in horizontally periodic domains. All datapoints are for water ($Pr \approx 5$) and at constant $Ek = 10^{-7}$. The two experiments included in the plot, TROCONVEX (Eindhoven) [76, 128] and RoMag (UCLA) [71], align nicely, as do the two numerical studies (Stellmach et al. [45] and the current study). However, for $Ra > 10^{11}$ there is a gap in Nu between numerical and experimental data (i.e. cylinder and periodic layer), roughly a factor two in magnitude. This discrepancy is unexpected: as the cylindrical domains in experiments were always wide enough to accommodate many times the characteristic horizontal convective scale [128], no confinement effects were anticipated.

In this chapter we want to explain this discrepancy using a set of DNSs at the same operating conditions as the experiments and now in the same domain shape and boundary conditions, i.e. a cylinder of aspect ratio $\Gamma = 1/5$. We find a good agreement between DNS and experiments in the same domain. The discrepancy in heat transfer between the two domains used for DNS (i.e.

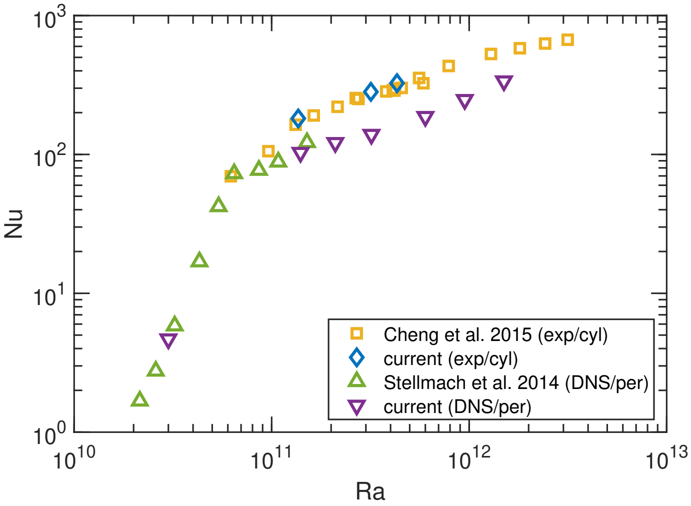

Figure 7.1.: *Comparison of Nusselt number results from experiments in a cylinder (Cheng et al. 2015 [71] and the current work) and DNS on a horizontally periodic domain (Stellmach et al. 2014 [45] and the current work) as a function of the Rayleigh number. All simulations adopt constant* $Ek = 10^{-7}$ *and* $Pr \approx 5$ *for water.*

cylinder and horizontally periodic layer) is shown to be caused by a strong circulation that is formed on the sidewall and significantly contributes to the overall heat flux. However, when excluding the sidewall region, we recover identical heat transfer for the bulk of the cylinder and the horizontally periodic layer.

A recent paper [55] describes a similar flow feature. While further in-depth comparison is required given that the parameter values used are quite far apart, it is expected that the same feature of confined rotating convection is studied. Hence we will identify similarities and differences between our findings and those reported in [55]. The two studies give complementary views on this interesting flow structure with obvious consequences for the interpretation of experiments.

7.2. Numerical and experimental methods

The numerical simulations presented here are done using two codes: the cylinder code and the multiple-grid Cartesian code, both described in Section 3.2. In the cylinder code the domain is a slender upright cylinder with $\Gamma = 1/5$. Boundary conditions at the bottom, top and sidewalls are described in Section 3.4. The simulations have been performed at parameter values displayed in Table 3.2.

On the other hand, the simulations in the horizontally periodic domain are those at $Pr = 5.2$ reported in Table 3.1.

The experimental results are from TROCONVEX, the setup in Eindhoven. It is described in [76,128]. It is a slender cylinder of diameter $D = 0.39$ m consisting of four segments, allowing for different working heights. The measurements in this work are taken in a cylinder of $H = 2$ m with $\Gamma = 0.195$. The cylinder is enclosed by copper plates. The bottom plate is electrically heated while the top plate is kept at a constant temperature by circulation of cooling water from a chiller/thermostatic bath combination. The cylinder is encapsulated in insulation foam surrounded by active heat shields that take on the same temperature measured by thermistors in the sidewall; the entire height is divided into five different shields, each connected to two thermistors measuring the temperature at that height. Similarly, there is an active heater below the bottom plate that adapts to the same temperature as the bottom plate. This arrangement minimizes outward conductive losses and is the standard for precise heat-flux measurements. Note that the sidewall thermistors turn out to be interesting for flow diagnostics too. For the three measurements considered here $Ek = 10^{-7}$ and the mean temperature is $T_m = 31.0°\mathrm{C}$, so $Pr = 5.2$. To ease comparison we shall also nondimensionalize the experimental data using the cell height $H = 2$ m, applied temperature difference $\Delta T = \{0.63,\ 1.47,\ 1.99\}°\mathrm{C}$ and convective time $\tau_c = H/U = \{32.1,\ 21.0,\ 18.1\}$ s for $Ra = \{1.4,\ 3.2,\ 4.3\} \times 10^{11}$, respectively. From here on all quantities are expressed in these units. Note that we renormalize the radial coordinate with the radius $R = D/2$, so that $r/R = 1$ on the sidewall, for ease of interpretation.

7.3. Instantaneous snapshots

From the cylinder DNS we can get detailed information on the flow field. To start the exploration, we show instantaneous cross-sections displaying the vertical component of velocity for $Ra = 5.0 \times 10^{10}$ and 4.3×10^{11} in Fig. 7.2. Horizontal cross-sections at $z/H = 0.5$ and vertical cross-sections are included. The Rayleigh number has a significant effect on the overall flow field: at the lower Ra rotation is stronger than buoyancy and vertical alignment along the rotation axis is enforced, while at the higher Ra there is more three-dimensional dynamics. This effect is well-known from previous studies [41,45,71] where the overall flow phenomenology was characterized. At this Ek, for $Ra \lesssim 1.1 \times 10^{11}$ (based on the empirical relation Eq. (19) of [71]) we expect to recover the convective-Taylor-column (CTC) regime, with plumes taking the shape of columnar vortical chimneys connecting both boundary layers and shielded with

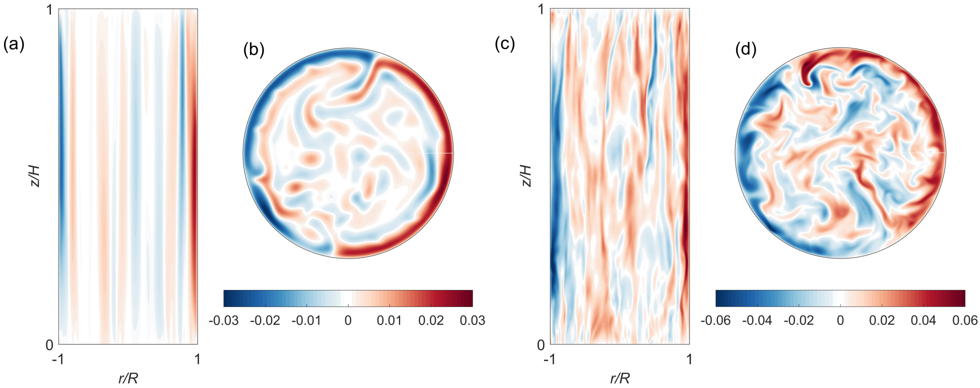

Figure 7.2.: *Snapshots of vertical velocity u_z/U from the simulations at (a,b) $Ra = 5 \times 10^{10}$ and (c,d) $Ra = 4.3 \times 10^{11}$. Panels (a,c) display vertical cross-sections where the horizontal direction has been stretched by a factor two for clarity; panels (b,d) are horizontal cross-sections at $z/H = 0.5$.*

patches of opposite vorticity. The 'torsional' nature of the columns [89, 154], with vertical vorticity changing sign from cyclonic to anticyclonic while crossing the vertical extent of the domain, is confirmed with plots of vertical vorticity (not shown here). The simulation at $Ra = 7.0 \times 10^{10}$ also renders a CTC-type flow. At higher $Ra \gtrsim 1.5 \times 10^{11}$ the vertical coherence is relaxed, but still the dominant force balance is the geostrophic balance between Coriolis and pressure gradient. This flow regime is referred to as plumes [41, 45, 71]. At $Ra = 1.4 \times 10^{11}$ (not shown) some columns can be found but the columnar structure is falling apart, hence a transitional state. For the two highest-Ra cases considered here we recover a flow as displayed in Fig. 7.2(c,d), belonging to either plumes or geostrophic-turbulence regimes [33, 41, 71, 128] that are difficult to discern by eye (and which is not our current objective).

However, all simulations share a predominant flow feature: there is a region of large vertical velocity near the sidewall. This represents a structure of fluid flowing up along one side of the wall and down along the opposite side. It can be observed throughout almost the full vertical extent of the domain; it is only close to the Ekman layers that the prominence of this flow is reduced. We will refer to this flow feature as the sidewall circulation. Zhang et al. [55] coined it the boundary zonal flow (BZF); here we shall not adopt that name given the different results from the analysis of the sidewall flow feature that we will indicate later, which could also indicate different structures. Nevertheless, here, as in [55], the sidewall circulation contributes significantly to the overall heat transfer.

7.4. Size of the sidewall circulation

The definition of the size of a boundary layer like this is quite ambiguous. Different definitions may be used, see e.g. the various definitions of the thermal boundary layer thickness as compared in [41]. Zhang et al. [55] have introduced four definitions that we will also apply (all evaluated at mid-height $z/H = 0.5$):

- δ_0, where the time-and-azimuthally averaged azimuthal velocity $\langle u_\phi \rangle_{t,\phi}$ is zero;
- $\delta_{u_\phi^{\max}}$, where $\langle u_\phi \rangle_{t,\phi}$ reaches its maximum;
- $\delta_{\mathcal{F}_z}$, where the normalized local vertical heat flux $\mathcal{F}_z = [u_z(T - T_m) - \kappa \partial T/\partial z]/(\kappa \Delta T/H)$ attains its maximum, with $T_m = (T_{\text{bottom}} + T_{\text{top}})/2$ the mean temperature of bottom and top plates.
- $\delta_{u_z^{\text{rms}}}$, where the root-mean-square (rms) vertical velocity is maximal;

Additionally, we consider three more boundary layer scales:

- $\delta_{u_\phi^{\text{rms}}}$, location of the maximal azimuthal rms velocity;
- $\delta_{T^{\text{rms}}}$, location of the maximal rms temperature;
- $\delta_{u_{z,\min}^{\text{rms}}}$, the location of the near-wall minimum of u_z^{rms}.

The boundary layer scales are plotted as a function of Ek in Fig. 7.3(a); We plot the radial dependence of u_z^{rms} for the considered simulations in Fig. 7.3(b) to further illustrate the definition of $\delta_{u_{z,\min}^{\text{rms}}}$. We note that the measures based on azimuthal averaging of azimuthal velocity disregard some of the more complex features of the circulation, as will be shown in Section 7.6. The measures based on peak rms velocity and peak heat flux are quite similar overall and in line with earlier studies on sidewall Stewartson boundary layers in rotating cylindrical convection [38, 69, 121, 207], with a thickness scaling as $\delta_S/H \sim (2Ek)^{1/3}$ (that we cannot validate here) or $\delta_S/R \sim (2/\Gamma)(2Ek)^{1/3}$ and a prefactor of about 1. Here we choose the local minimum in u_z^{rms} for further analysis, as we found that it captures the full near-wall heat-flux peak in Fig. 7.3(b). This boundary layer thickness changes with Ra: a power-law fit results in $\delta_{u_{z,\min}^{\text{rms}}}/R = (3 \pm 1) \times 10^{-3} \cdot Ra^{0.15 \pm 0.02}$.

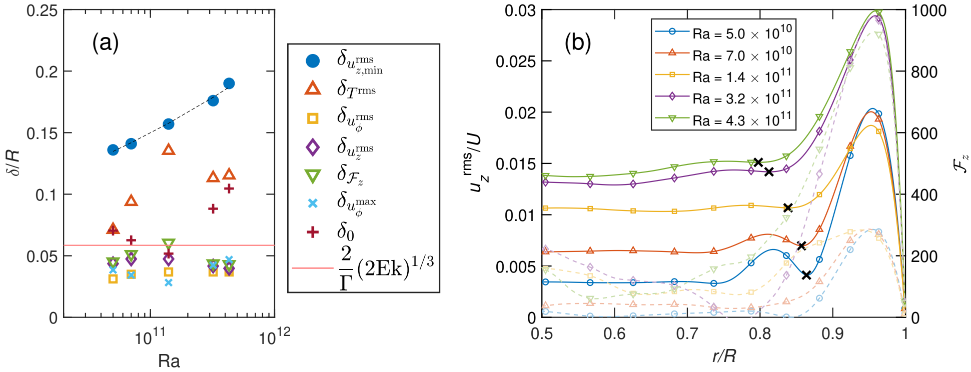

Figure 7.3.: *(a) Various boundary-layer scales evaluated at different Ra. The definitions are introduced in the text; the horizontal line indicates the boundary layer thickness* $\delta_S/R = (2/\Gamma)(2Ek)^{1/3}$ *reported to be a good fit to the sidewall boundary layer thickness in previous studies [38, 69, 121, 207]. The black dashed line is a power-law fit* $\delta_{u_{z,\min}^{\mathrm{rms}}}/R = (3 \pm 1) \times 10^{-3} \cdot Ra^{0.15\pm0.02}$*. (b) Radial dependence of* u_z^{rms} *(solid lines with dark shading; left ordinate) and* $\mathcal{F}_z$ *(dashed lines with light shading; right ordinate) at* $z/H = 0.5$*. The black crosses indicate the positions of the local minima in* u_z^{rms}*, the distance of these points to the sidewall is called* $\delta_{u_{z,\min}^{\mathrm{rms}}}$*.*

7.5. Dynamics of the sidewall circulation

From movies of the vertical velocity in a horizontal cross-sectional plane (see Appendix A) it is clear that the sidewall circulation rotates anticyclonically (i.e. counter to the rotation of the cylinder) in the co-rotating frame of reference used for the simulations. As is customary in experiments and simulations to study the large-scale circulation typical for non- and weakly rotating convection [207, 208], we use the azimuthal profile of vertical velocity at $r/R = 1 - \frac{1}{2}\delta_{u_{z,\min}^{\mathrm{rms}}}/R$ and $z/H = 0.5$ from our simulations to fit a cosine function $u_z(\phi, t) \sim \cos(\phi - \phi_0(t))$ to determine the phase angle $\phi_0(t)$ of the sidewall circulation. In Fig. 7.4(a) we plot ϕ_0 as a function of (convective) time t/τ_c. In all cases the graphs display a trend towards negative ϕ_0, i.e. anticyclonic precession. To quantify the drift rate we fit lines to $\phi_0(t)$; the slope ω_{sc} is negative and its dependence on Ra is displayed in Fig. 7.4(b). Note that we plot $|\omega_{\mathrm{sc}}|H^2/\nu$ to express the rotation rate nondimensionalized using the inverse viscous time $1/\tau_\nu = \nu/H^2$ rather than the convective unit $1/\tau_c = (g\alpha\Delta T/H)^{1/2}$; the viscous unit retains the same value in all simulations while τ_c changes with Ra. The rotation rate of the sidewall circulation increases quite rapidly as Ra is enhanced, but it must be said that in all cases this azimuthal drift is still more than two orders of magnitude slower than the rotation rate of the cylinder (which is $1/(2Ek) = 5 \times 10^6$ in the same units).

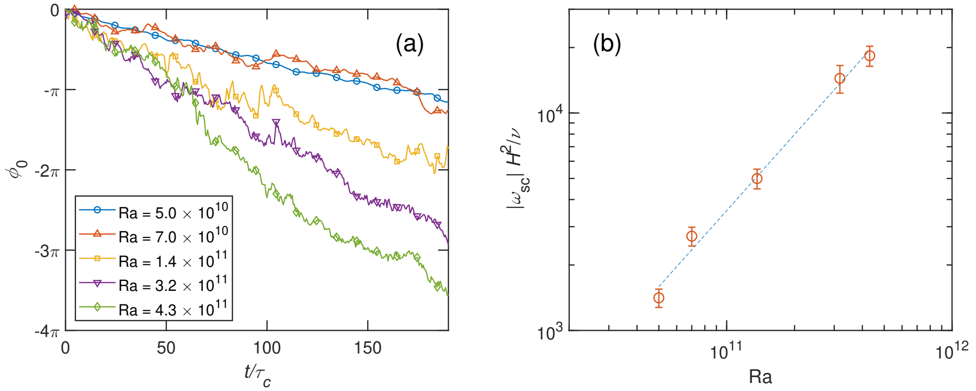

Figure 7.4.: *(a) Radial drift of the sidewall circulation: phase angle ϕ_0 as a function of time t/τ_c. (b) Angular velocity $|\omega_{\rm sc}|$ expressed in viscous units (which are independent of Ra) as a function of Ra. The error bars represent the standard deviation of the angular velocities determined for six equal parts of the total time. The dashed line displays a power-law fit $|\omega_{\rm sc}|H^2/\nu = 6 \times 10^{-10} \cdot Ra^{1.16\pm0.06}$.*

7.6. Orientation-compensated mean flow structure of the sidewall circulation

To understand the azimuthal drift and the enhanced near-wall heat transfer, we want to identify the circulation set up inside the sidewall circulation region. The mean flow pattern can be identified by an orientation-compensating shift followed by averaging, i.e. we rotate instantaneous horizontal cross-sections counter to their corresponding $\phi_0(t)$ before performing an ensemble average of the flow field. The averaged snapshots provide detailed information on the mean flow pattern of the sidewall circulation, as displayed in Fig. 7.5. The lowest and highest Ra simulations are visualized here. Temperature is not included; temperature fluctuations around the mean for each height are distributed similarly to vertical velocity u_z. What can be observed is a geostrophic bulk (i.e. velocity components are mostly independent of the vertical coordinate), surrounded by a two-layer (inner and outer), two-halves (left and right parts of the panels in Fig. 7.5) sidewall boundary layer. Within this boundary layer the azimuthal velocity u_ϕ displays up–down antisymmetry with respect to the midplane $z/H = 0.5$, while the vertical velocity u_z is vertically symmetrical. The radial velocity u_r in the boundary layer region is prominent in two spots located at the top and bottom of the panels in Fig. 7.5, where again approximate up–down antisymmetry can be observed. The two-halves structure is the reason why we want to avoid defining the thickness of the layer using azimuthal

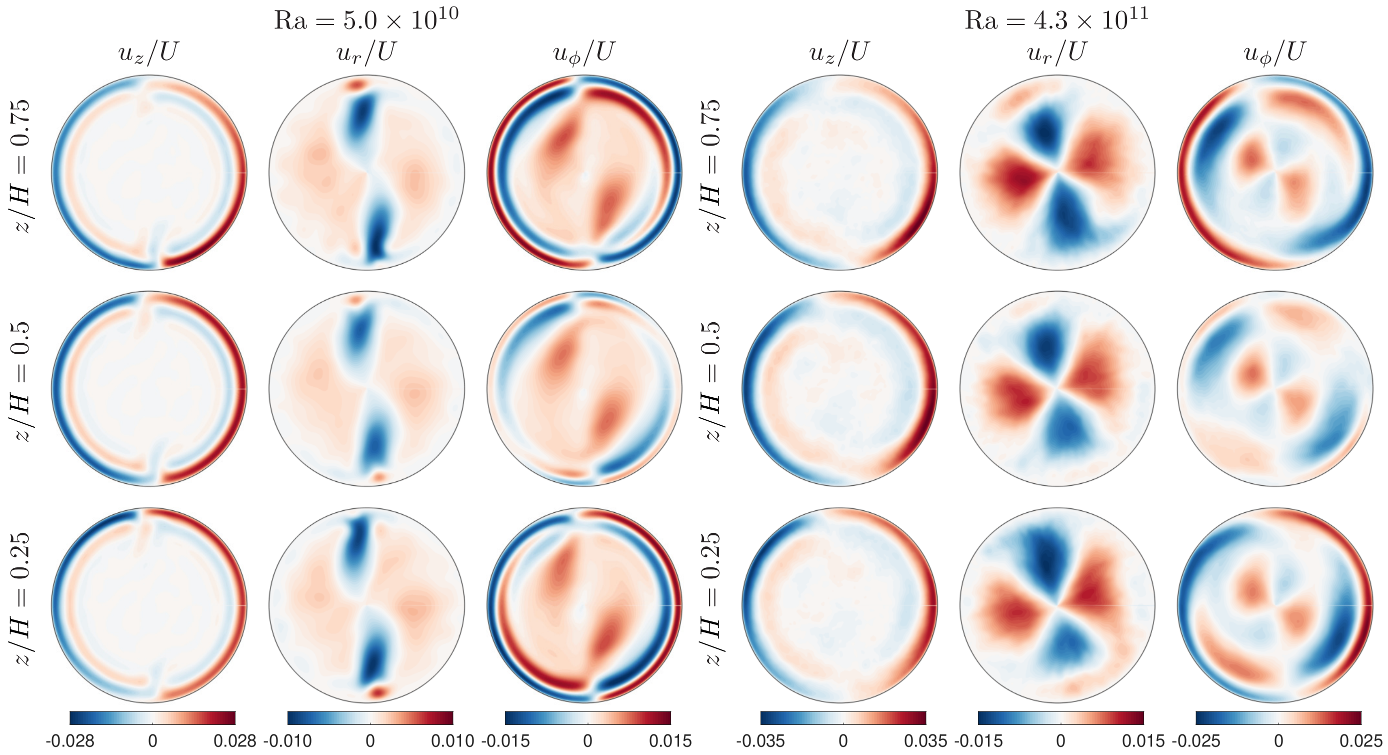

Figure 7.5.: *Orientation-compensated mean velocity fields in horizontal cross-sections at heights* $z/H = 0.25$, 0.5 *and* 0.75 *for two Rayleigh numbers* 5.0×10^{10} *(left) and* 4.3×10^{11} *(right). The vertical* (u_z)*, radial* (u_r) *and azimuthal* (u_ϕ) *velocity components are shown.*

averaging of u_ϕ; there is only a minor asymmetry between the two halves, the mean of which does not correctly convey the size. Azimuthal averaging washes away all of the interesting azimuthal structure revealed here. Appendix A displays this effect for the azimuthally averaged u_ϕ at $z/H = 0.5$.

In both displayed Ra cases we observe a radial structure for u_z that consists of two layers of opposite sign akin to the Stewartson-type layers described in [121]. The thickness of the outermost layer, following the peak position of rms velocity, is in line with the expected thickness for Stewartson layers, as shown before. Further evidence of the layers being Stewartson layers is presented in Appendix A, where a horizontal cross-section within the bottom Ekman boundary layer reveals the action of the 'corner' region near $z/H = 0$ and $r/R = 1$ of typical dimension $Ek^{1/2} \times Ek^{1/2}$ (both scaled with cell height H) that can be quite important for the overall flux [121]. The inner part of the Stewartson layer is expected to be weaker than the outer part; it is visible in Fig. 7.3(b) as a smaller peak in u_z^{rms}, which is washed away by the turbulent bulk in the higher Ra cases. In line with that, the two-layer structure in u_ϕ, prominent at $Ra = 5.0 \times 10^{10}$, all but disappears at $Ra = 4.3 \times 10^{11}$. Where the two halves of the layers meet there is a strong radially inward flow that can be appreciated even better from the movies in Appendix A. These jet-like eruptions set the mean flow pattern in the bulk: at the lower Ra the jets are deflected to the right (positive u_ϕ) by the Coriolis acceleration; at the higher Ra the jets collide centrally and subsequently flow outward in the perpendicular directions. Note, however, that the mean flow in the bulk is coexisting with a fluctuating turbulent field (see Section 7.7).

The visualizations in Fig. 7.5 have some visual resemblance to the modes for convective onset in a cylinder [209]. However, at the current parameter values these onset modes are domain-filling (and not wall-localized) with azimuthal wavenumber $m = 1$ and leave out the prominent jets, leading us to conclude that what we observe are not onset modes. We currently cannot explain the structure of the sidewall circulation: its 'torsional' structure of the mean u_ϕ field (up–down antisymmetry) and its division into two halves. We are currently studying this in more detail with boundary-layer theory.

7.7. Contributions of bulk and sidewall circulation regions to the heat transfer

Given that the sidewall circulation contributes significantly to the overall heat transfer, it is of interest to compare the 'strength' of the sidewall circulation to the turbulence intensity. To this end we take the absolute value of u_z in the orientation-compensated mean field at $z/H = 0.5$ (Fig. 7.5) and average it over the sidewall-circulation region $1 - \delta_{u_{z,\min}^{\mathrm{rms}}}/R < r/R < 1$ as a measure of the strength of the sidewall circulation. The bulk turbulence intensity is measured by u_z^{rms} averaged over $0 < r/R < 1 - \delta_{u_{z,\min}^{\mathrm{rms}}}/R$ at the corresponding height. The resulting sidewall-circulation-to-bulk-turbulence ratio denoted by Φ is $\Phi \approx 3$ at the lowest $Ra = 5.0 \times 10^{10}$; $\Phi \approx 1.5$ at $Ra = 7.0 \times 10^{10}$; it attains its minimal value $\Phi \approx 0.5$ at $Ra = 1.4 \times 10^{11}$; then at the two highest Ra increases again to $\Phi \approx 0.9$. An interpretation of this ratio is that its value indicates which flow feature (turbulence or sidewall circulation) is expected to be most prominent in an instantaneous snapshot of the flow: when $\Phi \gg 1$ it will mostly display the sidewall-circulation signature, when $\Phi \ll 1$ we expect a foremost turbulent field. From these numbers we conclude that indeed the sidewall circulation remains significant throughout the Ra range considered here; for the lowest Ra it is probably the dominant dynamical feature, stronger than the bulk turbulence, while at $Ra = 1.4 \times 10^{11}$ the bulk turbulence is stronger than the sidewall circulation. This can also be appreciated from the movies in Appendix A.

The distinction between bulk and sidewall-circulation regions is also easily made in the heat transfer. We have computed the bulk (near-wall) Nusselt number Nu_{bulk} (Nu_{wall}) by averaging $\mathcal{F}_z$ over $0 < r/R < 1 - \delta_{u_{z,\min}^{\mathrm{rms}}}/R$ ($1 - \delta_{u_{z,\min}^{\mathrm{rms}}}/R < r/R < 1$) at $z/H = 0.5$. These results, together with the default full-area Nusselt number Nu_{full}, are plotted in Fig. 7.6. Overall, we want to mention first that Nu_{full} (filled red circles) nicely coincides with the experimental results, giving us trust in the current cylindrical DNS. At the two lowest Ra considered here, part of the CTC flow regime, it can be seen that the bulk is convecting less heat than the horizontally periodic layer. We observe in the movies in Appendix A that a dominant horizontal flow induced by the jets truly dominates the bulk flow, which we expect to distort and reduce the vertical natural convection. On the other hand, when considering Nu_{bulk} at $Ra \geq 1.4 \times 10^{11}$ we can see a very satisfactory quantitative agreement with the results of the DNS on the horizontally periodic domain. This is a strong result that indicates that — for the plumes and geostrophic-turbulence flow regimes at least — the sidewall circulation is indeed only affecting the turbulent heat flux in a confined near-wall region, while the bulk displays unaffected dynamics at least with regard to the heat transfer. Obviously, Nu_{wall} displays the opposite trend from Nu_{bulk} where it reaches values higher than Nu_{full} as a clear sign that the near-wall region contributes more than its share in area to the overall heat flux. If Ra would be increased beyond 4.3×10^{11}, we expect the sidewall circulation to disappear once the transition to rotation-affected flow takes place. Then the three quantities Nu_{full}, Nu_{bulk} and Nu_{wall} should

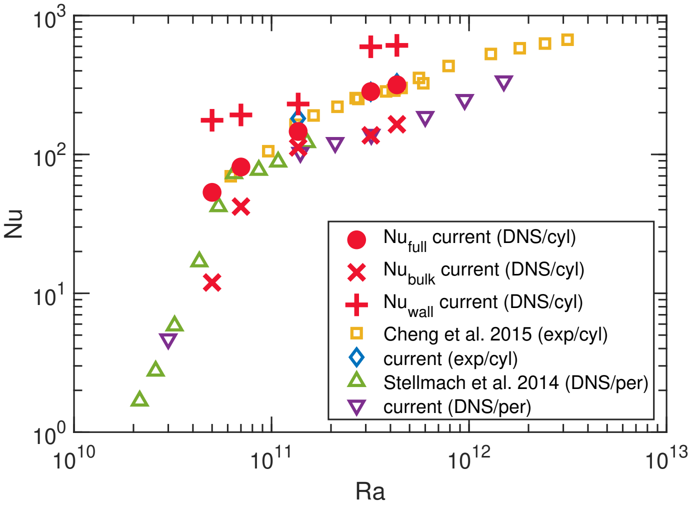

Figure 7.6.: *Nusselt number results from the current simulations. Included are* Nu_{full} *for heat flux averaged over the entire cylinder cross-section, as well as* Nu_{bulk} *and* Nu_{wall} *representing the heat flux averaged over bulk and near-wall regions, respectively. The other symbols are repeated from Fig. 7.1.*

be closer together.

7.8. Experimental evidence for existence of the sidewall circulation

The sidewall temperature probes provide evidence for the existence of the sidewall circulation in the experiment. In Fig. 7.7(a) we plot part of the time trace of temperature measurements of the sidewall probes; two pairs of probes on opposite sides of the cylinder at five different heights. The displayed part covers 1000 convective time units, i.e. about five hours out of a total segment of 24 hours measured in this experiment. Each trace displays a somewhat erratic but clearly evident oscillation around a mean value. This mean value is a function of height, a well-known result of the mean temperature gradient that develops in turbulent rotating convection [31]. There is a half-period phase difference between signals from opposite sides of the cylinder wall (darker and lighter shades of the same color), while signals on the same side but at different heights are at the same phase (darker shades align in phase, as do the lighter shades). These measurements are fully in line with the presence of a sidewall circulation as described in the earlier sections. Since we only have two thermistors per height we cannot determine the direction of the precession.

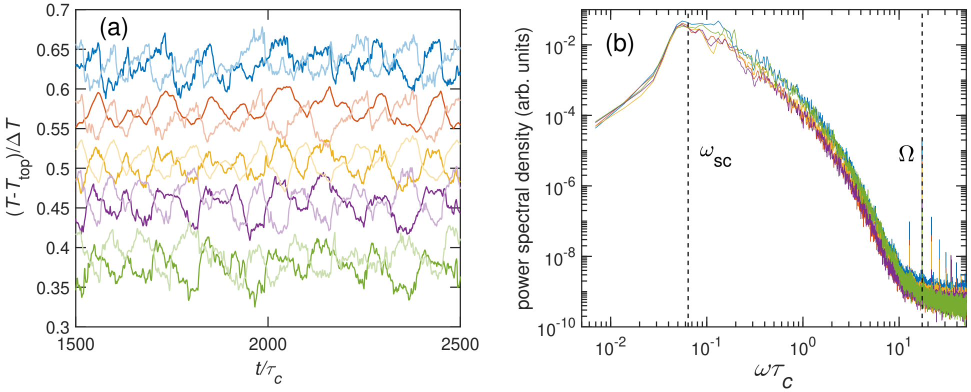

Figure 7.7.: *(a) Partial time traces (in convective time units) of sidewall temperature probes at (from top to bottom)* $z/H = 0.1, 0.3, 0.5, 0.7$ *and* 0.9*. Each pair of lines with the same color but different shading displays the signals from sensors on opposite sides of the cylinder but at the same height. These measurements are taken at* $Ra = 4.3 \times 10^{11}$*. (b) Frequency spectra of the sidewall temperature time traces in panel (a). Only one sensor per height is included for clarity. The vertical dashed lines indicate reference angular frequencies:* ω_{sc} *from the corresponding DNS (Fig. 7.4) and* Ω*, the rotation rate of the setup.*

But it is possible to calculate frequency spectra of the temperature time traces. These are reported in Fig. 7.7(b), where we only include one spectrum per vertical position for clarity; the others are similar. The shape of the spectrum is independent of height. The precession rate ω_{sc} of the sidewall circulation as inferred from the corresponding DNS is indicated with a vertical dashed line. It coincides satisfactorily with the peak of the spectra. This shows that the precession period of the sidewall circulation is the largest active time scale in this flow. We can compute similar spectra from the DNS for reference; we do not show them here given that the shorter elapsed time (only a few hundreds of τ_c) leads to inferior frequency resolution, but the peak is found at the expected position. The spectra of the two other experimental cases (shown in Appendix A) display similar results; the experiment at $Ra = 1.4 \times 10^{11}$ has a sidewall-circulation peak that is lower, in line with the observed lower intensity of the sidewall circulation in that case (Section 7.7).

7.9. Conclusions

In this combined numerical–experimental investigation of rapidly rotating turbulent convection in a cylindrical cell we have found a prominent sidewall circulation that provides a significant contribution to the overall heat transfer. It consists of a two-layer, two-halves structure with upward flow near the sidewall on one side and downward flow on the opposite side, while the azimuthal velocity displays a division into two radially separated bands with opposite direction of motion and a vertical torsional structure (antisymmetry with respect to the horizontal midplane). Jets consisting of intermittent bursts are ejected into the bulk from the locations where the two halves meet. This entire arrangement drifts slowly in the anticyclonic direction on timescales several orders of magnitude larger than the rotation period of the cell.

The sidewall circulation described here has similarities to the boundary zonal flow (BZF) reported by [55], but we also find remarkable differences, e.g., the two-halves structure. We expect that most of the differences occur because of different methods of analysis. In particular the use of azimuthal averaging in [55] obscures a lot of the important properties of the sidewall circulation that we report here, due to the approximate antisymmetry of the two halves. Additionally, it is entirely possible that the differences in the values of the governing parameters are responsible for the observed differences, given that our Prandtl number is considerably larger ($Pr = 5.2$ versus 0.8 in [55]), our Rayleigh numbers are about two orders of magnitude larger, and our Ekman number is more than one order of magnitude smaller than the smallest Ek considered in [55]. Finally, the cylinder aspect ratio (here $\Gamma = 1/5$, while [55] apply $\Gamma = 1/2$) is different. There is certainly need for further reconciliation of these results, by investigating the dependence of properties of the sidewall circulation or BZF on the parameter values.

This sidewall circulation contributes significantly to the overall heat transfer in a cylinder. Some care must be taken in the interpretation of these results as far as a comparison to horizontally periodic simulation domains or geophysically and astrophysically relevant geometries is intended (e.g. [55, 71, 76]). However, our current findings hint at the sidewall circulation being a Stewartson-type boundary layer, which identifies clear avenues of reducing its relative importance: either lower Ek to reduce its radial size, or increase the lateral dimensions of the convection cell. Nevertheless, for high enough Rayleigh number, the heat transfer properties of the bulk flow are clearly in line with those of simulated flows in a laterally periodic domain. Hence we expect the bulk flow to be unaffected by the sidewall. Experiments using stereoscopic particle image velocimetry in TROCONVEX are in preparation; with these measurements we will perform a more in-depth comparison of flow statistics between bulk and sidewall regions.

The influence of lateral confinement on rotating flow systems should never be underestimated. In this chapter we have identified a sidewall circulation that exists only due to the presence of a sidewall. Furthermore, we have carried out some further (preliminary) simulations, both in a square cuboid domain (courtesy of Paolo Cifani, University of Groningen) and in a cylinder domain with stress-free sidewalls, that have also revealed the existence of a sidewall circulation analogous to the one described in this chapter, but with differences in details of the structure. The combination of Ekman boundary layers and lateral confinement appears to be enough to set up a sidewall circulation. Yet, notwithstanding the prominence of the sidewall circulation, we have shown that a turbulent flow that is statistically unaffected by the sidewall circulation can still develop in the bulk of confined domains. Therefore, experiments, despite their inherent confinement, are still very valuable: they can provide bulk turbulence unaffected by sidewall effects at more extreme parameter values than can be achieved in numerical simulations, getting closer to the natural systems in geophysics and astrophysics that we want to understand and describe.

Chapter 8

Concluding remarks

In this thesis, we have discussed direct numerical simulations of rotating Rayleigh–Bénard convection driven by strong thermal forcing and subject to rapid rotation. The main approach used a domain with periodic lateral boundaries, vertically bounded by walls with no-slip boundary conditions and constant-temperature boundary conditions, $T(z = 0) = 1$ and $T(z = 1) = 0$. Some additional simulations on a confined cylindrical domain were considered for comparison with results from the periodic simulations as well as results from the laboratory experiment TROCONVEX in our group. In this chapter, we first summarise our main conclusions, and then we discuss possible research directions for the future.

8.1. Conclusions

Rotating Rayleigh–Bénard convection on a horizontally periodic domain is simulated over a range of parameter values (Pr, Ek and Ra) that jointly resolves over three decades of supercriticality Ra/Ra_c. We identified several different flow regimes: cells, convective Taylor columns, plumes, large-scale vortices (LSVs) and rotation-affected convection. These regimes, also found in previous studies, have been investigated in this thesis from various perspectives, with the intention to further deepen our knowledge and understanding of these phenomena. Below, we present our main findings.

Direct calculation of the magnitude of the governing forces of RRBC revealed that the primary force balance in the geostrophic regime (cells, columns, plumes and large-scale vortices) is indeed geostrophy. In this balance both the Coriolis force and the pressure-gradient are the main forces in the flow. We find that at higher supercriticality, in the rotation-affected regime, this rotational constraint is lost, at $Ra/Ra_c \approx 60$ for $Pr = 0.1$, due to a steep drop of the relative importance of Coriolis forces accompanied by an increase of the inertial forces.

The geostrophic flows are however *ageostrophic* at higher order, caused by the contribution of other forces. For cells and columns, ageostrophy is due to viscosity and buoyancy. Inertia is smaller, but steeply increases with Ra/Ra_c. For plumes, inertial forces enter the subdominant balance, along with viscous and buoyancy forces. For LSVs, inertia becomes the main source of ageostrophy. In rotation-affected convection, inertial and pressure-gradient forces constitute the dominant force balance. Here, the subdominant balance is formed by the remaining forces: Coriolis, viscous and buoyancy forces.

In the geostrophic regime, the near-wall flow is also geostrophic at leading order. This balance is lost towards the rotation-affected regime. As in the bulk, this is due to a rapid decrease of the relevance of the Coriolis force with supercriticality, and increased inertial forces. Remarkably, this occurs at a similar supercriticality as in the bulk (i.e. $Ra/Ra_c \approx 60$ at $Pr = 0.1$). In the geostrophic regime, the thickness δ_u of the kinetic boundary layer scales as $Ek^{1/2}$, as expected for linear Ekman boundary layers [107]. In the rotation-affected regime, the loss of rotational constraint in the kinetic boundary layer is reflected as deviations from the $Ek^{1/2}$ scaling. In that regime, the thermal boundary layer thickness δ_θ displays a tendency towards the scaling $\delta_\theta = 1/(2Nu)$ for non-rotating convection.

Close to the walls, viscous and inertial forces are about one order of magnitude larger than in the bulk. As a result, the ageostrophic component of the near-wall flow is about one order of magnitude larger than in the bulk. Buoyancy does not increase as much as viscous and inertial forces. Therefore, for cells, ageostrophy is caused by viscous forces alone, and, for columns and plumes, it is caused by inertia and viscosity; i.e. there is no participation of buoyancy, in contrast with the bulk. For LSVs and rotation-affected convection, bulk and near-wall subdominant balances are similar.

These dynamical balances lead to specific flow phenomenologies in each RRBC regime. We established connections between them and their corresponding temperature signature. At $Pr \approx 5$, the convective heat transfer Nu scales as $(Ra/Ra_c)^{2.7}$ in the cellular and columnar regimes, and as $(Ra/Ra_c)^{0.4}$ in the plumes regime. For plumes at $Pr = 100$ the heat transport is less efficient: $Nu \sim (Ra/Ra_c)^{0.2}$. For LSVs, at $Pr \approx 5$ and $Pr = 0.1$, the Nu scaling is in accordance with $Nu_* \sim Ra_*^{0.55}$ [36], where $Nu_* = NuEk/Pr$ and $Ra_* = RaEk^3Nu/Pr^2$. For rotation-affected convection (observed at $Pr = 0.1$), the heat transport scaling is shallower than for LSVs, as it approaches the non-rotating scaling $Ra^{1/5}$ [115, 182–184].

The relative thickness of the kinetic and thermal boundary layers affects the near-wall temperature distribution. When the thermal boundary layer is nested within the kinetic boundary layer, localised flows emerging from the bottom (top) kinetic boundary layer are matched by localisation of hot (cold) fluid in this region. This is observed for plumes at $Pr = 100$, LSVs at $Pr \approx 5$, and rotation-affected convection at $Pr = 0.1$. We hypothesise, nonetheless, that this correspondence becomes weaker at $\delta_u \gg \delta_\theta$. The rationale is that such situation would necessarily imply a state of vigorous convection (so that δ_θ is small) subject to slow rotation (so that δ_u is large), where the active pumping of fluid from the kinetic boundary layer is rather weak, if at all. Conversely, when $\delta_u < \delta_\theta$, hot (cold) fluid is distributed over large portions of the horizontal domain within the bottom (top) thermal boundary layer. This is observed for cells, columns and plumes at $Pr \approx 5$, and LSVs at $Pr = 0.1$. We thus hypothesise that in the case when $\delta_u \ll \delta_\theta$, Ekman pumping leads to the convective motion of fluid parcels with very low thermal contrast within the thermal boundary layer.

Localised Ekman pumping from the boundary layers postpones the occurrence of upscale energy transfer, and thus LSVs, to significantly higher rotation rates than for stress-free boundaries (at the same supercriticality). Namely, they require stronger rotational constraint to be diverted into upscale transfer to LSVs. These near-wall flows from the kinetic boundary layer are sheared apart by large horizontal velocities from the LSVs. Their kinetic energy is then available to be transferred towards the large scales to feed the vortex.

In confined RRBC, a sidewall circulation develops. This flow contributes significantly to the overall bottom-to-top heat transfer. It shares resemblance with Stewartson-type boundary layers in that its influence may be reduced by either lowering Ek, so that its size is smaller, or by increasing the cylinder radius. The sidewall circulation ejects fluid into the bulk. At larger Ra, where this effect is smaller, the heat transport evaluated exclusively in the bulk (i.e. excluding the sidewall circulation) is shown to match that of laterally periodic domains. Thus, turbulent flows that are statistically unaffected by the sidewall circulation can still develop in the bulk of confined domains, such as in laboratory experiments.

8.2. Outlook

Several interesting directions for further research emanate from the results presented in this thesis.

Our analysis of the force balances in rotating Rayleigh–Bénard convection, in itself, provides extensive characterisation of the observed flow regimes. The forces are computed at each computational grid cell, thus providing a real-space local measure of their magnitude. It would be interesting perform a scale-wise analysis, i.e. in Fourier space, of the force balances to elucidate the interplay amongst forces at different spatial scales. For example, in our real-space analysis we noticed the increasing importance of inertial forces. Through the proposed analysis, one could determine the scale, or range of spatial scales, at which this occurs. This Fourier-based approach could also be used to evaluate the existence of dominant physical balances over specific ranges of spatial scales. This study would then provide useful information on the scaling ranges of convectively driven rotating turbulence.

The direct calculation of the (local) Rossby number Ro_ℓ as the ratio of inertial to Coriolis forces proved to be a good indicator of the transition from rotation-dominated to rotation-affected convection. Given $Ro_\ell = U/2\Omega\ell$, one could separately characterise this transition in relation to the local characteristic velocity scale U (as we did using the RMS of horizontal and vertical velocities), but also in terms of the local characteristic length scale ℓ. Possible connections can then be established with the study proposed above, as to how the increased contribution of certain forces at a given spatial scale can influence the characteristic length scale in the flow. Furthermore, it would be possible to evaluate how this scale may depend on and/or relate to the thickness of the kinetic or thermal boundary layers.

A crucial next step in the field of convectively driven rotating turbulence is the exploration of LSV growth in laboratory experiments. In this setting, RRBC can be studied at more extreme parameter values, and over a longer time span, than can be achieved in numerical simulations. As a first step, the simulations could help to further quantify the influence of the horizontal jets from the sidewall circulation into the bulk. This would help to estimate the parameter settings (Ek, Ra, Γ) at which LSV growth is feasible. The establishment of a turbulent flow that is statistically unaffected by the sidewall circulation would then provide results that can be compared with those from unconfined simulations (i.e. horizontally periodic). The latter geometry turns out to be highly relevant to planetary settings, where the horizontal dimension is much larger than the vertical.

In this thesis, we employed a scale-by-scale energy transfer analysis to quantify the interactions amongst the multi-scale structures in the flow (Chapter 6). We found that deep insight into the boundary layer dynamics can be gained by taking into account the height-dependency of the energy transfer function. We promote this analysis not only for rotating Rayleigh–Bénard convection bounded by no-slip walls but also in the field of turbulence in general.

Finally, we encourage the implementation of the current analyses in spherical shell geometries. In particular, the investigation of LSV formation in these geometries would allow further understanding of large-scale flow organization in geophysical and astrophysical systems.

Appendix A

Additional analyses of the sidewall circulation

Azimuthally averaged profiles of azimuthal velocity

In the main text we have argued that azimuthal averaging, used frequently in the analysis by [55], provides a different and complementary view of the structure and size of the sidewall circulation. In visualizations of u_ϕ the two halves are almost identical but of opposite sign. Azimuthally averaged profiles of u_ϕ are the net result of these asymmetries and peaks or zero crossings are unrelated to the actual flow structure. We plot radial profiles of the azimuthally averaged $\langle u_\phi \rangle$ at $z/H = 0.5$ in Fig. A.1. This figure can be compared to Fig. 3(b) of [55], that qualitatively resembles our highest-Ra case. However, the curves for the other Ra values considered here display significantly different radial profiles, with a considerably and non-monotonically reduced peak near the sidewall and the development of a net cyclonic part for $0 < r \lesssim 0.75$.

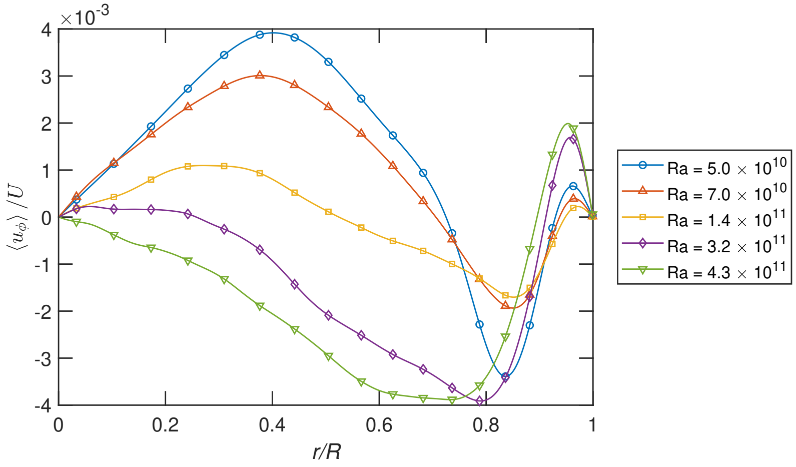

Figure A.1.: *Radial profiles of azimuthally averaged* $\langle u_\phi \rangle$ *at* $z/H = 0.5$.

Additional orientation-compensated mean velocity fields

To illustrate the flow field inside the bottom Ekman boundary layer, we present in Figure A.2 orientation-compensated mean velocity fields in a horizontal cross-section at $z/H = 6 \times 10^{-4}$. The Rayleigh number is 5.0×10^{10}. Of particular note is the u_z snapshot, where a thin layer of opposite flow direction is formed at the sidewall (i.e. the dark red area in the zoomed-in view), a known feature of Stewartson boundary layers [121]. The radial (u_r) and azimuthal (u_ϕ) velocity fields need to adapt too; the radial and azimuthal flow inside the Ekman boundary layer is more intense than outside that layer, at higher z.

In Figure A.3 we provide orientation-compensated mean cross-sections displaying the three velocity components u_z, u_r and u_ϕ at heights $z/H = 0.25$, 0.5 and 0.75 for the three simulations for which these plots are not included in Chapter 7. We want to emphasize the case $Ra = 1.4 \times 10^{11}$, where the sidewall circulation is weakest, as can be appreciated from the relatively small velocity values and the erratic structure in the interior where no strong mean flow is established.

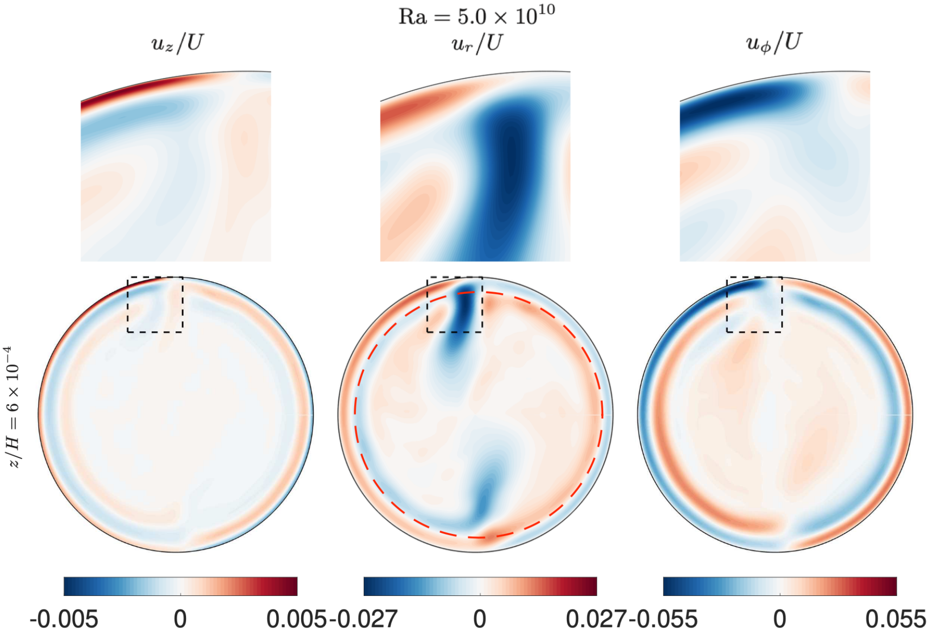

Figure A.2.: *Orientation-compensated mean velocity fields in horizontal cross-sections at height $z/H = 6 \times 10^{-4}$ for Rayleigh number $Ra = 5.0 \times 10^{10}$. The vertical (u_z), radial (u_r) and azimuthal (u_ϕ) velocity components are shown. The top row is a zoomed-in view of the area demarcated with the dashed line in the bottom row.*

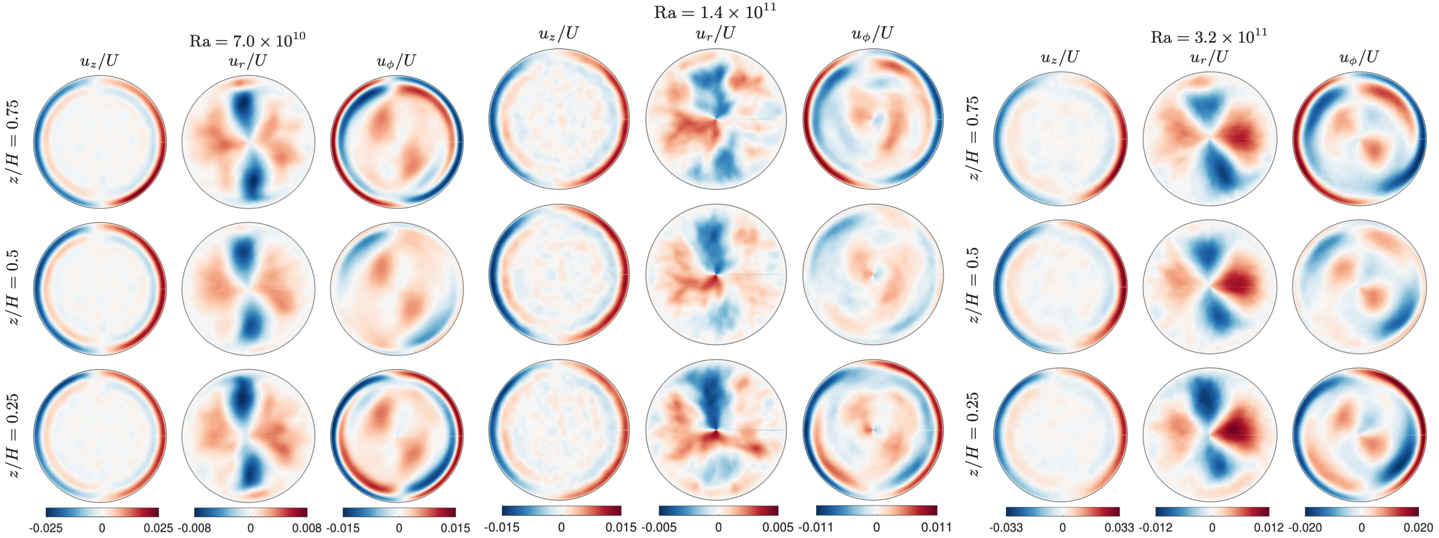

Figure A.3.: *Orientation-compensated mean velocity fields in horizontal cross-sections at heights* $z/H = 0.25$, 0.5 *and* 0.75 *for the remaining three Rayleigh numbers* 7.0×10^{10} *(top left),* 1.4×10^{11} *(top right) and* 3.2×10^{11} *(bottom). The vertical* (u_z), *radial* (u_r) *and azimuthal* (u_ϕ) *velocity components are shown.*

Additional spectra from the experiment

In Figure A.4 we provide additional sidewall temperature frequency spectra for the experiments at $Ra = 1.4 \times 10^{11}$ and 3.2×10^{11}. In both cases the spectra are reasonably independent of height (all curves overlap satisfactorily) and there is a local peak close to the azimuthal drift frequency ω_{sc} of the sidewall circulation as found in DNS. Note that at $Ra = 1.4 \times 10^{11}$ this peak is lower; the sidewall circulation is weakest there.

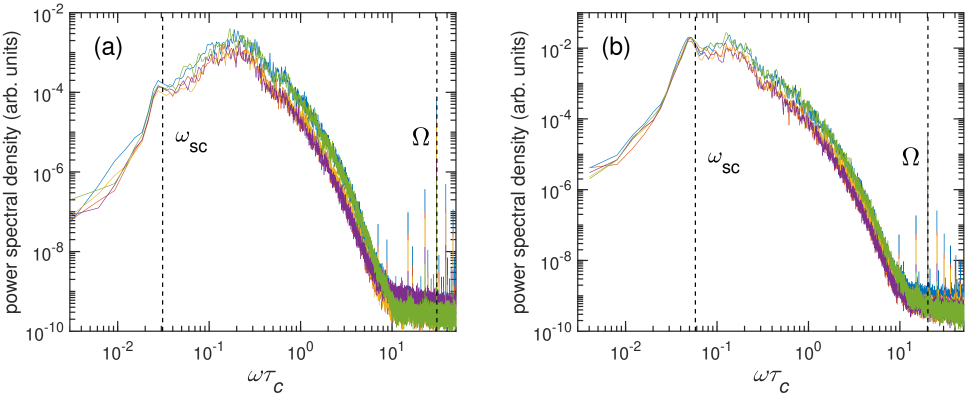

Figure A.4.: *Frequency spectra of the sidewall temperature time traces at (a)* $Ra = 1.4 \times 10^{11}$ *and (b)* $Ra = 3.2 \times 10^{11}$*. Only one sensor per height is included for clarity. The vertical dashed lines indicate reference angular frequencies:* ω_{sc} *from the corresponding DNS (see Fig. 7.4) and* Ω*, the rotation rate of the setup. The colors are as in Fig. 7.7.*

Bibliography

[1] H. Bénard. Les tourbillons cellulaires dans une nappe liquide. *Rev. Gén. Sci. Pure Appl.*, 11:1261–1271, 1900. (Cited on page 1.)

[2] H. Bénard. Les tourbillons cellulaires dans une nappe liquide. *Rev. Gén. Sci. Pure Appl.*, 11:1309–1328, 1900. (Cited on page 1.)

[3] H. Bénard. Les tourbillons cellulaires dans une nappe liquide transportant de la chaleur par convection en régime permanent. *Ann. Chim. Phys.*, 23:62–144, 1901. (Cited on page 1.)

[4] Lord Rayleigh. On convection currents in a horizontal layer of fluid, when the higher temperature is on the under side. *Phil. Mag.*, 32(192):529–546, 1916. (Cited on page 1.)

[5] S. Chandrasekhar. The instability of a layer of fluid heated below and subject to Coriolis forces. *Proc. R. Soc. Lond. A*, 217(1130):306–327, 1953. (Cited on page 1.)

[6] Y. Nakagawa and P. Frenzen. A theoretical and experimental study of cellular convection in rotating fluids. *Tellus*, 7(1):2–21, 1955. (Cited on page 1.)

[7] H. T. Rossby. A study of Bénard convection with and without rotation. *J. Fluid Mech.*, 36(2):309–335, 1969. (Cited on pages 1, 2, and 82.)

[8] P. Cardin and P. Olson. Chaotic thermal convection in a rapidly rotating spherical shell: consequences for flow in the outer core. *Phys. Earth Planet. Inter.*, 82(3-4):235–259, 1994. (Cited on pages 1 and 38.)

[9] G. A. Glatzmaier, R. S. Coe, L. Hongre, and P. H. Roberts. The role of the Earth's mantle in controlling the frequency of geomagnetic reversals. *Nature*, 401(6756):885–890, 1999. (Cited on page 1.)

[10] C. A. Jones. Convection–driven geodynamo models. *Phil. Trans. R. Soc. Lond. A*, 358(1768):873–897, 2000. (Cited on page 1.)

[11] G. R. Sarson. Reversal models from dynamo calculations. *Phil. Trans. R. Soc. Lond. A*, 358(1768):921–942, 2000. (Cited on page 1.)

[12] G. Budéus, B. Cisewski, S. Ronski, D. Dietrich, and M. Weitere. Structure and effects of a long lived vortex in the Greenland Sea. *Geophys. Res. Lett*, 31(5), 2004. (Cited on page 2.)

[13] J.-C. Gascard, A. J. Watson, M.-J. Messias, K. A. Olsson, T. Johannessen, and K. Simonsen. Long-lived vortices as a mode of deep ventilation in the Greenland Sea. *Nature*, 416(6880):525–527, 2002. (Cited on page 2.)

[14] J. Marshall and F. Schott. Open-ocean convection: Observations, theory, and models. *Rev. Geophys*, 37(1):1–64, 1999. (Cited on page 2.)

[15] P. Wadhams, J. Holfort, E. Hansen, and J. P. Wilkinson. A deep convective chimney in the winter Greenland Sea. *Geophys. Res. Lett.*, 29(10):76–1, 2002. (Cited on page 2.)

[16] G. Hadley. Concerning the cause of the general trade-winds. *Phil. Trans. R. Soc. Lond.*, 39(437):58–62, 1735. (Cited on page 2.)

[17] F. H. Busse. Convection driven zonal flows and vortices in the major planets. *Chaos*, 4(2):123–134, 1994. (Cited on page 2.)

[18] F. H. Busse and C. R. Carrigan. Laboratory simulation of thermal convection in rotating planets and stars. *Science*, 191(4222):81–83, 1976. (Cited on page 2.)

[19] M. Heimpel and J. M. Aurnou. Turbulent convection in rapidly rotating spherical shells: A model for equatorial and high latitude jets on Jupiter and Saturn. *Icarus*, 187(2):540–557, 2007. (Cited on page 2.)

[20] A. P. Ingersoll. Atmospheric dynamics of the outer planets. *Science*, 248(4953):308–315, 1990. (Cited on page 2.)

[21] C. C. Porco, R. A. West, A. McEwen, A. D. Del Genio, A. P. Ingersoll, P. Thomas, S. Squyres, L. Dones, C. D. Murray, T. V. Johnson, et al. Cassini imaging of Jupiter's atmosphere, satellites, and rings. *Science*, 299(5612):1541–1547, 2003. (Cited on page 2.)

[22] A. Sanchez-Lavega, J. F. Rojas, and P. V. Sada. Saturn's zonal winds at cloud level. *Icarus*, 147(2):405–420, 2000. (Cited on page 2.)

[23] M. S. Miesch. The coupling of solar convection and rotation. *Solar Physics*, 192:59–89, 2000. (Cited on page 2.)

[24] F. Cattaneo, T. Emonet, and N. Weiss. On the interaction between convection and magnetic fields. *Astrophys. J.*, 588(2):1183, 2003. (Cited on page 2.)

[25] S. A. Balbus, J. Bonart, H. N. Latter, and N. O. Weiss. Differential rotation and convection in the Sun. *Mon. Not. R. Astron. Soc.*, 400(1):176–182, 2009. (Cited on page 2.)

[26] M. G. Dunn. Convective heat transfer and aerodynamics in axial flow turbines. *J. Turbomach.*, 78538:V004T06A001, 2001. (Cited on page 2.)

[27] J. P. Johnston. Effects of system rotation on turbulence structure: a review relevant to turbomachinery flows. *Int. J. Rot. Mach.*, 4, 1998. (Cited on page 2.)

[28] H. van Santen, C. R. Kleijn, and H. E. A. van den Akker. On turbulent flows in cold-wall CVD reactors. *J. Cryst. Growth*, 212(1-2):299–310, 2000. (Cited on page 2.)

[29] R. van Wissen, M. Golombok, and J. J. H. Brouwers. Separation of carbon dioxide and methane in continuous countercurrent gas centrifuges. *Chem. Eng. Sci*, 60(16):4397–4407, 2005. (Cited on page 2.)

[30] R. van Wissen, M. Golombok, and J. J. H. Brouwers. Gas centrifugation with wall condensation. *AIChE J.*, 52(3):1271–1274, 2006. (Cited on page 2.)

[31] K. Julien, S. Legg, J. McWilliams, and J. Werne. Rapidly rotating turbulent Rayleigh–Bénard convection. *J. Fluid Mech.*, 322:243–273, 1996. (Cited on pages 2, 10, 50, 53, 82, and 92.)

[32] R. P. J. Kunnen, H. J. H. Clercx, and B. J. Geurts. Heat flux intensification by vortical flow localization in rotating convection. *Phys. Rev. E*, 74(5):056306, 2006. (Cited on pages 2, 50, and 82.)

[33] M. Sprague, K. Julien, E. Knobloch, and J. Werne. Numerical simulation of an asymptotically reduced system for rotationally constrained convection. *J. Fluid Mech.*, 551:141, 2006. (Cited on pages 2, 3, 33, 34, 37, 38, 47, 82, and 85.)

[34] R. P. J. Kunnen, H. J. H. Clercx, and B. J. Geurts. Enhanced vertical inhomogeneity in turbulent rotating convection. *Phys. Rev. Lett.*, 101(17):174501, 2008. (Cited on pages 2 and 51.)

[35] E. M. King, S. Stellmach, J. Noir, U. Hansen, and J. M. Aurnou. Boundary layer control of rotating convection systems. *Nature*, 457(7227):301–304, 2009. (Cited on pages 2 and 82.)

[36] S. Schmitz and A. Tilgner. Heat transport in rotating convection without Ekman layers. *Phys. Rev. E*, 80(1):015305, 2009. (Cited on pages 2, 54, 55, 56, 68, and 98.)

[37] R. J. A. M. Stevens, H. J. H. Clercx, and D. Lohse. Optimal Prandtl number for heat transfer in rotating Rayleigh–Bénard convection. *New J. Phys.*, 12(7):075005, 2010. (Cited on page 2.)

[38] R. P. J. Kunnen, B. J. Geurts, and H. J. H. Clercx. Experimental and numerical investigation of turbulent convection in a rotating cylinder. *J. Fluid Mech.*, 642:445–476, 2010. (Cited on pages 2, 51, 73, 82, 86, and 87.)

[39] R. J. A. M. Stevens, H. J. H. Clercx, and D. Lohse. Effect of plumes on measuring the large scale circulation in turbulent Rayleigh–Bénard convection. *Phys. Fluids*, 23(9):095110, 2011. (Cited on pages 2 and 70.)

[40] E. M. King and J. M. Aurnou. Thermal evidence for Taylor columns in turbulent rotating Rayleigh–Bénard convection. *Phys. Rev. E*, 85(1):016313, 2012. (Cited on pages 2, 3, and 34.)

[41] K. Julien, A. M. Rubio, I. Grooms, and E. Knobloch. Statistical and physical balances in low Rossby number Rayleigh–Bénard convection. *Geophys. Astrophys. Fluid Dyn.*, 106(4-5):392–428, 2012. (Cited on pages 2, 3, 4, 33, 34, 35, 37, 38, 41, 47, 49, 50, 51, 53, 54, 55, 56, 57, 64, 70, 71, 72, 73, 77, 82, 84, 85, and 86.)

[42] E. M. King, S. Stellmach, and B. Buffett. Scaling behaviour in Rayleigh–Bénard convection with and without rotation. *J. Fluid Mech.*, 717:449–471, 2013. (Cited on pages 2, 35, 39, 40, and 59.)

[43] R. J. A. M. Stevens, H. J. H. Clercx, and D. Lohse. Heat transport and flow structure in rotating Rayleigh–Bénard convection. *Eur. J. Mech. B Fluids*, 40:41–49, 2013. (Cited on page 2.)

[44] C. Guervilly, D. W. Hughes, and C. A. Jones. Large-scale vortices in rapidly rotating Rayleigh–Bénard convection. *J. Fluid Mech.*, 758:407–435, 2014. (Cited on pages 2, 3, 4, 34, 54, 70, 71, and 82.)

[45] S. Stellmach, M. Lischper, K. Julien, G. Vasil, J. S. Cheng, A. Ribeiro, E. M. King, and J. M. Aurnou. Approaching the asymptotic regime of rapidly rotating convection: boundary layers versus interior dynamics. *Phys. Rev. Lett.*, 113(25):254501, 2014. (Cited on pages 2, 3, 4, 33, 34, 53, 69, 70, 73, 82, 83, 84, and 85.)

[46] B. Favier, L. J. Silvers, and M. R. E. Proctor. Inverse cascade and symmetry breaking in rapidly rotating Boussinesq convection. *Phys. Fluids*, 26(9):096605, 2014. (Cited on pages 2, 3, 4, 34, 70, 71, 72, 73, and 82.)

[47] S. Horn and O. Shishkina. Rotating non-Oberbeck–Boussinesq Rayleigh–Bénard convection in water. *Phys. Fluids*, 26(5):055111, 2014. (Cited on pages 2 and 82.)

[48] S. Horn and O. Shishkina. Toroidal and poloidal energy in rotating Rayleigh–Bénard convection. *J. Fluid Mech.*, 762:232–255, 2015. (Cited on page 2.)

[49] M. A. Calkins, K. Hale, K. Julien, D. Nieves, D. Driggs, and P. Marti. The asymptotic equivalence of fixed heat flux and fixed temperature thermal boundary conditions for rapidly rotating convection. *J. Fluid Mech.*, 784, 2015. (Cited on page 2.)

[50] R. P. J. Kunnen, R. Ostilla-Mónico, E. P. van der Poel, R. Verzicco, and D. Lohse. Transition to geostrophic convection: the role of the boundary conditions. *J. Fluid Mech.*, 799:413–432, 2016. (Cited on pages 2, 3, 4, 34, 49, 50, 53, 57, 61, 70, and 82.)

[51] M. Plumley, K. Julien, P. Marti, and S. Stellmach. The effects of Ekman pumping on quasi-geostrophic Rayleigh–Bénard convection. *J. Fluid Mech.*, 803:51–71, 2016. (Cited on pages 2, 3, 4, 33, 37, 47, 70, 71, 73, and 82.)

[52] K. M. J. Alards, R. P. J. Kunnen, R. J. A. M. Stevens, D. Lohse, F. Toschi, and H. J. H. Clercx. Sharp transitions in rotating turbulent convection: Lagrangian acceleration statistics reveal a second critical Rossby number. *Phys. Rev. Fluids*, 4(7):074601, 2019. (Cited on pages 2, 4, and 69.)

[53] X. M. de Wit, A. J. Aguirre Guzmán, M. Madonia, J. S. Cheng, H. J. H. Clercx, and R. P. J. Kunnen. Turbulent rotating convection confined in a slender cylinder: The sidewall circulation. *Phys. Rev. Fluids*, 5(2):023502, 2020. (Cited on pages 2, 4, and 81.)

[54] H.-Y. Lu, G.-Y. Ding, J.-Q. Shi, K.-Q. Xia, and J.-Q. Zhong. Heat transport scaling and transition in geostrophic rotating convection with varying aspect ratio. *arXiv preprint arXiv:2007.13279*, 2020. (Cited on page 2.)

[55] X. Zhang, D. P. M. Van Gils, S. Horn, M. Wedi, L. Zwirner, G. Ahlers, R. E. Ecke, S. Weiss, E. Bodenschatz, and O. Shishkina. Boundary zonal flow in rotating turbulent Rayleigh–Bénard convection. *Phys. Rev. Lett.*, 124(8):084505, 2020. (Cited on pages 2, 4, 83, 85, 86, 94, and 101.)

[56] B. Favier and E. Knobloch. Robust wall states in rapidly rotating Rayleigh–Bénard convection. *J. Fluid Mech.*, 895:R1, 2020. (Cited on pages 2 and 4.)

[57] Y. Yang, R. Verzicco, D. Lohse, and Richard J. A. M. Stevens. What rotation rate maximizes heat transport in rotating Rayleigh-Bénard convection with Prandtl number larger than one? *Phys. Rev. Fluids*, 5(5):053501, 2020. (Cited on page 2.)

[58] A. J. Aguirre Guzmán, M. Madonia, J. S. Cheng, R. Ostilla-Mónico, H. J. H. Clercx, and R. P. J. Kunnen. Competition between Ekman plumes and vortex condensates in rapidly rotating thermal convection. *Phys. Rev. Lett.*, 125(21):214501, 2020. (Cited on pages 2, 3, 34, and 69.)

[59] S. Maffei, M. J. Krouss, K. Julien, and M. A. Calkins. On the inverse cascade and flow speed scaling behavior in rapidly rotating Rayleigh–Bénard convection. *arXiv preprint arXiv:2003.01669*, 2020. (Cited on pages 2, 3, and 37.)

[60] B. M. Boubnov and G. S. Golitsyn. Experimental study of convective structures in rotating fluids. *J. Fluid Mech.*, 167:503–531, 1986. (Cited on page 2.)

[61] F. Zhong, R. E. Ecke, and V. Steinberg. Rotating Rayleigh–Bénard convection: asymmetric modes and vortex states. *J. Fluid Mech.*, 249:135–159, 1993. (Cited on page 2.)

[62] Y. Liu and R. E. Ecke. Heat transport scaling in turbulent Rayleigh–Bénard convection: effects of rotation and Prandtl number. *Phys. Rev. Lett.*, 79(12):2257, 1997. (Cited on page 2.)

[63] S. Sakai. The horizontal scale of rotating convection in the geostrophic regime. *J. Fluid Mech.*, 333:85–95, 1997. (Cited on pages 2, 3, 4, 34, 50, 61, and 69.)

[64] P. Vorobieff and R. E. Ecke. Turbulent rotating convection: an experimental study. *J. Fluid Mech.*, 458:191–218, 2002. (Cited on pages 2, 4, 51, 69, and 82.)

[65] Y. Liu and R. E. Ecke. Heat transport measurements in turbulent rotating Rayleigh–Bénard convection. *Phys. Rev. E*, 80(3):036314, 2009. (Cited on page 2.)

[66] J.-Q. Zhong and G. Ahlers. Heat transport and the large-scale circulation in rotating turbulent Rayleigh–Bénard convection. *J. Fluid Mech.*, 665:300, 2010. (Cited on page 2.)

[67] J. J. Niemela, S. Babuin, and K. R. Sreenivasan. Turbulent rotating convection at high Rayleigh and Taylor numbers. *J. Fluid Mech.*, 649:509, 2010. (Cited on page 2.)

[68] S. Weiss and G. Ahlers. Heat transport by turbulent rotating Rayleigh–Bénard convection and its dependence on the aspect ratio. *J. Fluid Mech.*, 684:407, 2011. (Cited on page 2.)

[69] R. P. J. Kunnen, Y. Corre, and H. J. H. Clercx. Vortex plume distribution in confined turbulent rotating convection. *EPL*, 104:54002, 2013. (Cited on pages 2, 51, 86, and 87.)

[70] R. E. Ecke and J. J. Niemela. Heat transport in the geostrophic regime of rotating Rayleigh–Bénard convection. *Phys. Rev. Lett.*, 113(11):114301, 2014. (Cited on pages 2 and 3.)

[71] J. S. Cheng, S. Stellmach, A. Ribeiro, A. Grannan, E. M. King, and J. M. Aurnou. Laboratory-numerical models of rapidly rotating convection in planetary cores. *Geophys. J. Int.*, 201(1):1–17, 2015. (Cited on pages 2, 39, 49, 72, 82, 83, 84, 85, and 94.)

[72] H. Rajaei, R. P. J. Kunnen, and H. J. H. Clercx. Exploring the geostrophic regime of rapidly rotating convection with experiments. *Phys. Fluids*, 29(4):045105, 2017. (Cited on pages 2, 3, 34, 51, and 52.)

[73] H. Rajaei, K. M. J. Alards, R. P. J. Kunnen, and H. J. H. Clercx. Velocity and acceleration statistics in rapidly rotating Rayleigh–Bénard convection. *J. Fluid Mech.*, 857:374–397, 2018. (Cited on pages 2, 51, and 82.)

[74] J. M. Aurnou, V. Bertin, A. M. Grannan, S. Horn, and T. Vogt. Rotating thermal convection in liquid gallium: Multi-modal flow, absent steady columns. *J. Fluid Mech.*, 846:846–876, 2018. (Cited on pages 2, 12, and 35.)

[75] E. H. Anders, C. M. Manduca, B. P. Brown, J. S. Oishi, and G. M. Vasil. Predicting the Rossby number in convective experiments. *Astrophys. J.*, 872(2):138, 2019. (Cited on page 2.)

[76] J. S. Cheng, M. Madonia, A. J. Aguirre Guzmán, and R. P. J. Kunnen. Laboratory exploration of heat transfer regimes in rapidly rotating turbulent convection. *Phys. Rev. Fluids*, 5(11):113501, 2020. (Cited on pages 2, 23, 30, 49, 50, 51, 53, 82, 84, and 94.)

[77] J.-Q. Shi, H.-Y. Lu, S.-S. Ding, and J.-Q. Zhong. Fine vortex structure and flow transition to the geostrophic regime in rotating Rayleigh-Bénard convection. *Phys. Rev. Fluids*, 5(1):011501, 2020. (Cited on pages 2, 3, 34, and 51.)

[78] E. M. King, S. Stellmach, and J. M. Aurnou. Heat transfer by rapidly rotating Rayleigh–Bénard convection. *J. Fluid Mech.*, 691:568–582, 2012. (Cited on pages 2 and 82.)

[79] S.-K. Chan. Investigation of turbulent convection under a rotational constraint. *J. Fluid Mech.*, 64(3):477–506, 1974. (Cited on page 2.)

[80] P. Constantin, C. Hallstrom, and V. Putkaradze. Heat transport in rotating convection. *Physica D*, 125(3-4):275–284, 1999. (Cited on page 2.)

[81] S. Chandrasekhar. *Hydrodynamic and Hydromagnetic Stability*. Oxford University Press, Oxford, 1961. (Cited on pages 2, 3, 9, 10, 12, and 33.)

[82] C. R. Doering and P. Constantin. On upper bounds for infinite Prandtl number convection with or without rotation. *J. Math. Phys.*, 42(2):784–795, 2001. (Cited on page 2.)

[83] N. K. Vitanov. Convective heat transport in a rotating fluid layer of infinite Prandtl number: Optimum fields and upper bounds on Nusselt number. *Phys. Rev. E*, 67(2):026322, 2003. (Cited on page 2.)

[84] D. Gubbins. The Rayleigh number for convection in the Earth's core. *Phys. Earth Planet. Inter.*, 128(1-4):3–12, 2001. (Cited on page 3.)

[85] J. M. Aurnou, S. Andreadis, L. Zhu, and P. Olson. Experiments on convection in Earth's core tangent cylinder. *Earth Planet. Sci. Lett.*, 212(1-2):119–134, 2003. (Cited on page 3.)

[86] G. Schubert and K. M. Soderlund. Planetary magnetic fields: observations and models. *Phys. Earth Planet. Inter.*, 187(3-4):92–108, 2011. (Cited on page 3.)

[87] J.-B. Manneville and P. Olson. Banded convection in rotating fluid spheres and the circulation of the Jovian atmosphere. *Icarus*, 122(2):242–250, 1996. (Cited on page 3.)

[88] R. P. J. Kunnen, H. J. H. Clercx, and B. J. Geurts. Vortex statistics in turbulent rotating convection. *Phys. Rev. E*, 82(3):036306, 2010. (Cited on pages 3, 4, 34, 69, and 73.)

[89] I. Grooms, K. Julien, J. B. Weiss, and E. Knobloch. Model of convective Taylor columns in rotating Rayleigh–Bénard convection. *Phys. Rev. Lett.*, 104(22):224501, 2010. (Cited on pages 3, 34, 41, 53, 61, and 85.)

[90] D. Noto, Y. Tasaka, T. Yanagisawa, and Y. Murai. Horizontal diffusive motion of columnar vortices in rotating Rayleigh–Benard convection. *J. Fluid Mech.*, 871:401–426, 2019. (Cited on pages 3 and 34.)

[91] K. L. Chong, J.-Q. Shi, G.-Y. Ding, S.-S. Ding, H.-Y. Lu, J.-Q. Zhong, and K.-Q. Xia. Vortices as Brownian particles in turbulent flows. *Sci. Adv.*, 6(34):eaaz1110, 2020. (Cited on pages 3 and 34.)

[92] A. M. Rubio, K. Julien, E. Knobloch, and J. B. Weiss. Upscale energy transfer in three-dimensional rapidly rotating turbulent convection. *Phys. Rev. Lett.*, 112(14):144501, 2014. (Cited on pages 3, 4, 34, 38, 70, 72, 73, and 75.)

[93] W. V. R. Malkus. The heat transport and spectrum of thermal turbulence. *Proc. R. Soc. Lond. A*, 225(1161):196–212, 1954. (Cited on page 3.)

[94] R. H. Kraichnan. Turbulent thermal convection at arbitrary Prandtl number. *Phys. Fluids*, 5(11):1374–1389, 1962. (Cited on page 3.)

[95] E. A. Spiegel. Convection in stars I. Basic Boussinesq convection. *Annu. Rev. Astron. Astrophys.*, 9(1):323–352, 1971. (Cited on page 3.)

[96] B. Castaing, G. Gunaratne, F. Heslot, L. Kadanoff, A. Libchaber, S. Thomae, X.-Z. Wu, S. Zaleski, and G. Zanetti. Scaling of hard thermal turbulence in Rayleigh-Bénard convection. *J. Fluid Mech.*, 204:1–30, 1989. (Cited on page 3.)

[97] V. W. Ekman. On the influence of the Earth's rotation on ocean-currents. *Arkiv. Matem. Astr. Fysik.*, 2:1–52, 1905. (Cited on pages 3, 4, and 15.)

[98] M. H. Rogers and G. N. Lance. The rotationally symmetric flow of a viscous fluid in the presence of an infinite rotating disk. *J. Fluid Mech.*, 7(4):617–631, 1960. (Cited on page 4.)

[99] P. P. Niiler and F. E. Bisshopp. On the influence of Coriolis force on onset of thermal convection. *J. Fluid Mech.*, 22(4):753–761, 1965. (Cited on page 4.)

[100] K. Julien, E. Knobloch, A. M. Rubio, and G. M. Vasil. Heat transport in low-Rossby-number Rayleigh–Bénard convection. *Phys. Rev. Lett.*, 109(25):254503, 2012. (Cited on pages 4 and 82.)

[101] O. Shishkina. Tenacious wall states in thermal convection in rapidly rotating containers. *J. Fluid Mech.*, 898, 2020. (Cited on page 4.)

[102] L. D. Landau and E. M. Lifshitz. *Fluid Mechanics.* Pergamon, London, 1959. (Cited on page 8.)

[103] A. Oberbeck. Über die Wärmeleitung der Flüssigkeiten bei Berücksichtigung der Strömungen infolge von Temperaturdifferenzen. *Annalen der Physik*, 243(6):271–292, 1879. (Cited on page 8.)

[104] J. V. Boussinesq. *Théorie analytique de la chaleur*, volume 2. Paris: Gauthier-Villars, 1903. (Cited on page 8.)

[105] X. Chavanne, F. Chilla, B. Chabaud, B. Castaing, and B. Hebral. Turbulent Rayleigh–Bénard convection in gaseous and liquid He. *Phys. Fluids*, 13(5):1300–1320, 2001. (Cited on page 9.)

[106] J. J. Niemela, L. Skrbek, K. R. Sreenivasan, and R. J. Donnelly. Turbulent convection at very high Rayleigh numbers. *Nature*, 404(6780):837–840, 2000. (Cited on page 9.)

[107] H. P. Greenspan. *The Theory of Rotating Fluids.* Cambridge University Press, 1968. (Cited on pages 9, 17, 50, 58, and 98.)

[108] P. K. Kundu, I. M. Cohen, and D. Dowling. *Fluid Mechanics*. Elsevier, 6 edition, 2016. (Cited on page 9.)

[109] L. Prandtl. Meteorologische Anwendung der Strömungslehre. *Beitr. Phys. Atmosph.*, 19:188–202, 1932. (Cited on page 10.)

[110] P. A. Gilman. Nonlinear dynamics of Boussinesq convection in a deep rotating spherical shell-I. *Geophys. Astrophys. Fluid Dyn.*, 8(1):93–135, 1977. (Cited on page 10.)

[111] R. J. A. M. Stevens, J.-Q. Zhong, H. J. H. Clercx, G. Ahlers, and D. Lohse. Transitions between turbulent states in rotating Rayleigh–Bénard convection. *Phys. Rev. Lett.*, 103(2):024503, 2009. (Cited on page 10.)

[112] W. B. Heard and G. Veronis. Asymptotic treatment of the stability of a rotating layer of fluid with rigid boundaries. *Geophys. Fluid Dyn.*, 2(1):299–316, 1971. (Cited on page 12.)

[113] K. Julien, J. M. Aurnou, M. A. Calkins, E. Knobloch, P. Marti, S. Stellmach, and G. M. Vasil. A nonlinear model for rotationally constrained convection with Ekman pumping. *J. Fluid Mech.*, 798:50–87, 2016. (Cited on pages 12, 38, and 70.)

[114] F. H. Busse. Non-linear properties of thermal convection. *Rep. Prog. Phys.*, 41(12):1929, 1978. (Cited on page 13.)

[115] S. Grossmann and D. Lohse. Scaling in thermal convection: a unifying theory. *J. Fluid Mech.*, 407:27–56, 2000. (Cited on pages 13, 55, 56, 68, and 98.)

[116] J. Pedlosky. *Geophysical Fluid Dynamics*. Springer, 1979. (Cited on pages 13, 14, 15, 47, 69, and 77.)

[117] G. I. Taylor. Motion of solids in fluids when the flow is not irrotational. *Proc. R. Soc. Lond. A*, 93(648):99–113, 1917. (Cited on page 14.)

[118] J. Proudman. On the motion of solids in a liquid possessing vorticity. *Proc. R. Soc. Lond. A*, 92(642):408–424, 1916. (Cited on page 14.)

[119] K. Stewartson. On almost rigid rotations. *J. Fluid Mech.*, 3(1):17–26, 1957. (Cited on pages 17 and 18.)

[120] K. Stewartson. On almost rigid rotations. Part 2. *J. Fluid Mech.*, 26(1):131–144, 1966. (Cited on pages 17 and 18.)

[121] R. P. J. Kunnen, H. J. H. Clercx, and G. J. F. van Heijst. The structure of sidewall boundary layers in confined rotating Rayleigh–Bénard convection. *J. Fluid Mech.*, 727:509–532, 2013. (Cited on pages 18, 86, 87, 90, and 102.)

[122] A. S. Monin and A. M. Yaglom. *Statistical Fluid Mechanics*, volume 2. The MIT Press, Cambridge, Mass., 1975. (Cited on page 18.)

[123] B. I. Shraiman and E. D. Siggia. Heat transport in high-Rayleigh-number convection. *Phys. Rev. A*, 42(6):3650, 1990. (Cited on pages 19 and 27.)

[124] E. D. Siggia. High Rayleigh number convection. *Annu. Rev. Fluid Mech.*, 26(1):137–168, 1994. (Cited on page 19.)

[125] R. Verzicco and P. Orlandi. A finite-difference scheme for three-dimensional incompressible flows in cylindrical coordinates. *J. Comput. Phys.*, 123(2):402–414, 1996. (Cited on pages 21, 22, and 23.)

[126] R. Ostilla-Mónico, Y. Yang, E. P. van der Poel, D. Lohse, and R. Verzicco. A multiple-resolution strategy for Direct Numerical Simulation of scalar turbulence. *J. Comput. Phys.*, 301:308–321, 2015. (Cited on pages 21 and 22.)

[127] R. Verzicco and R. Camussi. Numerical experiments on strongly turbulent thermal convection in a slender cylindrical cell. *J. Fluid Mech.*, 477:19, 2003. (Cited on pages 22, 23, and 27.)

[128] J. S. Cheng, J. M. Aurnou, K. Julien, and R. P. J. Kunnen. A heuristic framework for next-generation models of geostrophic convective turbulence. *Geophys. Astrophys. Fluid Dyn.*, 112(4):277–300, 2018. (Cited on pages 23, 30, 79, 82, 84, and 85.)

[129] Description of the Cartesius system (Surfsara). `https://userinfo.surfsara.nl/systems/cartesius/description`. Accessed: 01 November 2020. (Cited on page 23.)

[130] P. Moin and K. Mahesh. Direct numerical simulation: a tool in turbulence research. *Annu. Rev. Fluid Mech.*, 30(1):539–578, 1998. (Cited on page 27.)

[131] S. B. Pope. *Turbulent Flows*. Cambridge University Press, 2001. (Cited on pages 27 and 75.)

[132] D. Nieves, A. M. Rubio, and K. Julien. Statistical classification of flow morphology in rapidly rotating Rayleigh–Bénard convection. *Phys. Fluids*, 26(8):086602, 2014. (Cited on pages 33, 39, 47, 51, 52, and 72.)

[133] J. Aubert, D. Brito, H. C. Nataf, P. Cardin, and J. P. Masson. A systematic experimental study of rapidly rotating spherical convection in water and liquid gallium. *Phys. Earth Planet. Inter.*, 128(1-4):51–74, 2001. (Cited on page 35.)

[134] J. Aubert. Steady zonal flows in spherical shell dynamos. *J. Fluid Mech.*, 542:53, 2005. (Cited on page 35.)

[135] U. R. Christensen. Zonal flow driven by strongly supercritical convection in rotating spherical shells. *J. Fluid Mech.*, 470:115, 2002. (Cited on page 35.)

[136] E. M. King and B. A. Buffett. Flow speeds and length scales in geodynamo models: the role of viscosity. *Earth Planet. Sci. Lett.*, 371:156–162, 2013. (Cited on page 35.)

[137] J. M. Aurnou, M. A. Calkins, J. S. Cheng, K. Julien, E. M. King, D. Nieves, K. M. Soderlund, and S. Stellmach. Rotating convective turbulence in Earth and planetary cores. *Phys. Earth Planet. Inter.*, 246:52–71, 2015. (Cited on page 35.)

[138] T. Gastine, J. Wicht, and J. Aubert. Scaling regimes in spherical shell rotating convection. *J. Fluid Mech.*, 808:690–732, 2016. (Cited on page 35.)

[139] C. Guervilly, P. Cardin, and N. Schaeffer. Turbulent convective length scale in planetary cores. *Nature*, 570(7761):368–371, 2019. (Cited on page 35.)

[140] K. M. Soderlund, E. M. King, and J. M. Aurnou. The influence of magnetic fields in planetary dynamo models. *Earth Planet. Sci. Lett*, 333:9–20, 2012. (Cited on page 35.)

[141] R. K. Yadav, T. Gastine, U. R. Christensen, S. J. Wolk, and K. Poppenhaeger. Approaching a realistic force balance in geodynamo simulations. *Proc. Natl. Acad. Sci.*, 113(43):12065–12070, 2016. (Cited on page 35.)

[142] J. Aubert, T. Gastine, and A. Fournier. Spherical convective dynamos in the rapidly rotating asymptotic regime. *J. Fluid Mech.*, 813:558–593, 2017. (Cited on page 35.)

[143] J. Aubert. Approaching Earth's core conditions in high-resolution geodynamo simulations. *Geophys. J. Int*, 219(Supplement_1):S137–S151, 2019. (Cited on page 35.)

[144] T. Schwaiger, T. Gastine, and J. Aubert. Relating force balances and flow length scales in geodynamo simulations. *Geophys. J. Int*, 224(3):1890–1904, 2021. (Cited on page 35.)

[145] M. A. Calkins, K. Julien, S. M. Tobias, and J. M. Aurnou. A multiscale dynamo model driven by quasi-geostrophic convection. *J. Fluid Mech.*, 780:143–166, 2015. (Cited on page 35.)

[146] F. H. Busse. Thermal instabilities in rapidly rotating systems. *J. Fluid Mech.*, 44(3):441–460, 1970. (Cited on page 38.)

[147] J. G. Charney. Geostrophic turbulence. *J. Atmos. Sci.*, 28(6):1087–1095, 1971. (Cited on page 38.)

[148] J. G. Charney. On the scale of atmospheric motions. In *Geophys. Publ.*, number 17, pages 3–17. 1948. (Cited on page 38.)

[149] J. Aubert, N. Gillet, and P. Cardin. Quasigeostrophic models of convection in rotating spherical shells. *Geochem. Geophys.*, 4(7), 2003. (Cited on page 38.)

[150] N. Gillet and C. A. Jones. The quasi-geostrophic model for rapidly rotating spherical convection outside the tangent cylinder. *J. Fluid Mech.*, 554:343, 2006. (Cited on page 38.)

[151] M. A. Calkins, J. Noir, J. D. Eldredge, and J. M. Aurnou. The effects of boundary topography on convection in Earth's core. *Geophys. J. Int.*, 189(2):799–814, 2012. (Cited on page 38.)

[152] K. Julien, E. Knobloch, and J. Werne. A new class of equations for rotationally constrained flows. *Theor. Comput. Fluid Dyn.*, 11(3):251–261, 1998. (Cited on page 38.)

[153] K. Julien, E. Knobloch, R. Milliff, and J. Werne. Generalized quasi-geostrophy for spatially anisotropic rotationally constrained flows. *J. Fluid Mech.*, 555:233, 2006. (Cited on page 38.)

[154] J. W. Portegies, R. P. J. Kunnen, G. J. F. van Heijst, and J. Molenaar. A model for vortical plumes in rotating convection. *Phys. Fluids*, 20:066602, 2008. (Cited on pages 41 and 85.)

[155] R. M. Kerr. Rayleigh number scaling in numerical convection. *J. Fluid Mech.*, 310:139–179, 1996. (Cited on page 50.)

[156] C.-H. Moeng and R. Rotunno. Vertical-velocity skewness in the buoyancy-driven boundary layer. *J. Atmos. Sci*, 47(9):1149–1162, 1990. (Cited on page 50.)

[157] R. P. J. Kunnen, B. J. Geurts, and H. J. H. Clercx. Turbulence statistics and energy budget in rotating Rayleigh–Bénard convection. *Eur. J. Mech. B/Fluids*, 28(4):578–589, 2009. (Cited on pages 50, 53, 61, 75, and 77.)

[158] G. K. Batchelor. *The Theory of Homogeneous Turbulence.* Cambridge University Press, 1953. (Cited on page 51.)

[159] M. Wilczek, A. Daitche, and R. Friedrich. On the velocity distribution in homogeneous isotropic turbulence: correlations and deviations from Gaussianity. *J. Fluid Mech.*, 676:191–217, 2011. (Cited on page 51.)

[160] M. Buzzicotti, A. Bhatnagar, L. Biferale, A. S. Lanotte, and S. S. Ray. Lagrangian statistics for Navier–Stokes turbulence under Fourier-mode reduction: fractal and homogeneous decimations. *New J. Phys.*, 18(11):113047, 2016. (Cited on page 51.)

[161] A. Belmonte, A. Tilgner, and A. Libchaber. Temperature and velocity boundary layers in turbulent convection. *Phys. Rev. E*, 50(1):269, 1994. (Cited on page 51.)

[162] S.-L. Lui and K.-Q. Xia. Spatial structure of the thermal boundary layer in turbulent convection. *Phys. Rev. E*, 57(5):5494, 1998. (Cited on page 51.)

[163] G. Ahlers, E. Bodenschatz, D. Funfschilling, S. Grossmann, X. He, D. Lohse, R. J. A. M. Stevens, and R. Verzicco. Logarithmic temperature profiles in turbulent Rayleigh–Bénard convection. *Phys. Rev. Lett.*, 109(11):114501, 2012. (Cited on page 51.)

[164] R. du Puits, C. Resagk, and A. Thess. Thermal boundary layers in turbulent Rayleigh–Bénard convection at aspect ratios between 1 and 9. *New J. Phys.*, 15(1):013040, 2013. (Cited on page 51.)

[165] R. P. J. Kunnen, H. J. H. Clercx, and B. J. Geurts. Breakdown of large-scale circulation in turbulent rotating convection. *EPL*, 84(2):24001, 2008. (Cited on page 51.)

[166] P. Vorobieff and R. E. Ecke. Vortex structure in rotating Rayleigh–Bénard convection. *Physica D*, 123(1-4):153–160, 1998. (Cited on page 51.)

[167] R. P. J. Kunnen, H. J. H. Clercx, B. J. Geurts, L. J. A. van Bokhoven, R. A. D. Akkermans, and R. Verzicco. Numerical and experimental investigation of structure-function scaling in turbulent Rayleigh–Bénard convection. *Phys. Rev. Lett.*, 77(1):016302, 2008. (Cited on page 51.)

[168] C. Morize, F. Moisy, and M. Rabaud. Decaying grid-generated turbulence in a rotating tank. *Phys. Fluids*, 17(9):095105, 2005. (Cited on page 52.)

[169] P. J. Staplehurst, P. A. Davidson, and S. B. Dalziel. Structure formation in homogeneous freely decaying rotating turbulence. *J. Fluid Mech.*, 598:81, 2008. (Cited on page 52.)

[170] F. Moisy, C. Morize, M. Rabaud, and J. Sommeria. Decay laws, anisotropy and cyclone-anticyclone asymmetry in decaying rotating turbulence. *J. Fluid Mech.*, 666:5, 2011. (Cited on page 52.)

[171] F. S. Godeferd and F. Moisy. Structure and dynamics of rotating turbulence: a review of recent experimental and numerical results. *Appl. Mech. Rev.*, 67(3):030802, 2015. (Cited on pages 52 and 73.)

[172] K. Yoshimatsu, M. Midorikawa, and Y. Kaneda. Columnar eddy formation in freely decaying homogeneous rotating turbulence. *J. Fluid Mech.*, 677:154, 2011. (Cited on page 52.)

[173] P. Bartello, O. Métais, and M. Lesieur. Coherent structures in rotating three-dimensional turbulence. *J. Fluid Mech.*, 273:1–29, 1994. (Cited on page 52.)

[174] L. J. A. van Bokhoven, C. Cambon, L. Liechtenstein, F. S. Godeferd, and H. J. H. Clercx. Refined vorticity statistics of decaying rotating three-dimensional turbulence. *J. Turbul.*, (9):N6, 2008. (Cited on page 52.)

[175] B. Sreenivasan and P. A. Davidson. On the formation of cyclones and anticyclones in a rotating fluid. *Phys. Fluids*, 20(8):085104, 2008. (Cited on pages 52 and 73.)

[176] L. M. Polvani, J. C. McWilliams, M. A. Spall, and R. Ford. The coherent structures of shallow-water turbulence: Deformation-radius effects, cyclone/anticyclone asymmetry and gravity-wave generation. *Chaos*, 4(2):177–186, 1994. (Cited on page 52.)

[177] G. J. Hakim, C. Snyder, and D. J. Muraki. A new surface model for cyclone-anticyclone asymmetry. *J. Atmos. Sci.*, 59(16):2405–2420, 2002. (Cited on page 52.)

[178] G. Perret, A. Stegner, M. Farge, and T. Pichon. Cyclone-anticyclone asymmetry of large-scale wakes in the laboratory. *Phys. Fluids*, 18(3):036603, 2006. (Cited on page 52.)

[179] L. P. Graves, J. C. McWilliams, and M. T. Montgomery. Vortex evolution due to straining: A mechanism for dominance of strong, interior anticyclones. *Geophys. Astrophys. Fluid Dyn.*, 100(3):151–183, 2006. (Cited on page 52.)

[180] J. E. Hart and D. R. Ohlsen. On the thermal offset in turbulent rotating convection. *Phys. Fluids*, 11(8):2101–2107, 1999. (Cited on page 53.)

[181] K. Julien and E. Knobloch. Fully nonlinear three-dimensional convection in a rapidly rotating layer. *Phys. Fluids*, 11(6):1469–1483, 1999. (Cited on page 53.)

[182] S. Grossmann and D. Lohse. Fluctuations in turbulent Rayleigh–Bénard convection: the role of plumes. *Phys. Fluids*, 16:4462–4472, 2004. (Cited on pages 55, 56, 68, and 98.)

[183] R. J. A. M. Stevens, E. P. van der Poel, S. Grossmann, and D. Lohse. The unifying theory of scaling in thermal convection: the updated prefactors. *J. Fluid Mech.*, 730:295–308, 2013. (Cited on pages 55, 56, 68, and 98.)

[184] S. Grossmann and D. Lohse. Thermal convection for large Prandtl numbers. *Phys. Rev. Lett.*, 86:3316–3319, 2001. (Cited on pages 55, 56, 68, and 98.)

[185] G. Ahlers, Siegfried Grossmann, and D. Lohse. Heat transfer and large scale dynamics in turbulent Rayleigh-Bénard convection. *Rev. Mod. Phys.*, 81(2):503, 2009. (Cited on page 70.)

[186] R. H. Kraichnan. Inertial ranges in two-dimensional turbulence. *Phys. Fluids*, 10(7):1417–1423, 1967. (Cited on page 70.)

[187] G. K. Batchelor. Computation of the energy spectrum in homogeneous two-dimensional turbulence. *Phys. Fluids*, 12(12):II–233, 1969. (Cited on page 70.)

[188] L. M. Smith and V. Yakhot. Finite-size effects in forced two-dimensional turbulence. *J. Fluid Mech.*, 274:115–138, 1994. (Cited on page 70.)

[189] M. Chertkov, C. Connaughton, I. Kolokolov, and V. Lebedev. Dynamics of energy condensation in two-dimensional turbulence. *Phys. Rev. Lett.*, 99(8):084501, 2007. (Cited on page 70.)

[190] A. Frishman and C. Herbert. Turbulence statistics in a two-dimensional vortex condensate. *Phys. Rev. Lett.*, 120(20):204505, 2018. (Cited on page 70.)

[191] G. Boffetta and R. E. Ecke. Two-dimensional turbulence. *Annu. Rev. Fluid Mech.*, 44:427–451, 2012. (Cited on page 70.)

[192] A. Alexakis and L. Biferale. Cascades and transitions in turbulent flows. *Phys. Rep.*, 767:1–101, 2018. (Cited on pages 70 and 72.)

[193] H. Xia, D. Byrne, G. Falkovich, and M. Shats. Upscale energy transfer in thick turbulent fluid layers. *Nat. Phys.*, 7(4):321, 2011. (Cited on page 72.)

[194] E. J. Hopfinger, F. K. Browand, and Y. Gagne. Turbulence and waves in a rotating tank. *J. Fluid Mech.*, 125:505–534, 1982. (Cited on page 73.)

[195] C. N. Baroud, B. B. Plapp, H. L. Swinney, and Z.-S. She. Scaling in three-dimensional and quasi-two-dimensional rotating turbulent flows. *Phys. Fluids*, 15(8):2091–2104, 2003. (Cited on page 73.)

[196] K. Seshasayanan and A. Alexakis. Condensates in rotating turbulent flows. *J. Fluid Mech.*, 841:434–462, 2018. (Cited on page 73.)

[197] A. Alexakis, P. D. Mininni, and A. Pouquet. Shell-to-shell energy transfer in magnetohydrodynamics. I. Steady state turbulence. *Phys. Rev. E*, 72(4):046301, 2005. (Cited on page 73.)

[198] P. D. Mininni, A. Alexakis, and A. Pouquet. Scale interactions and scaling laws in rotating flows at moderate Rossby numbers and large Reynolds numbers. *Phys. Fluids*, 21(1):015108, 2009. (Cited on page 73.)

[199] G. Dar, M. K. Verma, and V. Eswaran. Energy transfer in two-dimensional magnetohydrodynamic turbulence: formalism and numerical results. *Physica D*, 157(3):207–225, 2001. (Cited on page 73.)

[200] M. K. Verma, A. Kumar, and A. Pandey. Phenomenology of buoyancy-driven turbulence: recent results. *New J. Phys.*, 19(2):025012, 2017. (Cited on page 73.)

[201] M. K. Verma. *Energy Transfers in Fluid Flows: Multiscale and Spectral Perspectives.* Cambridge University Press, 2019. (Cited on page 73.)

[202] J. W. Deardorff and G. E. Willis. Investigation of turbulent thermal convection between horizontal plates. *J. Fluid Mech.*, 28(4):675–704, 1967. (Cited on page 75.)

[203] R. M. Kerr. Energy budget in Rayleigh–Bénard convection. *Phys. Rev. Lett.*, 87(24):244502, 2001. (Cited on page 75.)

[204] B. Favier, C. Guervilly, and E. Knobloch. Subcritical turbulent condensate in rapidly rotating Rayleigh–Bénard convection. *J. Fluid Mech.*, 864:R1, 2019. (Cited on page 82.)

[205] S. Horn and J. M. Aurnou. Regimes of Coriolis–Centrifugal Convection. *Phys. Rev. Lett.*, 120:204502, 2018. (Cited on page 82.)

[206] S. Horn and J. M. Aurnou. Rotating convection with centrifugal buoyancy: Numerical predictions for laboratory experiments. *Phys. Rev. Fluids*, 4:073501, 2019. (Cited on page 82.)

[207] R. P. J. Kunnen, R. J. A. M. Stevens, J. Overkamp, C. Sun, G. J. F. van Heijst, and H. J. H. Clercx. The role of Stewartson and Ekman layers in turbulent rotating Rayleigh–Bénard convection. *J. Fluid Mech.*, 688:422, 2011. (Cited on pages 86 and 87.)

[208] E. Brown and G. Ahlers. Rotations and cessations of the large-scale circulation in turbulent Rayleigh–Bénard convection. *J. Fluid Mech.*, 568:351–386, 2006. (Cited on page 87.)

[209] K. Zhang and X. Liao. The onset of convection in rotating circular cylinders with experimental boundary conditions. *J. Fluid Mech.*, 622:63–73, 2009. (Cited on page 90.)

Summary

Numerical study of rapidly rotating turbulent convection

Convectively driven flows subject to the influence of rotation are everywhere in nature, from Earth's liquid-metal outer core, oceans and atmosphere to the interior and atmosphere of other planets and stars like our Sun. Understanding the dynamics of these geophysical and astrophysical flows is of paramount importance, yet their sheer size, remoteness and complexity preclude their direct investigation. The canonical model of rotating Rayleigh–Bénard convection (RRBC), the flow between two co-rotating horizontal plates heated from below and cooled from above, provides a simple but highly relevant framework to study these flows. We investigate RRBC using direct numerical simulation on a horizontally periodic domain. This geometry is relevant to large-scale natural settings, where the horizontal dimension is much larger than the vertical (as in oceans) or even present no lateral confinement (as in planetary and stellar atmospheres). No-slip boundary conditions at the top and bottom walls are employed. This provides realistic boundary conditions, relevant to natural systems and laboratory experiments. For comparison, some additional simulations on a confined cylindrical domain are considered. This results are also compared with those from the laboratory experiment TROCONVEX in our group.

In the explored parameter space, regimes of cellular convection, convective Taylor columns, plumes, large-scale vortices (LSVs) and rotation-affected convection are observed. In rotationally constrained regimes (cells, columns, plumes and LSVs) both the bulk and near-wall flow is primarily geostrophic, i.e. the balance between Coriolis and pressure-gradient forces constitute the dominant force balance in the flow. The geostrophic flows are however ageostrophic at higher order, as a result of the contribution of the remaining forces (inertia, viscous and buoyancy forces). The higher order interplay between these forces defines a subdominant balance that distinguishes the distinct geostrophic states. Low Prandtl number simulations (where the flow is more prone to turbulence) reveal that this rotational constraint is lost, both in the bulk and near the walls, when the flow becomes more turbulent, in the rotation-affected regime. Near the walls, the kinetic boundary layer dynamics is also affected: it transitions from an Ekman-type behaviour to displaying significant deviations from it.

The thermal boundary layer thickness approaches the non-rotating value.

In the next part of the thesis, we link the flow behaviours that result from the force balances with their corresponding temperature features. The heat transport scaling with flow supercriticality (defined here as the ratio between the Rayleigh number and its critical value for onset of convection) is studied. Closer to the onset, the flow structures (cells and columns) efficiently transport heat. This results in a steep heat transport scaling. As turbulence increases (for plumes, LSVs and rotation-affected convection) the scaling becomes shallower. The temperature features near the walls are affected by the relative thickness of the kinetic and thermal boundary layers. In particular, the skewness sign of the temperature distribution at the kinetic boundary layer depends on whether this boundary layer is embedded within the thermal boundary layer or not.

The following part focuses on the regime of large-scale vortices. We study their competing dynamics against Ekman pumping from the boundary layers. A mechanism for the interaction between LSVs and the Ekman plumes is presented. This result is particularly relevant in geophysics and astrophysics, where large-scale flows develop regardless of the presence of frictional boundaries.

In the last part, RRBC is studied on a confined cylindrical domain. This configuration yields the development of a sidewall circulation, which contributes significantly to the overall heat transport across the fluid layer. The sidewall circulation ejects fluid into the bulk. This effect appears to be smaller at larger Rayleigh numbers. We discuss the nature of the sidewall circulation and its influence on the bulk, and compare the resulting bulk dynamics with the unbounded (periodic) case at various Rayleigh numbers. These findings establish the ground for comparison between confined settings, such as laboratory experiments, and laterally periodic simulations.

The findings presented in this thesis elucidate the force balance, flow dynamics and thermal properties specific to various regimes of rapidly rotating Rayleigh–Bénard convection. The consideration of boundary conditions relevant to large-scale natural settings provides the fundamental framework for extrapolation of our results towards geophysical and astrophysical applications.

Cover Illustration

Snapshot of horizontal kinetic energy of rotating thermal convection displaying a large-scale vortex (LSV). The simulation parameters are: Rayleigh number $Ra = 10^{10}$, Ekman number $Ek = 2.5 \times 10^{-7}$ and Prandtl number $Pr = 0.1$. The colour scale is chosen to highlight the flow features. The horizontal kinetic energy increases from blue to red. The domain is horizontally periodic, vertically bounded by no-slip top and bottom boundaries. The actual domain is slender: its width-to-height ratio $\Gamma = 0.326$. For better visibility, the domain is stretched horizontally by a factor of 3.

Curriculum Vitae

20 August 1992	Born in Valencia, Venezuela
2009–2014	**Licentiate degree in Physics** University of Carabobo Valencia, Venezuela
2015–2016	**Postgraduate diploma in Earth System Physics** The Abdus Salam International Centre for Theoretical Physics Trieste, Italy
2016–2020	**PhD in Applied Physics** Fluids and Flows group Department of Applied Physics Eindhoven University of Technology Eindhoven, The Netherlands

List of publications and conferences

This thesis is based on the following publications

- A. J. Aguirre Guzmán, M. Madonia, J. S. Cheng, R. Ostilla-Mónico, H. J. H. Clercx and R. P. J. Kunnen. Force balance in rapidly rotating Rayleigh–Bénard convection. *Submitted to Journal of Fluid Mechanics.* **(Chapter 4)**

- A. J. Aguirre Guzmán, M. Madonia, J. S. Cheng, R. Ostilla-Mónico, H. J. H. Clercx and R. P. J. Kunnen. Flow statistics of rotating Rayleigh–Bénard convection regimes. *In preparation.* **(Chapter 5)**

- A. J. Aguirre Guzmán, M. Madonia, J. S. Cheng, R. Ostilla-Mónico, H. J. H. Clercx, and R. P. J. Kunnen. Competition between Ekman plumes and vortex condensates in rapidly rotating thermal convection. *Phys. Rev. Lett.*, 125(21):214501, 2020. **(Chapter 6)**

- X. M. de Wit, A. J. Aguirre Guzmán, M. Madonia, J. S. Cheng, H. J. H. Clercx, and R. P. J. Kunnen. Turbulent rotating convection confined in a slender cylinder: The sidewall circulation. *Phys. Rev. Fluids*, 5(2):023502, 2020. **(Chapter 7)**

Other publications

- J. S. Cheng, M. Madonia, A. J. Aguirre Guzmán, and R. P. J. Kunnen. Laboratory exploration of heat transfer regimes in rapidly rotating turbulent convection. *Phys. Rev. Fluids*, 5(11):113501, 2020.

Conference contributions

- A. J. Aguirre Guzmán, M. Madonia, J. S. Cheng, R. Ostilla-Mónico, H. J. H. Clercx and R. P. J. Kunnen. Talk: Large scale vortices in rotating thermal convection. Physics@Veldhoven 2020, Veldhoven, The Netherlands, January 2020.

- A. J. Aguirre Guzmán, M. Madonia, J. S. Cheng, R. Ostilla-Mónico, H. J. H. Clercx and R. P. J. Kunnen. Talk: Geostrophic turbulent regime of rotating Rayleigh–Bénard convection at different Prandtl numbers. ETC2019 17th European Turbulence Conference, Turin, Italy, September 2019.
- A. J. Aguirre Guzmán, M. Madonia, J. S. Cheng, R. Ostilla-Mónico, H. J. H. Clercx and R. P. J. Kunnen. Talk: Flow regimes in turbulent rotating Rayleigh–Bénard convection at different Prandtl numbers. Burgers Symposium 2019, J. M. Burgers Centre for Fluid Dynamics, Lunteren, The Netherlands, May 2019.
- A. J. Aguirre Guzmán, R. Ostilla-Mónico, H. J. H. Clercx and R. P. J. Kunnen. Talk: Turbulent rotating Rayleigh–Bénard convection at different Prandtl numbers. Meeting JMBC contact group Turbulence, J. M. Burgers Centre for Fluid Dynamics, Eindhoven, The Netherlands, April 2019.
- A. J. Aguirre Guzmán, M. Madonia, J. S. Cheng, R. Ostilla-Mónico, H. J. H. Clercx and R. P. J. Kunnen. Poster: Rotating Rayleigh–Bénard convection at different Prandtl numbers: the geostrophic turbulent regime. Physics@Veldhoven 2019, The Netherlands Organisation for Scientific Research (NWO), Veldhoven, The Netherlands, January 2019.
- A. J. Aguirre Guzmán, R. Ostilla-Mónico, H. J. H. Clercx and R. P. J. Kunnen. Talk: Prandtl number dependence of the transition to the geostrophic regime of rotating Rayleigh–Bénard convection. 71st Annual Meeting of the APS Division of Fluid Dynamics, Atlanta, Georgia, USA, November 2018.
- A. J. Aguirre Guzmán, M. Madonia, J. S. Cheng, H. J. H. Clercx and R. P. J. Kunnen. Talk: Rotating Rayleigh–Bénard convection at different Prandtl numbers. Burgers Symposium 2018, J. M. Burgers Centre for Fluid Dynamics, Lunteren, The Netherlands, June 2018.
- A. J. Aguirre Guzmán, M. Madonia, J. S. Cheng, H. J. H. Clercx and R. P. J. Kunnen. Poster: Direct numerical simulations of rapidly rotating Rayleigh–Bénard convection. Rotating Convection from the Lab to the Stars - EUROMECH Colloquium 599, Leiden, The Netherlands, May 2018.
- A. J. Aguirre Guzmán, H. J. H. Clercx and R. P. J. Kunnen. Poster: Rapidly rotating thermal convection at low Prandtl number.

Physics@Veldhoven 2018, The Netherlands Organisation for Scientific Research (NWO), Veldhoven, The Netherlands, January 2018.

- A. J. Aguirre Guzmán, R. Ostilla-Mónico, H. J. H. Clercx and R. P. J. Kunnen. Talk: Rotating Rayleigh–Bénard convection at low Prandtl number. 70th Annual Meeting of the APS Division of Fluid Dynamics, Denver, Colorado, USA, November 2017.
- A. J. Aguirre Guzmán, R. P. J. Kunnen and H. J. H. Clercx. Flash pitch and Poster: Rapidly rotating Rayleigh–Bénard convection at low Pr. Burgers Symposium 2017, J. M. Burgers Centre for Fluid Dynamics, Lunteren, The Netherlands, May 2017.

Acknowledgements

Over the past four years I have received a great deal of guidance, support and encouragement. I would like to extend my sincere and heartfelt gratitude to the many people who have enriched these educational years and have made this manuscript possible.

First of all, I am profoundly grateful to my supervisors Herman Clercx and Rudie Kunnen, who gave me the opportunity to work on this fascinating project. Herman, your insightful and critical feedback pushed me to sharpen my thinking and brought my research to a higher level. Rudie, thanks for promoting, through example, an exploratory attitude towards my research and an open mind in the interpretation of the results. I thank you both for your patience, guidance and encouragement.

I would like to thank the members of my committee Hans Kuerten, Saša Kenjereš, Roberto Verzicco and Federico Toschi for reading and evaluating my thesis. A special thanks to Keith Julien for useful comments on the key chapters of this thesis that led to their improvement.

The results presented here are the product of a collaborative effort. I would like to thank Matteo Madonia, Jonathan Cheng and Rodolfo Ostilla-Mónico for critically reviewing my numerous drafts of our papers, and for continually providing me with new perspectives on my work. I am particularly thankful to Rodolfo for always being available to help me with all matters concerning the codes used for the simulations. I would also like to thank Xander de Wit, whose BEP results contributed to one of the chapters of this thesis.

My appreciation also extends to my friends, colleagues and former colleagues of the Turbulence and Vortex Dynamics group (now Fluids and Flows group): Abheeti, Abhineet, Alessandro, Altuğ, Andrei, Arnab, Bijan, Bojia, Cosimo, Dennis, Felix, Francesca, GertJan, Gianluca, Gianmarco, Giorgia, Hadi, Haijing, Hanneke, Ivo, Jonathan, Josje, Karun, Kim, Lenin, Leon, Maarten, Marjan, Marlies, Matteo, Matias, Rik, Samuel, Sebastián, Steven, Twan, Vignesh, Wolfram and Xiao. Thank you all for the great experiences we shared: borrels, conference trips, dinners. Haijing, thank you for giving me a glimpse into Chinese culture. Matias, Samuel and Sebastián, thank you for helping me keep my Spanish alive. Felix, I am grateful for our great conversations during conference trips. Steven, I am thankful for our occasional table tennis matches at the beginning of my

PhD. Cosimo and Jonathan, thank you for the wonderful climbing trips we had. I would also like to thank Xander, Kees, Hannah and Wouter for their contribution to the field of rotating Rayleigh–Bénard convection through their master and bachelor projects. And last but not least, Marjan, a big thank you for your invaluable efforts of arranging all formalities for everybody in the group.

Living abroad is by no means easy, I am thus glad to have met Carlo, Melania, Lars, Alejandro and Rainer. Thank you guys for the good times, climbing sessions and for making life in Eindhoven so enjoyable. I am also grateful to count with the support, warmth and hospitality of my Venezuelan friends in Europe: Alexander, Ambar, Carla, Eduardo, Héctor, Juan Pablo and Luis. En especial, quisiera agradecer a Alexander, Javier, Luciana y Fidel por abrirme las puertas de su casa siempre que los visito, por brindarme su calidez familiar y por los buenos momentos.

I shall be forever indebted to my dear family for always being there for me. Mamá, papá, Mariana, Fernando, Yanny, gracias por su amor, paciencia y apoyo incondicional, y además por siempre darme la confianza para crecer en la dirección que decida.

Rad bi se zahvalil in izkazal globoko hvaležnost družini moje življenjske sopotnice Nine, in sicer Vinku, Ani, Roku, Kaji, Brini in Gabru. Z vami sem odkril čudovito in toplo družino, v kateri se počutim ljubljen. Hvala, ker ste zame odprli vrata svojega doma in me sprejeli kot člana vaše družine.

Zadnji odstavek moje disertacije namenjam tebi, Nina. Tukaj sva. Uspelo nama je. Ni nama bilo lahko, a v tem času si me navdušila z ogromno mero predanosti, potrpežljivosti in podpore, s čimer si daleč presegla vsa moja pričakovanja. Zdaj je čas, da rasteva skupaj in da sedaj ti slediš svojim sanjam, da narediš, kar moreš narediti za izpolnitev le-teh. Podpiral te bom kot si me ti. Na vsakem koraku tvoje poti.

Andrés